Sabrina Meninno

# Mechanics of dry granular flows driven by gravity

UNIVERSITY OF TRENTO - Italy
Department of Civil, Environmental and Mechanical Engineering

Doctoral thesis in Environmental Engineering,
XXVI cycle

Supervisors: Prof. A. Armanini and Prof. M. Larcher

University of Trento
Department of Civil, Environmental and Mechanical Engineering

April 2015

# Abstract

Dry granular flows are an important paradigm for a large number of problems, from industrial applications to geophysical events. Most of the research published has studied inclined granular flows over bumpy and flat rigid base, while only few of them have been focused on fully developed steady flows over an erodible beds. This kind of flows are important to understand the dynamics of complex phenomena such as dense snow-avalanches and landslides, whose rheology is still ambiguous and not well defined. In this thesis, we focus on the following three aspects: (1) dynamics of uniform flows over loose bed, where the condition of uniformity and steadiness has accurately checked, (2) the influence of collisional parameters on the behavior of the flow, (3) the side-wall effect. Experimental investigations were carried out in laboratory through imaging techniques and direct methods to analyse the stresses exerted by the flow. The thesis contributes with accurate measurements of the mean velocity, solid concentration, and granular temperature profiles obtained along the depth and the free surface of the flow. Considerations have been derived in comparison to the existing data, pointing out the importance of collisional parameters and the conditions for uniform and steady flows. Experimental evaluation of the stresses was carried out at the side-walls of the channelized granular flows by the means of new device developed in the laboratory and tested for different configurations of the flow.

# Aknowledgements

First, and foremost, I would like to thank my supervisors Aronne Armanini and Michele Larcher for their help and encouragement during my thesis. Their patience, dedication, intelligence and positiveness will continue to inspire me for a long time to come. Additionally I would thank the technicians of the Laboratory of Hydraulics of Trento for their precious support in doing and preparing my experiments. As pointed out in an editorial of Nature (Nature 517, 528; 29 January 2015), "technical and support staff are such an important pillar of academic life", giving an important contribution to the research.

I would like to thank the many new friends that I encountered in these years. They made my experience in Trento unforgettable and unique with their love and joy. I am glad to have gone through this path with them, sharing the happy and sad moments, receiving and giving soothing words, and building a solid and beautiful bond that will link us forever. They have been my new family in Trento, giving me valuable memories that I will keep jealously.

Then, I would like to thank my parents for their unconditional support and for being always proud of me, even when I do not deserve it. My sister, my grandparents, and also my whole family have been always present in these years, cheering me from the colourful and sunny South. Lastly, I am grateful to my boyfriend who always encouraged me and loved, despite the distance that have kept us far away for a long time.

# Contents

# List of Figures

# List of Tables

# Chapter 1

# Introduction

## 1.1 Motivations

A granular material can be described as an ensemble of discrete macroscopic particles, such as sand in an hourglass or rice in a container. If agitated, these particles move like a liquid or a gas, otherwise they behave like a solid remaining at rest. This peculiarity has led many researchers to identify granular materials as a new form of matter that stands between the solid and the liquid one (Jaeger *et al.*, 1996) and has attracted the attention of many researchers in different fields of science.

Flows involving solid particulates are widely present both in industry and nature. They differentiate in shapes and sizes, ranging from micron-sized powders in the industrial application to blocks having a diameter of few meters in rock avalanches.

Grains are manipulated by the pharmaceutical, food and chemical industries, but they are also largely present in the construction activities and mining processes. In all these sectors they are transported, poured or mixed and sometimes they are stored in piles, silos or other containers. Understanding how granular flows behave is crucial to handle them properly and more efficiently avoiding, for example, the unwanted segregation of the coarse aggregates during the preparation of the concrete, or reducing the costs of transportation thanks to a correct design of the conveyor plants.

In nature, a great number of geophysical flows involving the mass movement can be reasonably described within the framework of granular matters. An example is given by snow-avalanches, which are among the most destructive hazards in the mountainous regions, due to their potential to carry enormous mass of snow at high speeds. But also, rock avalanches, debris-flows, both aerial and submarine, can be included among granular flows, and their comprehension is fundamental to save human lives and reduce property losses.

In recent decades, in fact, the increased population and the economical exploitation of the territory have enhanced the human pressure on vulnerable areas that are characterized by high level of hazards. The urge of finding effective solutions has fostered the research to develop reliable models to predict granular flows, and a great amount of works has been written on the topic.

Real granular flows can be subject to a plethora of complicating forces, including cohesion, van der Waals forces or magnetic forces. Indeed, even without any of these effects, the description of a dry, cohesion-less granular material still represents a challenge for researchers, and the question of which set of equations should be used to model them is still open.

Their macroscopic behaviour can be studied in the framework of the continuum mechanics despite of their heterogeneity and discontinuous nature. However, some peculiar characteristics make their description much more complicated with respect to gases, liquids and even solids.

For example, the analogy between macroscopic particles and molecules of gases has motivated researchers to apply the kinetic theory for dense gases to them since the 80's. However, because particles are inelastic and usually frictional, these models have been opportunely modified to take into account energy dissipation. Additionally, due to the finite dimension of the constituents, ordinary temperature plays no role in their dynamics, being a key factor that differentiates them from fluids and regular gases. The energy scale of granular flows is the potential energy, and the lack of a thermodynamic equilibrium means that entropic arguments are no longer valid (Aranson and Tsimring, 2006). As a result, segregation processes can be observed, with larger particles floating over smaller ones for a flow composed of two specimens, apparently violating the second law of the thermodynamics. Moreover, in some occasions, high density clusters can occur due to the inelastic collisions, unlike what can be expected for traditional gases.

Unlike fluids, hydrostatic law is not applicable to granular flows, and pressure increases linearly with the flow-depth until saturation, after which it becomes constant. This effect, known as Janssen effect (Janssen, 1895), is largely exploited in practical applications to regulate the discharge flowing from a container by changing only its aperture. Finally, static assemblies are very different from solids, since they exhibit the tendency to form arches and force chains, which break down when the ensemble of grains is moved with enough energy.

## 1.2 Objectives of the thesis

The thesis considers an experimental investigation on channelized dry granular flows in equilibrium with the loose bed.

The confined geometry is relevant to granular geophysical flows, which are often either confined by the topography or self-channelized by the formation of levees. Similarly, the presence of an erodible bed is significant for natural movements of mass, such as snow-avalanches and debris flows, which usually move on a loose deposit made of the same material that compose the flow. In such situation the erodible bed forms spontaneously, and it is dynamically coupled with the material flowing over it. Thus its slope depends entirely on the flow-field that characterizes the systems.

The work addresses different aspects of granular flows. The first objective is the relevance of the boundary conditions on the formation of steady and uniform flows for dry systems.

Then an accurate characterization of the dynamics is pursued through the imaging technique of Voronoï developed within a collaboration between the University of Trento, the National Taiwan University and the Université catholique de Louvain. Profiles of velocity, concentration and granular temperature are presented from very slow discharge to very fast flows. Vertical structures are highlighted together with transversal variations of the variables. These measurements are not available in literature for dry flows on inclined plane and are an important contribution to the description of these flows.

A third aspect investigated is the effect of the side-walls on the granular flows, and the impact of the micro-mechanical properties of particles on their interaction with the walls. A design of a specific tool to measure the stresses at the side-walls is discussed and presented in its preliminary version.

## 1.3 Thesis structure

The thesis is organized according to the following structure:

1. Chapter 2 gives an overview of the state of the art for the characterization of the granular flows, both experimentally and theoretically. Due to the extent of the subject, the focus is mainly directed on flows down inclines. After reporting the main findings on the topic, the most important theories are reviewed, paying more attention for the rheological models that are tested against the collected data.

2. Chapter 3 describes the experimental set-up and the techniques used to collect data. The principle of the Voronoï technique is briefly explained, together with the other method used to measured the variables of interest.

3. Chapter 4 shows the results, presenting the profiles of velocity, concentration and granular temperature for different ranges of investigation.

4. Chapter 5 considers a rheological interpretation of the data, and it discusses the feasibility of an hydraulic approach to them.

5. Chapter 6 draws the final conclusion of the work and the possible future developments.

# Chapter 2

# State of the art

## 2.1 General features of dry granular flows

Granular flows display very unique behaviours and physical phenomena. When at rest, granular samples take the shape of the container holding them (like liquids) although they can maintain a non-horizontal surface up to a maximum angle that is defined as the angle of repose (eg.Jackson, 1986; de Gennes, 1999; Jaeger *et al.*, 1996). Steeper inclinations have as result the collapse of the heap.

Together with packing fraction (defined as the ratio of the volume of grains and the bulk volume) (Grasselli and Herrmann, 1997; Aguirre *et al.*, 2001), the angle of repose depends on the features of the grains and on the construction history of the sample. Size distribution, shape and uniformity can influence the value of these parameters, by changing the structure of the heap and the distribution of the forces.

Interesting aspects have been highlighted by experimental works (eg Vanel *et al.*, 1999; Daerr and Douady, 1999), which have shown that for granular at rest forces tend to propagate sidewards, forming arches through the pile, while right below the center, the pressure exhibits a local minimum.

Peculiar aspects of the granular materials can be observed also when they flow like fluids, since they exhibit some counter-intuitive behaviours. Segregation is one of these anomalies, involving the separation of individual granular species inside a bi-disperse or poly-dispersed flow, where the be-poly-dispersion can be due to different sizes, shapes and density. Jamming is another characteristic that differentiate granular flows from liquids, and it occurs when the flow tends to become rigid and stagnating following the formation of force chains (eg da Cruz *et al.*, 2005; Lois *et al.*, 2006).

Generally speaking, the discontinuous and inhomogeneous nature of granular materials leads to complex mechanical behaviours, even in the case of simple flow con-

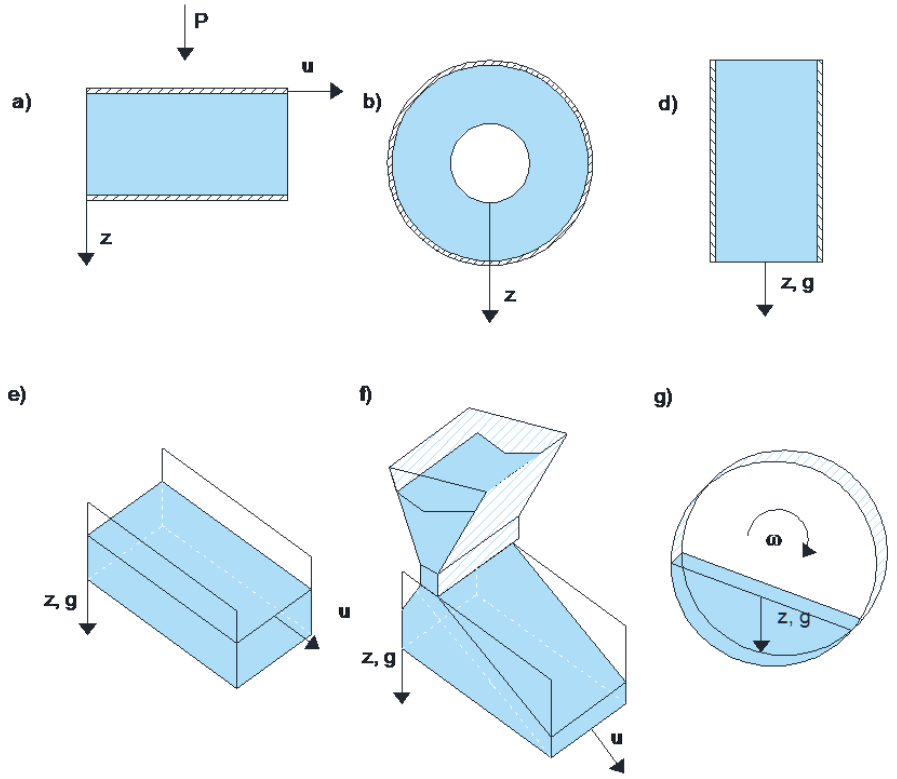


Figure 2.1: Different experimental configurations: a) plane shear stress in absence of gravity, having linear velocity and constant concentration across the cell, b) Couette flow, characterized by a parabolic profile of the velocity, and a decreasing concentration towards the top layers, c) vertical chute flow, having two shear bands near the wall, where the velocity and the concentration assume a minimum. d) Flows down inclines, e) flows at the surface of a pile, and f) rotating drums. Their details are presented and discussed in the paragraph. Reproduced from Forterre and Pouliquen (2008)

ditions or when the granular matter is particularly treatable. The above-mentioned phenomena are only a part of the observable features of the granular material. In the next paragraphs we will review only some aspects useful to the goal of the thesis.

## 2.2 Experimental studies

Dry granular flows have been widely analysed in the recent decades both experimentally and numerically, pointing out the complexity of their behaviour. As concern steady flows, GDR-MiDi (2004) gave a classification of the six most studied geometries, dividing them in confined and free surface flows (see figure 2.2). The plane shear geometry (a), the Couette flow (b) and the vertical chute flow (c) belong to the first category, while the inclined plane (d), the flow at the surface of a pile (d) and in a rotating drum (e) fall in the second category.

Above all, the inclined plane is one of the most interesting and discussed set-

up, because of its simplicity and because of its relevance in the geophysical context and industrial applications. Since the present work dealt with mono-dispersed and dry granular materials down inclines, in the following paragraphs we review the works made on this configuration, presenting the relevant features for two different conditions: flows on a fixed bed and flows on a erodible base.

### 2.2.1 Flows on fixed bed

The inclined plane geometry is shown in figure 2.2 (d). It consists of a granular layer of thickness $h$ that flows down a rough or flat plane inclined at an angle $\theta$ with respect to the horizontal. Disregarding the instabilities issues, the fingering process and other particular features, the most important findings on uniform and steady flow over a rigid base can be summarized as follows:

1. **Flow threshold**: steady uniform flows occur only above a minimum flow depth, $h_{stop}(\theta)$, which decreases with an increasing angle of inclination between the base and the horizontal (Pouliquen, 1999; Forterre and Pouliquen, 2008):

$$h_{stop}/d = B\frac{\tan\theta_2 - \tan\theta}{\tan\theta - \tan\theta_1} \tag{2.1}$$

   where $d$ is the grain diameter, $\theta_2$ is the critical inclination above which the flow accelerates (eg. Azanza *et al.*, 1999; Silbert *et al.*, 2003, 2001; Holyoake and McElwaine, 2012) and $\theta_1$ is the critical inclination below which the flow does not occur. The two angles are fit parameters together with $B$, and they depend on the bulk material and the rough boundary conditions.

2. **Discharge relation**: in GDR-MiDi (2004) and Pouliquen (1999) a power scaling has been proposed $U \propto h^n$, with $n = 3/2$, at any fixed angle of inclination, which is in contrast with granular flows down flat inclines, where $n = 1/2$. Ancey (2001) showed that the exponent varies according the Froude number.

3. **Density profile**: the volume fraction is almost constant through the flow depth, except from the boundaries. It decreases with increasing angle of inclination (Silbert *et al.*, 2001; GDR-MiDi, 2004; Kumaran, 2009).

4. **Velocity profile**: far from the boundaries and for sufficiently large flow depths the velocity profile is consistent with the Bagnold scaling (Mitarai and Nakanishi, 2005; Silbert *et al.*, 2001)

$$u(y) = u_h\left[1 - (1 - y/h)^{1.5}\right] \tag{2.2}$$

while near the free surface it has a linear trend with the crosswise coordinate $y$. These regions of mismatch apparently enlarge when the inclination decreases. Furthermore, in narrow channels the velocity profiles become convex (eg. Azanza *et al.*, 1999; Drake, 1990).

5. **Granular temperature**: it follows the prediction of the kinetic theory in the core region, being proportional to the the square of the shear rate $T \propto \dot{\gamma}^2$. It assumes a S-shaped profile with the flow depth (Silbert *et al.*, 2003, 2001), displaying two maxima at the bottom and at the surface and it increases with $\theta$.

6. **Parameter dependency**: Numerical simulations have shown that while the normal coefficient of restitution does not effect strongly the flow features, the internal friction has a more important role. Brodu *et al.* (2013) show that, compared to the bumpy base scenario, flows on flat frictional surfaces involve a much faster overall velocity, thanks to the presence of a basal layer of rolling grains, upon which the main bulk of the flow slides (Kumaran and Bharathraj, 2013). The flow profiles are very different in the two cases, there is shearing throughout the height for the flow over a bumpy base, while the flow over a flat, frictional base consists of a thin mobile fluidised layer of particles at the bottom supporting a plug flow above. According to Mitarai and Nakanishi (2005) the bottom roughness does not extend its influence to the core region as regards the volume solid fraction and the granular temperature, while Silbert *et al.* (2001) showed that the structure of the flow depends on the bottom, changing from a disordered configuration to a layered one.

### 2.2.2 Flows on an erodible base

While there are some similarities between surface flows down heaps and in rotating drums, the latter one exhibit more peculiarities in the velocity profiles and flow thickness that make them of less interest for the present work. Therefore, for flows on mobile bed, we refer to flows down heaps (2.2 (f)), which can be obtained by pouring grains between two flat plates, separated by a fixed gap $W$. In this conditions, after a transient time the flow becomes steady, a static edge forms in the flume, and a thin flow of particles starts rolling over it. It happens also for mixtures of water and sediments (eg. Tubino and Lanzoni, 1993; Larcher *et al.*, 2007; Armanini *et al.*, 2008), even in this case the behaviour is slightly different.

In the scientific community (eg. (Ertaş *et al.*, 2001; Delannay *et al.*, 2007)) there is a wide agreement on some issues:

1. There is a minimum flow rate below which the flow is intermittent. It is a kind of threshold value that defines the area of existence of the steady regime (eg. Rajchenbach, 1990; Lemieux and Durian, 2000).

2. The free-surface inclination increases with the flow rate for the steady regime. (Ancey and Evesque, 2000; Khakhar *et al.*, 2001; Taberlet *et al.*, 2003). Jop *et al.* (2005) found out that for a constant value of the discharge the free-surface slope increases for decreasing value of the space between the side-walls.

3. The effect of the width is important for narrow channel, as pointed out by Taberlet *et al.* (2003) who measured the variation of the free-surface inclination with the discharge rate, finding that it becomes far larger than the angle of repose, thanks to the confinement of the lateral walls.

4. The velocity profile is linear at the top and it is followed by an exponential tail towards the granular bed, where Komatsu *et al.* (2001) found that it varies with a very slow creeping.

5. The scaling for the shear rate is $\dot{\gamma} = \sqrt{g/d}$, and the dependence of $\dot{\gamma}$ on the flow rate is weak.

## 2.3 Theoretical approaches

A granular flow is a multiphase process, where momentum transport is mainly due to the dynamics of the grains rather than to the interstitial fluid (if any). A continuous approach is widely adopted to treat this kind of problem mathematically, and in the last decades most efforts have been spent to determine the rheological laws of these materials, trying to express the stress tensor as a function of the macroscopic variables that can be measured.

A granular flow can undergo different rheological behaviours, depending on the type of collisions that occur among particles. Three main regimes have been identified related to granular materials, and for each of them different models have been developed to describe their features. By considering the work of Lois *et al.* (2006), we can distinguish these three flow regimes:

- *the collisional regime or gas phase*, which is characterized by low concentration and high deformation rates. It has a gas-like behaviour, since each particle moves independently of its nearest neighbours, and interacts with other particles only by collisions. Constitutive equations are directly derived by the gas

kinetic theory with modifications to account for the more dissipative nature of the process.

- *the frictional regime or solid phase*, when granular materials behave as elastic solid under quasi-static deformation, and the solid volume fraction is almost equal to the loose packing concentration. It is studied using modified plasticity model based on a Coulombian friction model.

- *the intermediate region or liquid phase*, where short and long-term interactions coexist. Temporary force networks can develop.

The following sections survey the principle features of the mentioned theories.

### 2.3.1 Collisional regime

A first formulation of the rheology of granular materials at high shear rates was done by the pioneering work of Bagnold (1954), who studied buoyant particles in a plane shear configuration. He asserted that both normal and shear stresses for highly sheared flows are proportional to the square of the shear rate, and are correlated to each other by a Coulombian relation through the friction angle of the material. The so called "Bagnold scaling" was also verified by several experimental works (Mitarai and Nakanishi, 2005; Silbert *et al.*, 2001) and it has been extensively used in the description of granular flows in the collisional regime. However, the model is not able to reproduce important aspects of granular materials, predicting a constant concentration across the flow depth, or a linear correlation between the stresses.

A more physical based approach for collisional regime arises from the analogy between the molecules of gases and particles in granular flows, where both the constituents are sparse and free to move in every direction. (Campbell, 1990; Goldshtein and Shapiro, 1995; Goldhirsch, 1999). Jenkins and Richman (1985); Jenkins and Hanes (1998); Jenkins and Savage (1983) extended the kinetic theory for dense gases to granular materials, with the aim of deriving a set of continuum equations (typically mass, momentum and energy conservation) entirely from microscopic models of individual particle interactions.

The main difference between the two flows is due to the fact that grains are inelastic, and part of their energy is dissipated during the collisions. Therefore, granular flows always need a source of energy to remain in motion and they are subject to a series of processes that do not take place in granular gases. The concept of granular temperature plays an important role in kinetic theory, and it is a measure of the particles agitation within the ensemble, taking part into generating pressures and governing the momentum, mass and energy transfer processes.

Kinetic theory has been developed under some strict hypothesis that remain valid as far as the collisions are the predominant mechanism of interactions among particles. Then it becomes to fail to predict the complete dynamics of granular flows. Attempts to extend their validity to other regimes were made by Lun and Savage (1987), including friction or introducing new length scales, which account for the presence of force chains (Jenkins, 2006, 2007).

This section is devoted to a brief description of the kinetic theory for granular gases and the derivation of the rheological function used to describe these flows. It follows the review paper of Goldhirsch (1999)

### Standard kinetic theories

They are developed under the assumptions of

1. spherical particles;
2. monodisperse system;
3. frictionless particles;
4. constant coefficient of restitution;
5. instantaneous collisions (that comes from the assumption of rigidity);
6. binary collisions;
7. molecular chaos, and isotropy.

Let's consider an assembly of particles that fit the previous requirement, where $d$ is the diameter of the spheres and $m$ is the mass. The inelasticity of the collisions can be taken into account by introducing the normal coefficient of restitution $e_t$, which correlates the normal components of the pre- and post-impact. Therefore the collision between two particles 1 and 2 is described by:

$$\mathbf{g}' \cdot \mathbf{n} = -e_n \left( \mathbf{g} \cdot \mathbf{n} \right) \tag{2.3}$$

where $\mathbf{n}$ is the unit vector pointing from the center of particle 1 to that of particle 2, $\mathbf{g} = \mathbf{v}_1 - \mathbf{v}_2$ and $\mathbf{g}' = \mathbf{v}_1' - \mathbf{v}_2'$ are the relative velocities before and after the collision. The coefficient of restitution $e_n$ is considered constant, although it depends on the velocity before the impact and on its duration. It varies from 0, for collisions that are completely inelastic, to 1, for perfectly elastic particles, for which there is no dissipation.

The macroscopic quantities of the granular flows (density, velocity and granular temperature) are derived by the equations that describe particle-particle collisions by employing statistical mechanics. The operation is possible by defining the single particle distribution function $f(\mathbf{v}, \mathbf{x}, t)$, which specifies the probability to find particles with velocity $\mathbf{v}$ at point $\mathbf{x}$ and time $t$. Its integration over the volume of the velocity space leads to the number $n$ of particles per unit volume present at $\mathbf{x}$ in the time $t$:

$$n(\mathbf{x}, t) = \int f(\mathbf{v}, \mathbf{x}, t) d\mathbf{v}. \tag{2.4}$$

The single-particle distribution function is useful to define the average $\langle\,\rangle$ of a property $A$ in the system, at time $t$ by:

$$\langle A \rangle = \frac{1}{n(\mathbf{x}, t)} \int A\, f(\mathbf{v}, \mathbf{x}, t) d\mathbf{v}. \tag{2.5}$$

So that the three hydrodynamic mean fields $\rho$ (the mean mass density of the system), $\mathbf{v}$ (the mean velocity of the flow) and $T$ (the macroscopic granular temperature) can be defined as:

$$\begin{aligned} \rho &= m\, n = m \textstyle\int f(\mathbf{v}, \mathbf{x}, t) d\mathbf{v} \\ \mathbf{u} &= \langle \mathbf{v} \rangle = \tfrac{1}{n(\mathbf{x},t)} \textstyle\int \mathbf{v}\, f(\mathbf{v}, \mathbf{x}, t) d\mathbf{v} \\ \tfrac{3}{2} T &= \tfrac{1}{2} \left\langle \mathbf{V}^2 \right\rangle = \tfrac{1}{n(\mathbf{x},t)} \textstyle\int \tfrac{1}{2}\, \mathbf{V}^2\, f(\mathbf{v}, \mathbf{x}, t) d\mathbf{v} \end{aligned} \tag{2.6}$$

where $\mathbf{V} = \mathbf{v} - \mathbf{u}$ is the particle fluctuating velocity. $T$ is the average fluctuating kinetic energy per unit of mass.

Following the standard procedure, the temporal evolution of a generic function $\psi(\mathbf{v}_1)$ of the velocity can be written as:

$$\frac{\partial}{\partial t} \langle n\, \psi \rangle + \frac{\partial}{\partial x} \cdot \langle n\, \psi \mathbf{v}_1 \rangle = \int \psi(\mathbf{v}_1) I(f,\, f) d\mathbf{v} \tag{2.7}$$

where $I(f,\, f)$ is called binary collision integral, and it represents the rate of change due to the collisions among particles. It can be expressed by means of the two-particle distribution function $f_2(\mathbf{v}_1, \mathbf{x}_1, \mathbf{v}_2, \mathbf{x}_2)$, which, as the single-particle distribution function, defines the probability to find particles with velocity $\mathbf{v}_1$ and $\mathbf{v}_2$ at location $\mathbf{x}_1$ and $\mathbf{x}_2$ at the time $t$.

Under the assumptions of binary collisions, rarefied system and molecular chaos, the two-particle distribution functions can be given in terms of the product between the single particle velocity distributions

$$f_2(\mathbf{v}_1, \mathbf{x}_1, \mathbf{v}_2, \mathbf{v}_2) = f(\mathbf{v}_1, \mathbf{x}_1, t) f(\mathbf{v}_2, \mathbf{x}_2, t). \tag{2.8}$$

So the collision integral assumes the form of:

$$I(f,f) = \left(\frac{\partial}{\partial t} + \mathbf{v}_1 \cdot \frac{\partial}{\partial \mathbf{x}_1}\right) f(\mathbf{v}_1, \mathbf{x}_1, t) =$$
$$d^2 \int d\mathbf{v}_2 \int \Theta(\mathbf{g}\cdot\mathbf{n})(\mathbf{g}\cdot\mathbf{n}) \left[\frac{1}{e_n^2} f(\mathbf{v}_1', \mathbf{x}_1, t) f(\mathbf{v}_2', \mathbf{x}_2, t) - f(\mathbf{v}_1, \mathbf{x}_1, t) f(\mathbf{v}_2, \mathbf{x}_2, t)\right] d\mathbf{n}$$

where the Heaviside step function $\Theta$ selects only the couple of particles that are colliding.

The balance laws for $\rho_s$, $\mathbf{u}$ and $T$ result from the transport equation (2.7), when $\psi$ is $m$, $m\mathbf{v}$ and $m\mathbf{v}^2/2$.

Therefore, the hydrodynamic equations of motion are:

$$\frac{D\rho_s}{Dt} + \rho_s \frac{\partial u_i}{\partial x_i} = 0, \tag{2.9}$$

where $D/Dt$ is the material derivative $\partial/\partial t + \mathbf{u}\cdot\nabla$

$$\rho_s \frac{Du_i}{Dt} = -\frac{\partial \sigma_{ij}}{\partial x_{ij}}, \tag{2.10}$$

where $\sigma$ is the stress tensor and

$$\rho_s \frac{DT}{Dt} = -2\frac{\partial u_i}{\partial x_j}\sigma_{ij} - 2\frac{\partial q_j}{\partial x_j} - \rho_s \Gamma; \tag{2.11}$$

where $\mathbf{q}$ is the granular heat flux and $\Gamma$ the collisional rate of dissipation per unit volume. The hydrodynamic description is completed when constitutive relations for $q$, $\sigma$ and $\Gamma$ are given in terms of the hydrodynamic variables (fields).

**Derivation of the constitutive relations** The equations written in the previous paragraph correspond to the Boltzmann formulation, and they apply to very dilute flows. An extension to higher density gases was derived by Enskog, who introduced the pair correlation function $g_0$ in the definition of the two-particle distribution function. Thanks to this element, the collision frequency is increased by a factor that accounts for the spatial correlations between two colliding molecules in a denser fluid, even though the procedure does not consider any correlation among pre and post impact velocities.

Different approaches have been used to derive constitutive equations, by employing different approximation of the pair distribution function. We will refer to the

formulation proposed by Jenkins and Hanes (1998).

**The shear stress tensor** The stress tensor can be written as:

$$\sigma_{ij} = -p\delta_{ij} + \mu\left(\frac{\partial u_i}{\partial x_j} + \frac{\partial u_j}{\partial x_i}\right) \tag{2.12}$$

where the particle pressure is expressed through the relation:

$$p = f_1 \rho T \tag{2.13}$$

with $f_1 = \phi\,(1 + 4\phi g_0 \eta_p)$ The pressure relation is similar to the equation of state for gases $p = R\,\rho\,T$, where the thermodynamic temperature is substituted by the granular temperature $T$. The coefficient $\eta$ is correlated to the particle elasticity through the relation $\eta = (1 + e)\,/2$ The function $g_0$ is the radial distribution function, which takes into account the reduction of the space in which particles can move freely. It is a measure of the density distribution of the grains within the ensemble, and it can be have different formulations according the range of concentration for which they are valid. We will consider the distribution function introduced by Lun and Savage (1986):

$$g_0 = \frac{1}{\left(1 - \phi/\phi^*\right)^{2.5\phi^*}} \tag{2.14}$$

The viscosity $\mu$ in equation (2.12) is defined by the means of the square root of the granular temperature, as the velocity scale $\sqrt{T}$, and by the means of the diameter $d$ as length scale

$$\mu = f_2 \rho d \sqrt{T} \tag{2.15}$$

The constant $f_2$ depends on the dynamic of collisions and its expression is reported in table 2.3.1 according the definitions suggested by Lun and Savage (1986).

**Energy Balance** After adopting a proper definition for the particle distribution function, the energy balance written in equation (2.11) can be reformulated as:

$$\frac{3}{2}\rho_s \phi\left(\frac{\partial T}{\partial t} + u_j \frac{\partial T}{\partial x_j}\right) = \frac{\partial}{\partial x_j}\left(k_T \frac{\partial T}{\partial x_j}\right) + \mu\left(\frac{\partial u_i}{\partial x_j} + \frac{\partial u_j}{\partial x_i}\right)^2 - f_5 \rho_s \frac{T^{1.5}}{d} \tag{2.16}$$

where

$$k_T = f_4 \rho d \sqrt{T} \tag{2.17}$$

Table 2.1: Table of the functions used in equations (2.12),(2.13) and (2.16)

| |
|---|
| $f_1 = \phi\,(1 + 4\phi\,\eta_p g_0)$ |
| $f_2 = \frac{5\sqrt{\pi}}{96\eta_p(2-\eta_p)}\left(1 + \frac{8}{5}\eta_p\,\phi g_0\right)\left(\frac{1}{g_0} + \frac{8}{5}\eta_p(3\eta_p - 2)\phi\right) + \frac{8/5}{\sqrt{\pi}\eta_p\,\phi^2\,g_0}$ |
| $f_4 = \frac{25\sqrt{\pi}}{16\eta_p(41-33\eta_p)}\left(1 + \frac{12}{5}\eta_p\,\phi\,g_0\right)\left(\frac{1}{g_0} + \frac{12}{5}\eta_p^2(4\eta_p - 3)\phi\right) + \frac{4}{\sqrt{\pi}\eta_p\,\phi^2\,g_0}$ |
| $f_5 = \frac{12}{\sqrt{\pi}}\phi^2 g_0\,(1 - e_n^2)$ |
| $g_0(\phi) = (1 - \phi/\phi_*)^{-2.5\phi_*}$ |
| $\eta_p = \frac{1+e_n}{2}$ |

The equation shows that the variation of the kinetic energy (the first term) is balanced by the three terms at the right side, which represent:

1. the diffusion, where $k_T$ is diffusion coefficient;
2. the work done by the tangential stresses;
3. the energy dissipation, due to the inelasticity of the collisions.

**Extended kinetic theory**

Standard kinetic theory has been developed for dilute systems, where the solid concentration remains lower than $\phi = 0.49$ and particles are free to move and collide in every direction. For higher values the system becomes ordered (Azanza *et al.*, 1999), and the hypothesis of uncorrelated velocities breaks down. As shown by the numerical simulations of Mitarai and Nakanishi (2005) and Lois *et al.* (2006), in these conditions standard kinetic theory overestimates the rate of collisional dissipation $\Gamma$, which decreases as the collisions among the particles become more frequent. In fact, when the spheres experience repeated collisions, the process of energy dissipation is not controlled anymore by the single particle, but it is influenced by the extension of the chain of contacting grains. Therefore in the dissipation term of the energy, the grain diameter is replaced by a kind of length of particle correlations, while the stresses are not modified :

$$\Gamma = \frac{24}{\pi^{1/2}}\frac{\rho g_0}{L}(1 - e)T^{3/2} \tag{2.18}$$

The length $L$ is derived by Jenkins (2006, 2007), supposing that the spheres are forced to be in contact along the principle compressive axis of the shearing, and

that this order is contrasted by the inner kinetic agitation of the flow. Therefore, for uniform and steady conditions, Jenkins ended up with this simple balance:

$$cG^{1/2}D_{ij}L_j + (LT^{1/2}/d^2)L_i = 0 \tag{2.19}$$

where $c$ is a constant of order one. The correlation length can be derived by making an approximation to the energy balance

$$Su' - \Gamma \tag{2.20}$$

where $S$ is the tangential stress, and $u'$ the shear rate. Therefore, its expression becomes:

$$\frac{L}{d} = \frac{1}{2}\left[\frac{30}{J}(1-e)c^2G\right] \tag{2.21}$$

### 2.3.2 Frictional regime

The frictional behavior becomes important at high concentration, when particles approach the random packing fraction, moving at very low shear rates. In this case particles are close together and interact mainly through prolonged and multi-grain contacts. Therefore, forces are transmitted through the point of contact, and form chains that span throughout the granular media. They consist of normal reactions and the associated tangential forces due to the friction.

For free-surface flows, this regime becomes predominant in the lower layers of the depth, near the static deposit as shown by Armanini *et al.* (2005). However, Armanini *et al.* (2009) proved that it is not confined in a specific region of the flow but it coexists with the collisional regime.

A large number of constitutive relations have been proposed to account for the mechanical behaviour of the granular media in the quasi-static regime. They generally arise from soil mechanics and are based on the plasticity or visco-plasticity theories (Schofield and Wroth, 1968), or on models of sliding layers that generate frictional forces (eg. Roscoe *et al.*, 1958; Roux and Radjai, 1998; Roux and Combe, 2002). In this models the shear stress is considered proportional to the normal stress, while the normal stress is related to the bulk density.

### 2.3.3 Intermediate regime

Most of the constitutive models used to predict the behaviour in the whole range of flow regimes are based on the decomposition of the stress tensor into the sum of "rate-dependent" and "rate-independent" contributions (Savage, 1984, 1998; Johnson and

Jackson, 1987; Johnson *et al.*, 1990). In all these works the rate-independent part is defined by a Coulomb law relation between the shear and the normal stresses, while the rate-dependent contribution is modelled by using kinetic theory.

There have been also studies (Louge, 2003; Louge and Keast, 2001), which have been attempted to separate the flow into a bulk flow and boundary layers, and solve them separately. The balance equations in the different regions are different, as the criteria chosen to patch the solutions in different locations of the flow. However, in a physical system the transition from boundary layers to the bulk is gradual and not located in any specific point of the flow. So that, the solution of these models is a rough approximation of the reality, and it is dependent on where the union of the different solutions is done.

A phenomenological description of dense flows was given both by Aranson and Tsimring (2002) and by Bouchaud *et al.* (1994), who described the transition between the flowing and static components of the granular system through an order parameter, dynamically coupled with the equations for the flow velocity and shear stresses. However this model, as the layered ones, work well when a sharp division exists between static and rolling grains. As over-mentioned, this boundary is not well defined in granular systems.

### 2.3.4 The $\mu$ (I) rheology

The $\mu$ (I) rheology was proposed by Ancey and Evesque (2000) and Jop *et al.* (2006), obtaining a widely success among the scientific community for its simplicity and adaptability.

It was derived by a scaling analysis of a compilation of experimental data obtained for granular flows in different configurations GDR-MiDi (2004) and it is based on the definition of a dimensionless parameter called the Inertia number:

$$I = \frac{\dot{\gamma} d}{\sqrt{P/\rho}} \tag{2.22}$$

which can be interpreted as the ratio between two time scales: the time of the microscopic rearrangements $d/\sqrt{P/c}$, where $P$ is the confining pressure and $d$ the grain diameter in a simple shearing configuration, and the macroscopic scale of the flow, assumed equal to the mean deformation $\dot{\gamma}^{-1}$. It is equivalent to the square root of the Savage or Coulomb number introduced previously by some authors as the ratio of the collisional stress and of the total stress (Savage, 1984; Ancey *et al.*,

1999) The effective friction angle is thus expressed as:

$$\mu(I) = \frac{\tau}{P} = \mu_s + \frac{\mu_2 - \mu_s}{I_0/I + 1} \tag{2.23}$$

where $\mu_s$ and $\mu_2$ are the tangent respectively of the static angle and the dynamic angle introduced in the flow rule of Pouliquen. $I_0$ is a constant dependent on the material properties of the flow. According to this equation the friction angle increases during the transition from the quasi-static regime ($I \to 0$) to the kinetic regime ($I \gg I_0$).

This simple model augmented by a linear relation for the volume fraction

$$c = c_{max} - (c_{max} - c_{min})\, I \tag{2.24}$$

may describe several types of granular flow (da Cruz *et al.*, 2005; Jop, 2008; Jop *et al.*, 2005).

Various constitutive relations based on the $\mu(I)$ rheology have been developed for different configurations. However it does not apply when the particle fluctuations are predominant and close to the boundaries. Despite its success the, $\mu$(I) model has some important limits, which make it weak in situations different from those ones used to derive it. The critical points are:

1. The model accounts for the presence of two angles, one of which is a the dynamical angle. Physically this parameter depends on the flow-field and it is not a constant as proposed by the authors.

2. The model implicitly does not consider the granular temperature, assuming a local equilibrium between the kinetic energy and its dissipation. As a consequence, the equations used to express the stresses are not able to predict the transition to a dilute regime, being applicable only where particles are characterized by sustained contacts.

3. The variation of the concentration with the inertial parameter can be used only where the stresses are mainly frictional.

4. Although the model was developed from experiments of flows down inclined planes, it fails to predict the velocity profiles for shallow flows or for confined flows.

5. As concern flows in confined geometry, the model needs to introduce an additional length scale, corresponding to the width.

### 2.3.5 A heuristic model

The model was proposed by Armanini *et al.* (2014), and it adopts the kinetic theory for the collisional regime and a specific model for the frictional part, with a changing friction angle that depends on the local kinematics. The dimension-less parameter that is used to describe the kinematic properties of the flow is the Savage number, which coincides with the square of the inertia number $I$. The relation between the two quantities is the following:

$$\tau^{fric} = p^g \tan\phi^{fric} \frac{I_{s0}}{I_s + I_{s0}} \tag{2.25}$$

that was chosen in order to tend asymptotically to a pure Coulombian shear stress at the loose bed, and to vanish for larger values of $I$, corresponding to a collisional regime. In this expression $p^g$ is the total granular pressure, $\phi^{fric}$ is the internal friction of the material, while $I_{s0}$ is a parameter that depends on the bulk properties of the assembly of grains.

As for the tangential component, also the frictional pressure is written in terms of the Savage number, as:

$$p^{fric} = p^g \frac{I_{s0}}{I_s + I_{s0}} \tag{2.26}$$

where $p^{fric} = p^g - p^{coll}$. The collisional pressure is defined according the relationship written before.

In an uniform flow, calling the direction of the motion 1 and the vertical axis 2, the rheological relationship and the kinetic energy balance become:

$$\tau^g_{12} = p^g \tan\phi^{fric} \frac{I_{s0} p^g}{I_{s0} p^g + \left(\frac{\partial u^g_1}{\partial x_2} d\right)^2 \rho} + \rho\, f_2\, d\, T^{0.5} \frac{\partial u^g_1}{\partial x_2} \tag{2.27}$$

$$p^g = p^g \frac{I_{s0}}{I_s + I_{s0}} + \rho f_1 T \tag{2.28}$$

$$0 = \frac{\partial}{\partial x_2}\left(k_T \frac{\partial T}{\partial x_2}\right) + \mu^{coll}\left(\frac{\partial u^g_1}{\partial x_2}\right)^2 - f_5 \rho \frac{T}{d} \tag{2.29}$$

where the symbols are the same given in the previous paragraphs.

## 2.4 Collisional properties of particles: concepts

Dynamics of granular flows are governed by grain interactions, which are responsible for the exchange of momentum and energy in the system at least in the collisional

regime. Forces are transmitted through instantaneous or enduring contacts among particles, determining the rate of dissipation and production of granular temperature. Therefore, the mechanism of particle collisions is crucial to describe granular flows and to simulate them numerically. Simple models have been developed based on the physics of rigid bodies, as the Walton description reported below.

### 2.4.1 Impact model

Individual collisions are treated using the simplified theory proposed by Walton and Braun (1986). In this approach the dynamics of the impact are ignored and the effects of plastic deformations and heat dissipation are included in three parameters, which express a correlation among the post- and pre-impact values of the kinematic variables. The three parameters can be determined experimentally and are suitable to characterize the main features of collisions.
Consider a rigid sphere of diameter $d_p$, velocity at the center of mass $\mathbf{c}_i$ and spin $\omega_i$ before the impact. At the contact point the velocity is

$$\mathbf{g}_i = \mathbf{c}_i - (d_p/2)\boldsymbol{\omega} \times \mathbf{n} \tag{2.30}$$

The subscript $i$ stands for pre-collisional velocities, while the subscript $r$ is for post-collisional variables.

Velocities before and after the impact are related through the following relationships:

$$\begin{cases} m(\mathbf{c}_r - \mathbf{c}_i) = \mathbf{J} & (a) \\ \\ \dfrac{m d_p^2(\omega_r - \omega_i)}{10} = -\dfrac{d_p}{2}\mathbf{n} \times \mathbf{J} & (b) \end{cases} \tag{2.31}$$

where the rolling friction has been neglected as it tends to zero for spheres. At the contact point:

$$\begin{cases} \mathbf{g}_i = \mathbf{c}_i - (d_p/2)\boldsymbol{\omega} \times \mathbf{n} & (a) \\ \mathbf{g}_r = \mathbf{c}_r - (d_p/2)\boldsymbol{\omega} \times \mathbf{n} & (b) \end{cases} \tag{2.32}$$

Note that $\mathbf{n} \cdot \mathbf{g} = \mathbf{n} \cdot \mathbf{c}$. Now the restitution coefficients for the normal and tangential components of the velocities can be introduced:

$$(\mathbf{n} \cdot \mathbf{g}_r) = -e\,(\mathbf{n} \cdot \mathbf{g}_i)\,; \tag{2.33}$$

For collisions in which there is *no sliding* of the contact point

$$(\mathbf{n} \times \mathbf{g}_r) = -\beta_0 (\mathbf{n} \times \mathbf{g}_i) ; \tag{2.34}$$

While for collisions in which there is *sliding* it is assumed that the Coulomb friction acts during the sliding, so that the normal and tangential impulse are related by the coefficient of friction $\mu \geq 0$

$$|\mathbf{n} \times \mathbf{J}| = \mu (\mathbf{n} \cdot \mathbf{J}) \tag{2.35}$$

In some authors the same coefficients are defined in relation to the velocity of the centre. Note that $0 \leq e \leq 1$, like $0 \leq \beta_0 \leq 1$ and $\mu_0 \geq 1$

### 2.4.2 Binary collisions

Binary collisions of spherical particles are assumed to occur instantaneously and to be fully described by three parameters: the normal restitution, tangential restitution and friction, which can correlated to the pre- and post-collision velocities.

Depending on what happens at the point of contact they an be of two types:

1. If the point of contact slips during the collision the interaction is said to be one of "slipping " contact, and the tangential impulse is assumed to be correlated through a Coulombian friction

   $$|\mathbf{n} \times \mathbf{J}| = \mu (\mathbf{n} \cdot \mathbf{J}) \tag{2.36}$$

   For two spherical particles in contact $\mathbf{n}$ is defined as $\mathbf{n} = (\mathbf{r}_1 - \mathbf{r}_2)/|\mathbf{r}_1 - \mathbf{r}_2|$, where $\mathbf{r}_1$ and $\mathbf{r}_2$ are the position of the particle centres

2. Collisions where the point of contact remains "locked" are described as "sticking". In this case the following relation stands:

   $$(\mathbf{n} \times \mathbf{g}_r) = -\beta_0 (\mathbf{n} \times \mathbf{g}_i) ; \tag{2.37}$$

In both cases, as concern the normal component of the relative velocity, the pre and post-collisional value are correlated through the normal restitution coefficient:

$$(\mathbf{n} \cdot \mathbf{g}_r) = -e (\mathbf{n} \cdot \mathbf{g}_i) ; \tag{2.38}$$

### 2.4.3 Collisions with a plate

As in the case of binary collisions, it is assumed that the normal, tangential and the friction coefficient are sufficient to describe the dynamic of the impact. If the initial velocity of rotation is null, the post-collision can be given by the only translation components, and the parameters can be expressed as

$$e = -\frac{\mathbf{c}_r \cdot \mathbf{n}}{\mathbf{c}_r \cdot \mathbf{n}}; \qquad \beta_0 = \frac{\mathbf{c}_r \cdot \mathbf{t}}{\mathbf{c}_r \cdot \mathbf{t}}; \qquad \mu = \frac{|\mathbf{J}_i \cdot \mathbf{t}|}{\mathbf{J}_i \cdot \mathbf{n}} \tag{2.39}$$

where the translational velocity of the mass has been considered null, since its mass can be considered infinite in the analysis.

The parameters can be inferred by using the Maw representation (see Maw *et al.* (1976)), where the non-dimensional post-collision tangential component of relative velocity are defined as:

$$\psi_2 = \frac{\mathbf{c}_r \cdot \mathbf{t}}{\mathbf{c}_i \cdot \mathbf{n}} \tag{2.40}$$

versus the pre-collision tangential component of relative velocity:

$$\psi_1 = \frac{\mathbf{c}_i \cdot \mathbf{t}}{\mathbf{c}_i \cdot \mathbf{n}} \tag{2.41}$$

For sticking collision $\psi_2$ varies with $\psi_1$ as

$$\psi_2 = -\beta_0 \psi_2 \tag{2.42}$$

in the case of sliding regime

$$\psi_2 = \psi_1 + \frac{7}{2}\mu(1+e) \tag{2.43}$$

In the plot two domains can be defined and $\beta_0$ and $\mu$ may be determined either from the slopes and intercepts produced by regression analyses of the two regimes.

Since the coefficients empirically describe the behavior of the system without regard the material properties or system geometry, their validity is restricted to that system for which they are calculated. In the case of binary collisions, a system could be fully described simply by reporting only the particle diameters, compositions, and surface features. However, the behavior of a spherical particle/flat plate system is also dependent upon the plate thickness, material, and support geometry.

## 2.5 Effect of side walls

We will review briefly some approaches to model the effects of the side-walls on the granular flows, referring to flat and smooth walls. We first consider the approach developed by Jenkins (1992)and Jenkins and Louge (1997), who moved in the framework of the kinetic theory, and then we describe the theory of Johnson and Jackson (1987), who developed a heuristic model.

In his theory for boundary conditions Jenkins refers to the Walton theory to describe a collision with a flat plate. He distinguishes between sliding and non-sliding collisions, using the parameter

$$\mu^* = \frac{2}{7}\frac{1+\beta_0}{1+e} \tag{2.44}$$

Considering the ratio between the slip velocity and the square root of the granular temperature $r = \mathbf{g}_0/(3T)^{1/2}$, we have that:

1. for $\mu \geq \mu^*$ the collisions are sticking:

$$\frac{S}{N} = \frac{3}{7}\frac{1+\beta_0}{1+e}r \tag{2.45}$$

2. for $\mu \leq \mu^*$ the collisions are sliding;

$$\frac{S}{N} = \mu \tag{2.46}$$

Therefore, there are two limit cases, one characterized by high values of friction and the other characterized by low values of friction. In the first case particles cannot slide due the large friction and the contact point sticks to the wall and the ratio $S/N$ is proportional to the quantity $r$. In the second case the dynamic angle, defined as the ratio between the tangential and normal stresses at the wall, tends to become equal to the friction $\mu$ remaining always lower than it. From this considerations Jenkins derived also the expression for the flux and dissipation term at the side-walls.

On the contrary, Johnson and Jackson developed their model, adopting an heuristic approach. They observed that the tangential stress exerted by the particles has two contributions coming from the particle collisions and the friction with the wall.

- the frictional part can be assumed equal to $\mathbf{N}_f \tan\delta$, where $\mathbf{N}_f$ is the normal component of the stress and $\tan\delta$ is the friction angle between the material and the wall. (Coulombian assumption)

- on the other hand, the collisional part involves the collision frequency for each particle, the average momentum transferred per collision and the number of particles present near the wall.

This approach has been widely used, especially in numerical simulations, even though the formulation uses some empirical parameter, like the specularity coefficient, whose value is not univocally determined.

# Chapter 3

# Laboratory set-up and data collection

The experimental set-up was designed to simulate free-surface flows of dry granular material over a loose deposit. Measurements of the flow-field were achieved through imaging techniques to have profiles of velocity, concentration and granular temperature for different configurations. A small apparatus was built to measure collisional properties of the particle, while a first version of a home-made device was developed to have a direct measurement of the shear stresses at the walls.

## 3.1 The laboratory channel

The experimental set-up consists of an open channel having transparent side-walls of Plexigas, a hopper to convey the material into the flume, and a tank to collect the grains at the exit of the chute (figure 3.1). The system is an open-circuit, in which the flow rate is controlled by the opening of the hopper, and it is verified by weighting the material collected at the end of the flume in a given lapse of time.

The channel is 2.5 m long and 5 cm wide, but can be narrowed by placing a partition for a length of 1.30 m. The bottom is artificially roughened by coarse sand-paper, and its slope angle can be changed from 0 to 45°, thanks to an hydraulic piston that is mounted upstream.

The outlet section of the flume is closed by a multiple slit gate, used in place of a simple weir to have a better control of the deposit, as it is discussed in 4.2.

### Partition

The channel can be divided in two parts through a thin copper foil (0.6 mm) for a length of 1.30 m (the ratio between the flume length and the stretch involved in the

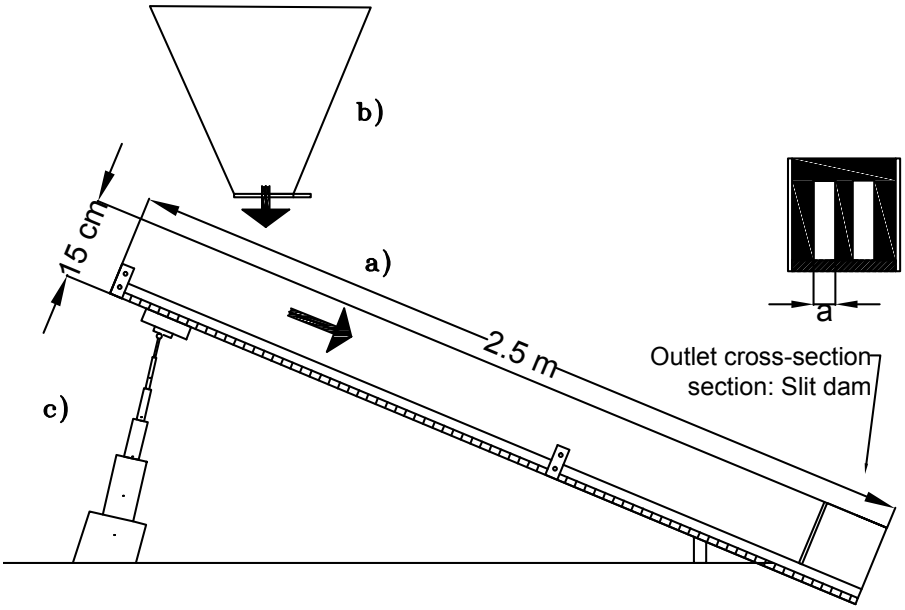


Figure 3.1: Experimental set-up: a) the inclined plane with transparent side-walls; b) the hopper and c) the hydraulic piston to change the slope of the flume.

partitioning is equal to 1.5 ). The foil is fastened to a plastic rod for all its length, apart from 30 cm, where the cameras can be set to record the surface velocity. It can be moved along the flume and along the transverse section thanks to a simple system of carriages. The partition wall is extended to the end of the flume to guarantee the separate measurements of the discharge coming from the two parts.

### Granular materials

The granular material used in the experiments is composed of plastic spheres having a diameter d= $0.55 \pm 0.05$ mm, and a density $\rho_s$= 980 kg/m$^3$. The friction angle is equal to $\theta_s$=$24 \pm 0.05°$, and it was estimated experimentally by measuring the free surface slope of a heap that forms naturally by pouring grains on an horizontal plane.

### The cameras

The two high speed cameras used to measure the flow-field are the FASTCAM X 1024 PCI by PHOTRON. The cameras are able to take 1000 frames per second at the maximum resolution of $1024x1024$ pixels but reducing the resolution the maximum velocity available is 109000 fps. The image size and the frequency were set to have the best compromise for a meaningful recording, considering that they influence also the registration time. The highest acquisition frequency that was used in the present

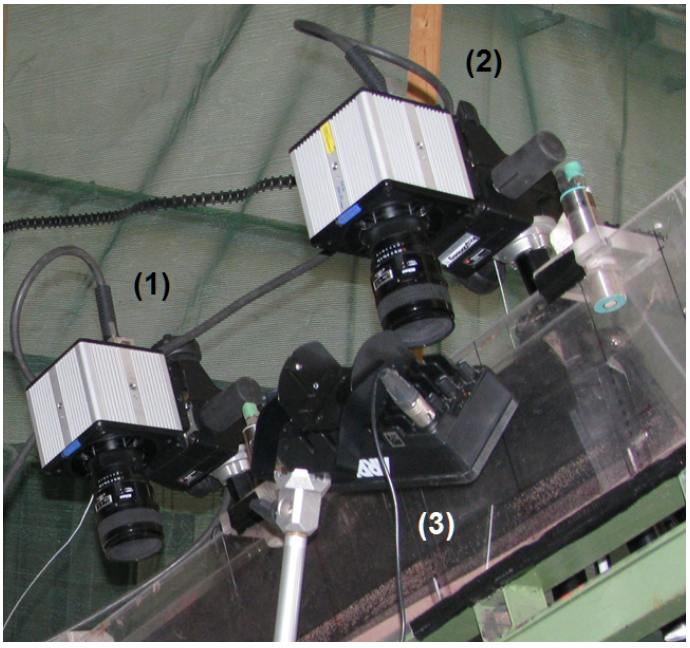


Figure 3.2: Setting for the imaging technique: (1) and (2) are the synchronized cameras, (3) is the lightning system used during the recording.

work is $f_{ac} = 3000$ fps for high flow rates, obtaining a duration of the registration that did not exceed 3 s. At low discharge, the acquisition frequency was limited at $f_{ac} = 1000$ fps, allowing for longer registration of the flow and larger image sizes. The resolution was chosen each time to have the best field of view necessary to compute the velocity profiles in the vertical or in the transversal direction.

The cameras were placed looking down, normal to the channel bottom, to analyse the surface flow-field, or pointing the flow through the Plexigass side-walls, to analyse the vertical structures of the flow.

## 3.2 Measurement techniques

Imaging techniques were used to evaluate the velocity field both from the top surface of flow and from the lateral side-walls. Home made algorithms, developed at the University of Trento were used to analyse the recordings, employing the Voronoï technique developed by by Capart *et al.* (2002) and Spinewine *et al.* (2003). The height of the flowing grains was measured through the erosion method and compared with the measures derived from the velocity profiles.

### 3.2.1 Measurements of the flow-field: the Voronoï technique

The analyses of the flow-field was carried out using the image techniques of Capart *et al.* (2002), developed to estimate the displacements and arrangement of visible

particles on digital frames in the specific case of granular flows.

The method can be included in the class of the particle tracking algorithms, and it exploits the Voronoï tessellation of the space to track particles in subsequent frames of a recording.

In the order, the algorithms used to process the images perform the following operations:

1. identifying the particle centres in the entire sequence of image with a sub-pixels accuracy. Particle images are initially highlighted by applying a Laplacian-of-Gaussian filter, and then their position are identified by pinpointing the local brightness maxima.

2. matching particles in subsequent frames to track them in time. This step is performed by recognizing the similarity between the Voronoï diagrams built on the particle centres of successive frames.

The method is able to track particles even for high density images and different shear rate across the frame. In fact, the polygons divide the space into not-overlapping parts with their own centroid which remain almost unchanged for small time intervals, allowing the identification of the same patterns in subsequent images.

After pairing each particle frame to frame, the velocity vectors are defined as:

$$\mathbf{v}_i^n = \frac{\mathbf{r}_i^{(n+1)} - \mathbf{r}_i^{(n)}}{\Delta t}; \tag{3.1}$$

where $\mathbf{r}_i^{(n)} = (x_i^{(n)}\, y_i^{(n)})$ is the two-dimensional position of the $i$th particle at time $t^{(n)}$, $\mathbf{v}_i^{(n)} = (u_i^{(n)}, v_i^{(n)})$ is the corresponding in-plane velocity in the $x-$ and $y-$ axes oriented in the directions parallel and orthogonal to the flow direction. By using a single camera to record the flow, the out-of-plane velocity component $w_i^{(n)}$ is not computed. A calibrated scale factor allows the transformation from pixel to physical coordinates.

Examples of the procedure are reported in figure 3.2.1

### 3.2.2 Three-dimensional measurements of the flow-field

Some experiments were carried out by using stereoscopic recording to have the reconstruction of the $3D$ velocity field and the three-dimensional Voronoï method was used.

The method shares the main features of pattern recognition with the 2D technique. However, beyond the problem of tracking particles in time, there is also an

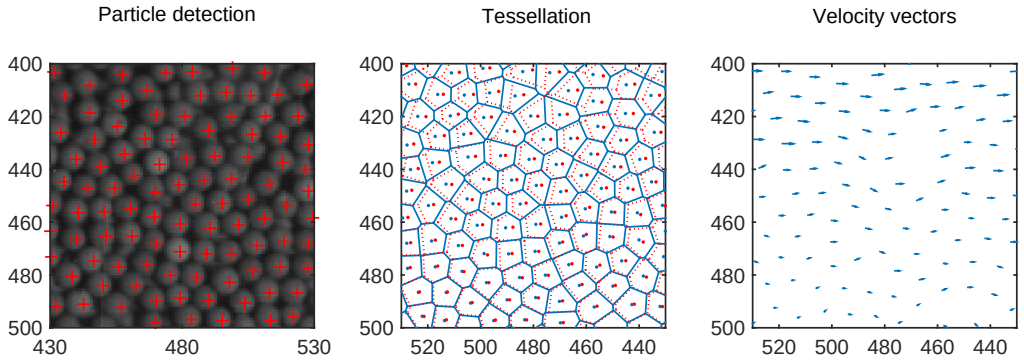


Figure 3.3: The three steps of the Voronoï method: 1) particle detection (red cross superimposed on the particle image), 2) Voronoï tessellation (in figure two consecutive frames are presented together), 3) reconstruction of the velocity field

additional problem of pairing the digital images of the particles seen from two different cameras. Therefore, in this case the procedure is made up of the following steps:

1. identifying particles in each frame that corresponds to a different viewpoint $A$ or $B$ from which the flow is observed;
2. passing from the cameras $\left(\mathbf{R}_P^{(A)} = \left[X_P^{(A)} Y_P^{(A)}\right]\right)$ to the world coordinates ($\mathbf{r}_P = [x_P,\, y_P,\, z_P]$), where $P$ is a generic particle;
3. associating correctly the particles on the two digital frames;
4. finally, matching the same particles also in time.

The transformation of the reference system is obtained by modelling the image formation as a central projection from a virtual camera focal point onto the image plane. So that, the relation between the spatial coordinate of a generic point P and its projection on the image plane is given by the following relation:

$$\alpha \begin{bmatrix} X^{(A)} \\ Y^{(A)} \\ 1 \end{bmatrix} = \left[\mathbf{A}^{(A)}\right] \begin{bmatrix} x \\ y \\ z \end{bmatrix} + \mathbf{b}^{(A)} \tag{3.2}$$

The matrix $\left[\mathbf{A}^{(A)}\right]$ and the vector $\mathbf{b}^{(A)}$ must be calibrated using a set of points whose coordinates are known both in the real world and in the digital frame. The parameter $\alpha$ is a scalar that defines the parametric equation of the ray $AP$ that pass

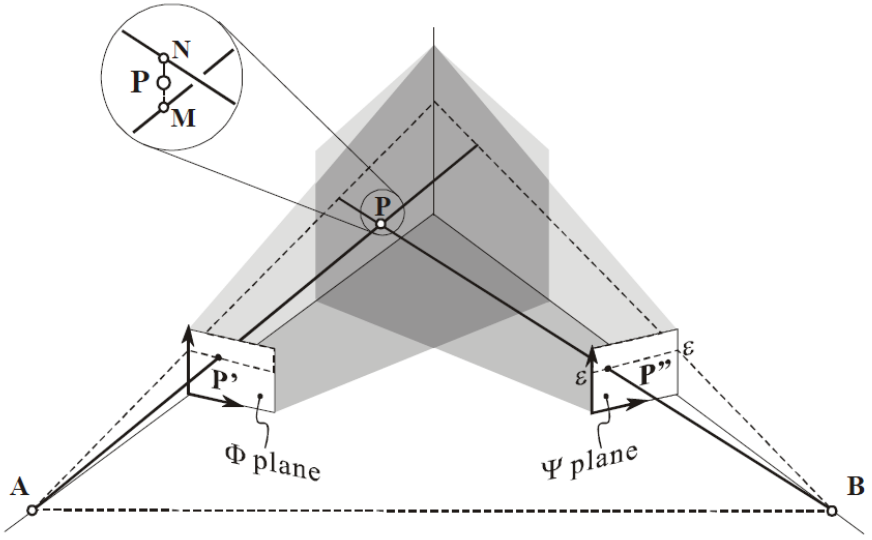


Figure 3.4: Projection scheme: P is the physical point while P' and P" are its image projections on the two stereo views. Points A and B are the focal points of the two central projections. The trace of the epipolar plane is shown in dashed lines. Inset: due to imperfections in the imaging geometry, the two rays may not perfectly intersect. Reproduced by Larcher (2002)

through the point P (see figure 3.4) :

$$\mathbf{r}_{AP}(\alpha) = \mathbf{r}_A + \alpha \mathbf{s}_{AP} \tag{3.3}$$

where $\mathbf{r}_A$ defines the position of the focal point A and $\mathbf{s}_{AP}$ specifies the direction of the ray passing through the point P and its projection on the plane:

$$\mathbf{r}_A = -\left[\mathbf{A}^{(A)}\right]^{-1}\mathbf{b}^{(A)}; \quad \mathbf{s}_{AP} = \left[\mathbf{A}^{(A)}\right]^{-1} + \begin{bmatrix} X^{(A)} \\ Y^{(A)} \\ 1 \end{bmatrix} \tag{3.4}$$

The three dimensional position of a particle seen from two points view can be derived by finding the intersection (almost exact) of the rays $AP'$ and $BP$" that pierce the two image planes passing through the point P. The two lines define a plane, called epipolar plane, whose intersection with the image plane $\Phi$ is a straight line $\epsilon\epsilon$ (epipolar line). This line is the locus of all possible projections of the point P in the image plane $\Phi$ of the physical point that has its projection in the other image plane. The epipolar constraint is very important since it accelerates the matching procedure between the two image frames.

### Calibration

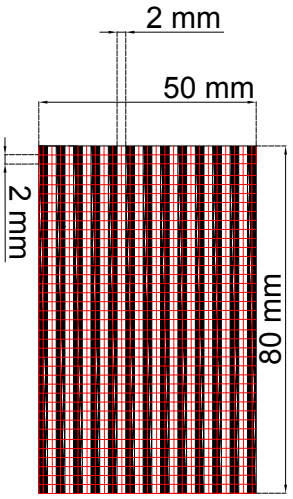


Figure 3.5: Dimensions of the target used to calibrate images for the stereoscopic measurements. Front view in which the net of points is visible. The coordinates of these points are used to calibrate the images.

The calibration allows the transformation from image to physical coordinates. As explained in the previous paragraph, the procedure use a set of points whose positions are known both in the image plane and in the real world. The system written in eq. (3.2) is over-determined if more than 6 calibration points are used, otherwise a least-square procedure is needed to obtain an optimal solution.

From an experimental point of view, the calibration is carried out by placing in the window view of the cameras a target, whose dimensions are well known.

In the case of the small plastic spheres used in the present thesis, the target consisted of a rectangular piece of plastic, high 8 cm and large 5 cm, having a series of humps and hollows. Inside the hollows small holes are cut every 2 mm, while red dots are painted on the humps at the same distance. Together, these points form a regular net of known points on two different planes, the first one at the same level of the side-walls, the other one at a depth of 2 mm from the previous one (see figure 3.5).

The origin of the real coordinates is put at a corner of the target (usually at the left corner at the top of the figure) in order to define the physical coordinates of the calibration points. Once their coordinates are known also in the image plane, through a least-square process the roto-translational matrix is computed.

**Top-view recordings** For top-view recording the calibration process is much more complicated, since it should be done on a plane coincident with the plane

of the flow surface. A small devise was realized to allow the target to be set parallel to the surface, and to be moved along the direction perpendicular to the loose bed (see figure 3.6).

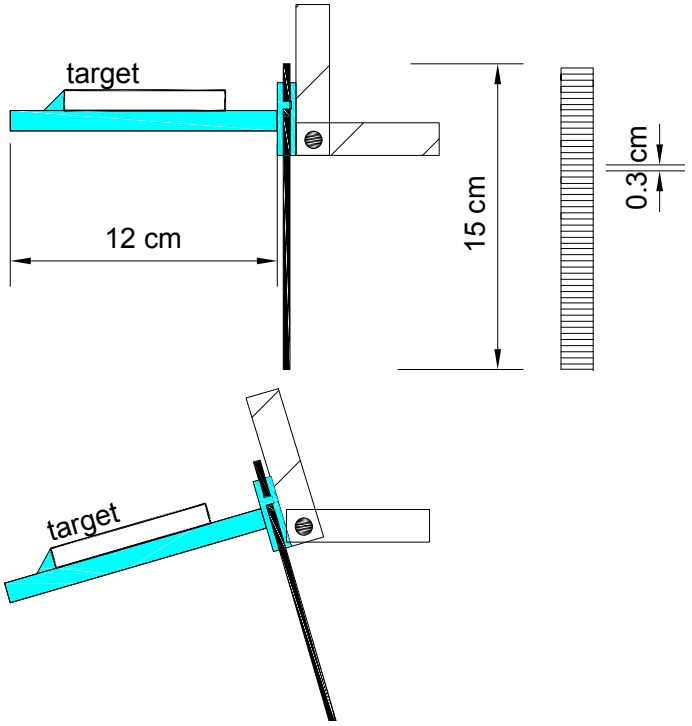


Figure 3.6: System used to move the target for stereoscopic recordings carried out at the top surface. The target is placed on a plastic support that can be tilted with respect to the horizontal and moved up and down, thanks to a beam.

### 3.2.3 Concentration estimation

The two-dimensional images are also used to estimate the volumetric concentration at the wall. As shown by Capart, the point density at the wall can be a poor estimator of the concentration due to the occlusion effects of the particles, while the parameters connected to the shape of the Voronoï diagrams give more reliable measurements. Capart *et al.* (2002) found out that the roundness of the Voronoï polygons is connected to the normalized concentration through a power law, whose coefficients are calibrated through Monte-Carlo simulation.

$$\xi = \frac{4\pi A}{P^2} \tag{3.5}$$

where $P$ is the perimeter of the single polygon, while $A$ is its area. and

$$\frac{c_s}{c_s^{(rcp)}} = \left( \frac{\xi - \xi^{(min)}}{\xi^{(rcp)} - \xi^{(min)}} \right)^b \tag{3.6}$$

where $c_s$ is the solid concentration, superscripts (rcp) and (min) designate the state of random close packing and the dilute state.

Additionally, another indicators reflects the Voronoï "area disorder" and is defined as:

$$\chi_i = \frac{1}{1+\sigma/\mu} \tag{3.7}$$

where $\sigma$ and $\mu$ are a kind of variance and mean value evaluated considering the geometry of the diagrams. As for the roundness factor, also in this case the concentration can be derived following a power-law:

$$\frac{c_s}{c_s^{(rcp)}} = \left( \frac{\chi - \chi^{(min)}}{\chi^{(rcp)} - \chi^{(min)}} \right)^{\gamma} \tag{3.8}$$

where $\chi_0 = 0.80$.

For stereoscopic measurements the local volumetric concentration $c(\mathbf{r})$ can be estimated making use of the 3D Voronoï partition, considering that each polygon contain a single particle:

$$\widehat{c} = \frac{V_P}{volume(V_k)} \tag{3.9}$$

where $V_P = 1/6\pi\, d^3$ is the volume of a single solid particle, and $V_k$ is the volume of the Voronoï polygon.

Due to impenetrability of opaque particles and sidewalls the set of points identified on the two images does not correspond exactly to the physical one, since part of the grains visible from one view-point may not be caught by the other cameras. In addition, particles near the wall occluded those ones that are behind them. For this reason the volumetric concentration can be estimated from the areal concentration $\eta_{0,i}$ defined as:

$$\eta_{0,i} = \frac{1}{area(A_0(V_i))} \tag{3.10}$$

where $A_0$ is the area that the i-th polygon shares with the side-wall. The transformation of the surface concentration to the volumetric one is made by assuming that particle centroids are distributed inside the 3D volume according to a homogeneous Poisson process $\langle \eta_0 \rangle = \chi\, \mu_P^{2/3}$ (where $\chi$ is a stereoscopic coefficient assumed equal to 0.92

$$c_s = V_P \left( \frac{\langle \eta_0 \rangle}{\chi} \right)^{3/2} \tag{3.11}$$

The main difference between the two estimates relay on the fact that in the monocular case, all the visible particles are counted regardless of their distance to the wall. For the stereoscopic case, by contrast, only the near-wall particles are counted and the concentration is derived by purely geometrical considerations,

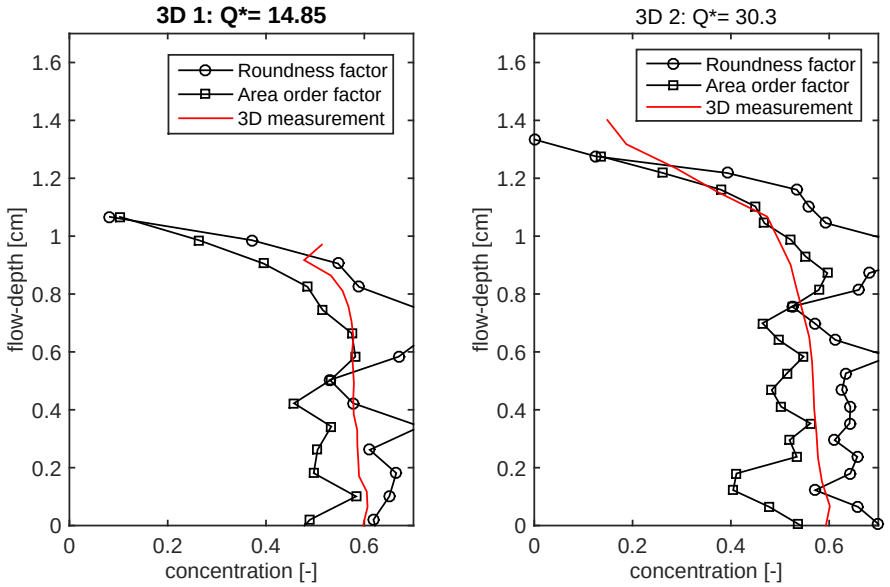


Figure 3.7: Comparison between the concentration estimated through two-dimensional analysis and three-dimensional measurements. The concentration estimated using the stereoscopic recordings is in the middle between the concentration derived by the area disorder factor and the roundness factor

without calibration parameters.

Even if the two measurements are in good agreement as it is shown in figure 3.7, for $c_s > 0.55$ the stereoscopic measures are more reliable, since the two-dimensional estimates are uncertain.

### 3.2.4 Granular temperature measure

The granular temperature represents a measure of the kinetic energy own by the particles, and it is defined as:

$$T = \frac{1}{3}\left(\langle u_i'^2\rangle + \langle v_i'^2\rangle + \langle w_i'^2\rangle\right) \tag{3.12}$$

where $T$ is the granular temperature, $u_i' = u_i' - \langle u\rangle$, $v_i' = v_i' - \langle v\rangle$ and $w_i' = w_i' - \langle w\rangle$ are the velocity fluctuations of the granular phase along the direction parallel and normal to the bed, and along the direction normal to the side-wall. The latter component is measured only in the experiments conducted by stereoscopic measurements.

The brackets designate a spacial average performed in horizontal layer, as explained in the section 4.1.1

## 3.3 Flow-depth measurements

In some experiments the flow depth was measured by using the erosion method proposed by Jop *et al.* (2005) in order to reconstruct the evolution of the flow thickness across the width.

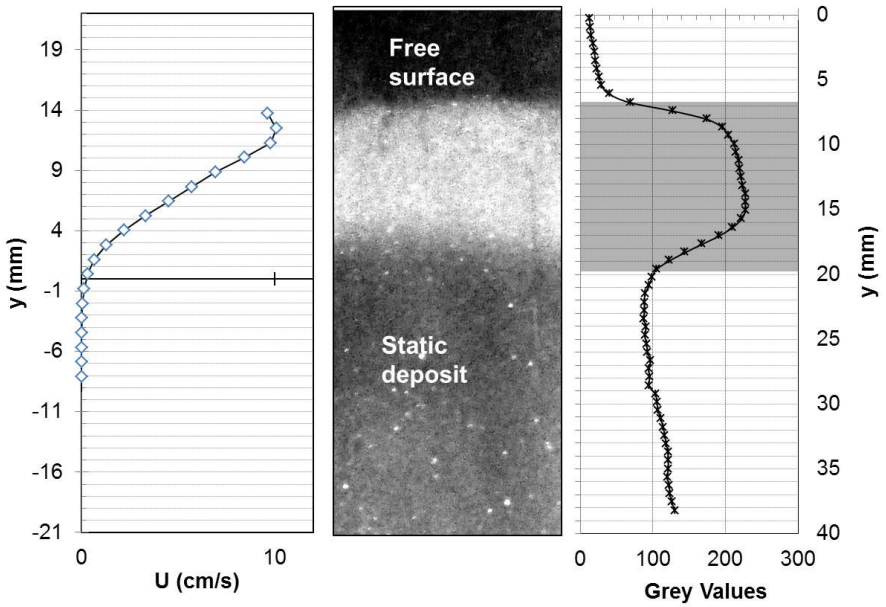


Figure 3.8: Example of measurements with the erosion method. At the left a grey-scale image of the blackened blade, at the right the histograms of the intensity values averaged on the image width. The extension of the peak corresponds to the flow-depth.

The technique was slightly modified to be adapted to the granular material used during the experiments. It consists in a thin metal blade, having a thick of 1 mm and a width of 2 cm, which is blackened by the smoke of a flame and then immersed in the granular flow for a given lapse of time (from 20 s to 40 s according to the flow-rate of the experiment).

The black coating is eroded by the particles flowing in the channel, while it remains almost untouched in the deposit where the grains are immobile.

Therefore, the height of the flow can be derived by estimating the extension of the bright part of the blade. It is done by computing the intensity histograms along the blade and measuring the distance between the line defining the surface of the flow, and the point at which the grey values stop decreasing (after having reached a peak value).

Picture 3.3 shows the identification procedure for the flow thickness and the comparison between the intensity histogram and the vertical velocity profile taken

near the side-walls.

During an experiments, three different measures of the thickness were done at different distance from the side-walls and in the same section of the flow. To avoid the blade deflection from the vertical, the metal edges were mounted on a plastic base at a given inclination and position, and then they were immersed in the flow, by placing the base on the side-walls. This device assures one to keep the blade in the same position during the measure.

Furthermore, to prevent the sooth to be consumed during the immersion phase, the blackened procedure was done after having painted the blade with a antistatic resin. The results are compared with the measurements made at the side-walls derived from the vertical velocity profiles. One should note that the method is quite intrusive, and the disturbing effects are larger decreasing the width of the channel.

## 3.4 Measurements of collisional properties of particles

The analysis regarded the collisions between the plastic material used in the experimental work and a small plate, representing the side-walls. The experimental apparatus was inspired from the work of Foerster *et al.* (1994) and Khakhar *et al.* (2001), but it was adapted and implemented to be used with our granular material.

### 3.4.1 Apparatus and procedure

The coefficients of restitution and friction for a particular collision may be calculated if the collision orientation and relative pre- and post-collision velocities are known. Conservation of angular momentum about the point of contact allows expression of the post-collision angular velocities in terms of particle masses, translational velocities and pre-collision spin. Thus, if two bodies collide without initial spin, the collision may be fully described by the knowledge of pre- and post-collision translational velocities, masses, and collision orientation.

Accurate measurements have been made of the rebound properties of particles impacting a plate of the same material of the side-walls. The study was performed for a large range of impact angles, from normal to near glancing incidence, and it was carried out by the means of the experimental system shown in figure 3.9. I is made up of:

1. A small-diameter nozzle that holds the particle at a known height from the plate at the beginning of the experiments. Its position can be modified along

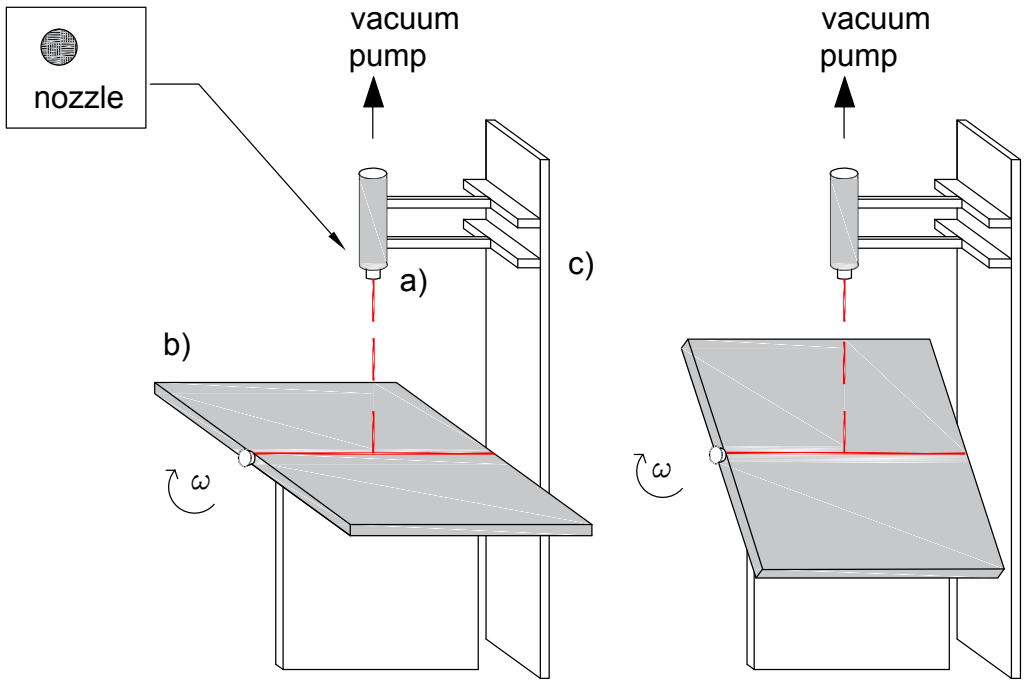


Figure 3.9: Apparatus to determine the collisional properties of the particles. It composes of a small-diameter nozzle connected with a vacuum pump, a plate that can be tilted, and a laser to align all the elements.

the vertical directions, while it remains perpendicular to the horizontal. The nozzle is connected with a vacuum pump and it is covered by a small piece of wove paper to prevent particles from being drawn inside the pump.

2. A plate having the same material and thickness of the flume side-walls. It is mounted on a pivot and can be turned at different angles with respect to the horizontal.

3. A small laser to align the mechanical components before each experiment, and to adjust the cameras to focus on the plane of the falling particles.

4. A digital camera (the fastcam x 1024 pci by Photron), used in these experiments with a resolution of 1024 x 512 frames, and a frame rate of 2000 to follow the particles during their impact

5. A lighting system, to detect precisely the spheres and a target to calibrate the image.

Initially the falling height was varied to study the dependence of the coefficient of restitution on the potential energy stored by the particles, keeping constant the angle

of the flat plate. In a second stage the spheres were released at the same height of 15 cm, and the tilting angle of the table was changed.

Table 3.1: Experiments performed to evaluate the collisional properties of particles

| n° tests | angle (°) | $h_{fall}$ cm |
|---|---|---|
| 19 | 0 | [4-12] |
| 5 | 0 | 15 |
| 5 | 30 | 15 |
| 5 | 40 | 15 |
| 5 | 45 | 15 |
| 5 | 50 | 15 |
| 5 | 60 | 15 |
| 5 | 70 | 15 |

### Procedure

During an experiment, a single particle was positioned at the nozzle centre thanks to a mirror, and it was held immobile by the vacuum pump. Then, the pump was turned off and the particle fell down impacting the plate. Therefore spheres started without a spin, having only the vertical component of the velocity, they reached the plate with a velocity that is function of the falling height and then they rebounded with a different velocity, which depends on the energy dissipated during the impact. The trajectory of the particles was registered by a fast camera, and processed by a home-made track code, which computes the normal and tangential components of the velocity to the plate (see figure 3.10).

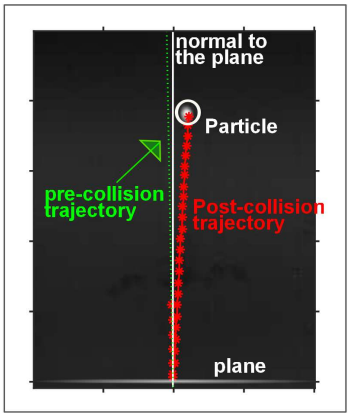


Figure 3.10: Particle tracking and reconstruction of its trajectory for a quasi-normal impact with the plate. In figure the pre and post-collisional trajectories, and the position of the particle detected at the $-i^{th}$ frame

The experiments performed can be summarised in the table 3.1

## 3.5 Direct measurements of stresses at the walls

This section shows the design of a device developed to obtain direct measurements of the shear stresses at the side-walls. During the research only a prototype could be developed, and only preliminary results could be achieved.

The sensor was designed to measure the wall shear stresses induced by the flow. It employs a floating element mounted flush with the wall and a mechanical cantilever system which bends in response to the shear stress applied to the sensor's surface. This bending is detected by two strain gauges attached to both sides of the cantilever, in correspondence to the joint. Figure 3.11 depicts how the sensor is mounted at the side-wall of the flume while figure 3.12 reports the rendering of the devise.

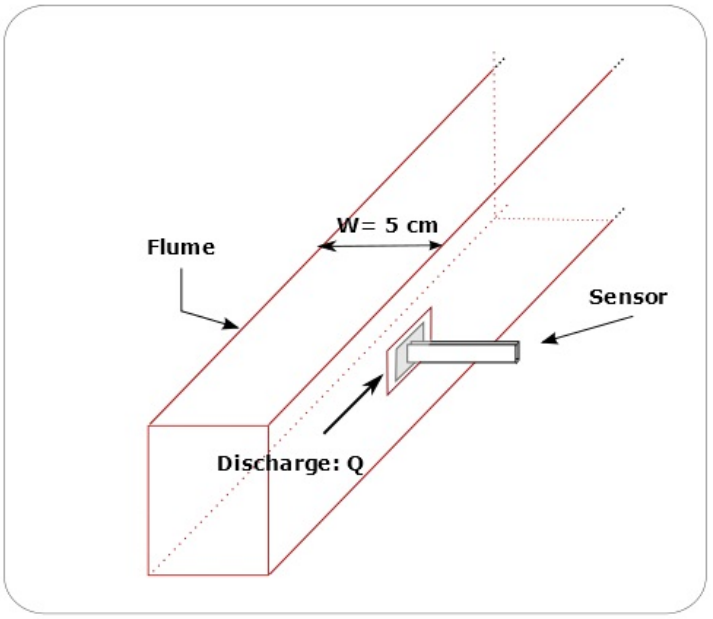


Figure 3.11: Position of the sensor at the wall flume and direction of the flowing material.

The system is inside a housing, which has a maximum gap with the floating element of 0.3 mm in order to avoid the intrusion of the granular material in the sensor. Since the flow height varies between a range of $0.6 - 1.5\,\text{mm}$ inside the channel, the active face mounted flush with the wall has a width of 6 mm. The sizes of the sensor are reported in the table table. 3.2.

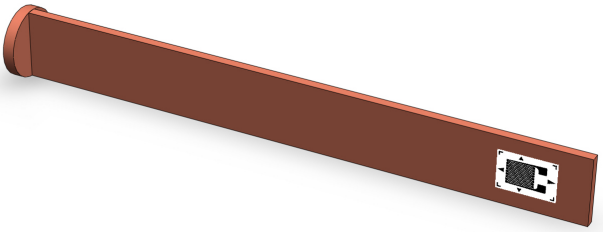

Figure 3.12: Rendering of the sensor. Three elements can be recognized: a disk, which represented the active element of the sensor, the cantilever, which can be bended, and the strain gauges attached at the joint of the sensor.

Table 3.2: Dimension of the developed sensor for the shear stress at the side-walls

| | |
|---|---|
| (active face)$W$[mm] | 10 |
| $h$ [mm] | 6 |
| $d$ [mm] | 1 |
| (cantilever)$L$ [mm] | 500 |
| $H$ [mm] | 6 |
| $s$ mm] | 2 |

**Project stresses**

In designing the device, shear stresses at the wall were assumed to be a fraction of the normal stresses. The following hypotheses were considered:

- In the worst case (maximum load) all the particles of the flowing depth touch the floating element at the same time. In a first approximation we can assume only a sliding mechanism, so that tangential stresses can be expressed through the Coulombian relationship: $\tau = \sigma \tan \phi$. Therefore they are almost half of the normal stresses.

- Actually particles also collide and roll along the walls, and they do not touch the floating element at the same time. So that tangential stresses are only a percentage of the Coulombian shear stresses.

Therefore, shear stresses can vary from a minimum value of $\frac{\sigma}{10}$ and a maximum value equal to the Coulombian contribution $\tau = \sigma \tan \phi$.

By making an analogy with the earth pressure we have the values listed in table 3.3.

| | **min** | **max** |
|---|---|---|
| $h$ (mm) | 6 | 30 |
| $\sigma_v$(Pa) | 58 | 288 |
| $\sigma_h$(Pa) | 40 | 202 |

Table 3.3: Project stresses for the devise designed to measure shear stresses

Having considered the following relationships:
For the vertical stress

$$\sigma_v = \gamma h \tag{3.13}$$

and for the lateral earth pressure:

$$\sigma_h = \sigma_v K \tag{3.14}$$

where $K$ is assumed equal to 0.7 (between the value of the active lateral pressure and the lateral pressure at rest) and $\tan\phi = \tan 25°$

The shear stresses value are:

- $\tau_{min} = 1/10\,\sigma_{min} = 4$ Pa
- $\tau_{max} = \tan\phi\,\sigma_{max} = 94$ Pa

**Stress analysis of the cantilever: preliminary considerations**

This section reports some considerations about the stresses on the cantilever.
In a first analysis the cantilever can be modelled as a jointed beam, which bends under the shear stress applied by the granular material through the floating element. The transversal force can be computed as:

$$T = \tau W H = 2.42 \cdot 10^{-4} \div 5.65 \cdot 10^{-3} N \tag{3.15}$$

Where $W$ and $H$ are the dimensions of the active face.

Considering a Young modulus of 120kN/mm$^2$ (having used copper), and a length of the cantilever of 5 cm, it is simple to derive the stresses due to the bending and the relative deformation along the axis of the beam for the minimum and maximum project forces respectively (See Tab 3.4).

| z | M | $\sigma$ | $\epsilon$ |
|---|---|---|---|
| mm | Nm | Pa | m/m |
| 50 | $10^{-5}$ | $9 \cdot 10^{3}$ | $8 \cdot 10^{-7}$ |
| 25 | $6 \cdot 10^{-6}$ | $5 \cdot 10^{3}$ | $4 \cdot 10^{-7}$ |

| z | M | $\sigma$ | $\epsilon$ |
|---|---|---|---|
| mm | Nm | Pa | m/m |
| 50 | $3 \cdot 10^{-4}$ | $2 \cdot 10^{5}$ | $2 \cdot 10^{-5}$ |
| 25 | $1 \cdot 10^{-4}$ | $1 \cdot 10^{5}$ | $9 \cdot 10^{-6}$ |

Table 3.4: Stresses and deformation for the minimum load configuration (left) and the maximum load configuration (right)

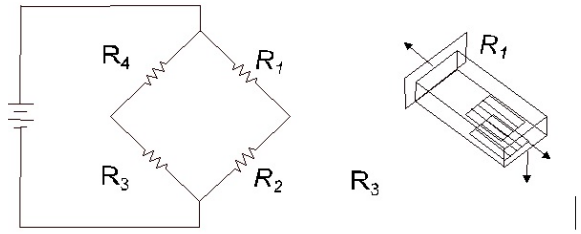


Figure 3.13: Circuit and positions of the strain gauge on the beam

**Electrical considerations**

Strains measurements are carried out by the means of strain-gauges applied at the end of the beam. In order to obtain accurate measurements, strain gages were used in a bridge configuration with a voltage excitation source of 5 V. The sensitivity of the bridge to strain are improved by using two gages active in a half-bridge configuration, in which one bridge is mounted in tension, while the other is mounted in compression (see Fig 3.13). In this case thevoltage at the end of the circuit can be expressed as:

$$\Delta V = \frac{\epsilon \cdot G \cdot V}{2} \tag{3.16}$$

where $\epsilon$ is deformation of the cantilever at the point where the strain gage is applied, $G$ is the Gage Factor of the strain gage while $V$ is the voltage excitation.

By considering a Gage Factor (G) of 2.1, we have:

- for the minimum value of deformation ($5.7 \cdot 10^{-7}$) the output voltage is equal to $0.0028mV$
- for the maximum value of deformation ($3.10 \cdot 10^{-6}$)the output voltage is equal to $0.016mV$

Better performances could be obtained by using a full bridge configuration, by placing two strain gauges orthogonal to each other onto both sides of the cantilever.

**Problems and accuracy**

Some aspects make the measurement of the shear stresses a tricky issue. First of all for the considered system, the exerted stresses are very low, and the devise should catch even lower variation of stresses along the flow-depth. To increase this sensitiveness, in a second version of the prototype the material was changed, and plastic was used. Therefore the device was printed by employing a 3D printer, having an additional guarantee on the perfect orthogonality between the cantilever and the floating element.

Then, the alignment of all the elements composing the measurement system is an important factor, determining the quality of the measure. The positioning of the devise is crucial during each run. To improve the result, measurements are taken simultaneously at both sides of the channel.

Finally, the most difficult task is the presence of powders that tend to intrude into the gap between the disk and its housing slot, getting stuck and distorting the measurements. Therefore, the system should be cleaned at every run and all the components should be aligned again to assure the repeatability of the measure.

## 3.6 Summary of the collected data

Table 3.6 and table 3.6 gather the main information of the experiments analysed in this work. The runs are divided in two sets, the first performed by using the entire width of the channel, the second carried out by partitioning the channel.

The histograms 3.6 show the number of experiments performed for each configuration (run at $W = 83d$ and $W < 83d$), having divided the flow-rates in 6 different classes of specific discharge $Q^*$ whose definition is given in the next chapter. For the two configurations some experiments were carried out by filming the flow from the top surface, while others were conducted imaging the experiment from the lateral walls.

Table 3.5: Experiments performed for a width of 5 cm.

| Run n | $\alpha$ [°] | $Q_s$[kg/s] | $Q*$ [−] | $H/d$ | Lateral | Surface | Analysis |
|---|---|---|---|---|---|---|---|
| treD_1 | 24.5 | 0.033 | 14.85 | 16.2 | x | | 3D Voronoï |
| treD_2 | 24.6 | 0.068 | 30.30 | 19.9 | x | | 3D Voronoï |
| treD_3 | 24.8 | 0.129 | 57.11 | 26.1 | x | | 3D Voronoï |
| treD_4 | 24.7 | 0.101 | 44.89 | 23.8 | x | | 3D Voronoï |
| treD_5 | 24.4 | 0.066 | 29.13 | 20.6 | x | | 3D Voronoï |
| treD_6 | 24.9 | 0.104 | 46.25 | 23.8 | x | | 3D Voronoï |
| treD_7 | 24.5 | 0.062 | 27.61 | 21.0 | x | | 3D Voronoï |
| treD_8 | 24.8 | 0.136 | 60.30 | 27.3 | x | | 3D Voronoï |
| treD_9 | 25.8 | 0.186 | 82.37 | 27.3 | x | | 3D Voronoï |
| treD_10 | 24.3 | 0.034 | 15.14 | 16.2 | | x | 3D Voronoï |
| Surf_1 | 24.1 | 0.041 | 18.09 | 19.2 | | x | 2D Voronoï |
| Surf_2 | 23.9 | 0.035 | 15.38 | 16.9 | | x | 2D Voronoï |
| Surf_3 | 23.9 | 0.035 | 15.38 | 16.9 | | x | 2D Voronoï |
| Surf_4 | 24.3 | 0.062 | 27.31 | 18.3 | | x | 2D Voronoï |
| Surf_5 | 24.3 | 0.062 | 27.37 | 18.3 | | x | 2D Voronoï |
| Surf_6 | 24.3 | 0.064 | 28.19 | 18.3 | | x | 2D Voronoï |
| Surf_7 | 24.7 | 0.086 | 38.34 | 21.7 | | x | 2D Voronoï |
| Surf_8 | 24.7 | 0.083 | 36.95 | 21.7 | | x | 2D Voronoï |
| Surf_9 | 24.7 | 0.083 | 36.95 | 21.7 | | x | 2D Voronoï |
| Fast_1 | 27.5 | 0.377 | 167.21 | 37.7 | x | x | 2D Voronoï |
| Fast_2 | 27.8 | 0.412 | 182.87 | 42.1 | x | x | 2D Voronoï |
| Fast_3 | 27.9 | 0.385 | 170.69 | 39.9 | x | x | 2D Voronoï |
| Fast_4 | 26.5 | 0.374 | 165.94 | 38.1 | x | x | 2D Voronoï |
| Fast_5 | 26.7 | 0.376 | 166.56 | 38.9 | x | | 2D Voronoï |
| Dam_1 | 24.5 | 0.066 | 29.12 | 22.4 | x | | 2D Voronoï |
| Dam_2 | 24.5 | 0.066 | 29.08 | 23.1 | x | | 2D Voronoï |
| Dam_3 | 24.5 | 0.068 | 29.97 | 23.0 | x | | 2D Voronoï |
| Dam_4 | 24.5 | 0.065 | 28.78 | 23.1 | x | | 2D Voronoï |
| Dam_5 | 24.7 | 0.039 | 17.43 | 18.0 | x | | 2D Voronoï |
| Dam_6 | 24.8 | 0.039 | 17.31 | 17.1 | x | | 2D Voronoï |
| Dam_7 | 24.5 | 0.038 | 16.68 | 18.9 | x | | 2D Voronoï |
| Dam_8 | 24.5 | 0.038 | 16.73 | 18.2 | x | | 2D Voronoï |
| Slow_1 | 24.0 | 0.031 | 13.77 | 21.4 | x | x | 2D Voronoï |
| Slow_2 | 24.9 | 0.088 | 39.16 | 24.9 | x | x | 2D Voronoï |
| Slow_3 | 24.4 | 0.014 | 6.38 | 11.8 | x | x | 2D Voronoï |
| Slow_5 | 23.9 | 0.039 | 17.40 | 20.2 | x | x | 2D Voronoï |
| Slow_6 | 24.1 | 0.025 | 11.14 | 19.1 | x | x | 2D Voronoï |
| Slow_8 | 23.9 | 0.014 | 6.38 | 10.0 | x | x | 2D Voronoï |
| Slow_10 | 23.6 | 0.015 | 6.68 | 10.3 | x | x | 2D Voronoï |
| Slow_12 | 23.7 | 0.006 | 2.82 | 10.0 | x | x | 2D Voronoï |
| Slow_14 | 23.4 | 0.005 | 2.15 | 9.8 | x | x | 2D Voronoï |
| Slow_15 | 23.7 | 0.013 | 5.81 | 12.4 | x | x | 2D Voronoï |

Table 3.6: Experiments performed for different widths

| Run n | W (cm) | $\alpha$ [°] | $Q_s$[kg/s] | $Q*$ [−] | $H/d$ | Lat. | Surf. | Analysis |
|---|---|---|---|---|---|---|---|---|
| W 1 | 1.5 | 27.07 | 0.01 | 8.66 | 17.90 | x | x | 2D Voronoï |
| W 2 | 1.5 | 27.46 | 0.01 | 12.43 | 21.84 | x | x | 2D Voronoï |
| W 3 | 1.5 | 27.60 | 0.01 | 13.43 | 21.97 | x | x | 2D Voronoï |
| W 4 | 1.5 | 27.89 | 0.02 | 31.27 | 25.97 | | x | 2D Voronoï |
| W 5 | 2 | 26.38 | 0.01 | 10.60 | 18.33 | | x | 2D Voronoï |
| W 6 | 2 | 26.66 | 0.02 | 18.34 | 22.17 | | x | 2D Voronoï |
| W 7 | 2 | 27.22 | 0.03 | 28.34 | 24.50 | x | x | 2D Voronoï |
| W 8 | 2.5 | 25.89 | 0.01 | 10.59 | 16.83 | | x | 2D Voronoï |
| W 9 | 2.5 | 25.90 | 0.01 | 11.02 | 17.17 | x | x | 2D Voronoï |
| W 10 | 2.5 | 26.00 | 0.02 | 13.88 | 18.83 | | x | 2D Voronoï |
| W 11 | 2.5 | 26.26 | 0.02 | 14.84 | 19.33 | x | x | 2D Voronoï |
| W 12 | 2.5 | 26.38 | 0.02 | 18.87 | 21.33 | x | x | 2D Voronoï |
| W 13 | 2.5 | 26.60 | 0.02 | 19.05 | 21.33 | | x | 2D Voronoï |
| W 14 | 2.5 | 26.60 | 0.03 | 28.59 | 23.83 | | x | 2D Voronoï |
| W 15 | 2.5 | 26.70 | 0.03 | 29.94 | 23.84 | x | x | 2D Voronoï |
| W 16 | 2.5 | 26.95 | 0.03 | 30.03 | 23.86 | | x | 2D Voronoï |
| W 17 | 2.5 | 26.55 | 0.03 | 30.20 | 23.86 | x | x | 2D Voronoï |
| W 18 | 3 | 25.60 | 0.02 | 15.68 | 18.08 | x | x | 2D Voronoï |
| W 19 | 3 | 26.20 | 0.04 | 28.28 | 21.50 | | x | 2D Voronoï |
| W 20 | 3 | 26.41 | 0.05 | 34.35 | 23.26 | x | x | 2D Voronoï |
| W 21 | 3.5 | 25.40 | 0.02 | 15.38 | 16.67 | | x | 2D Voronoï |
| W 22 | 3.5 | 25.71 | 0.03 | 21.24 | 19.17 | | x | 2D Voronoï |
| W 23 | 3.5 | 26.14 | 0.05 | 29.19 | 20.83 | | x | 2D Voronoï |
| W 24 | 3.5 | 26.53 | 0.06 | 35.73 | 22.50 | | x | 2D Voronoï |
| W 25 | 3.5 | 26.79 | 0.07 | 44.83 | 24.17 | | x | 2D Voronoï |

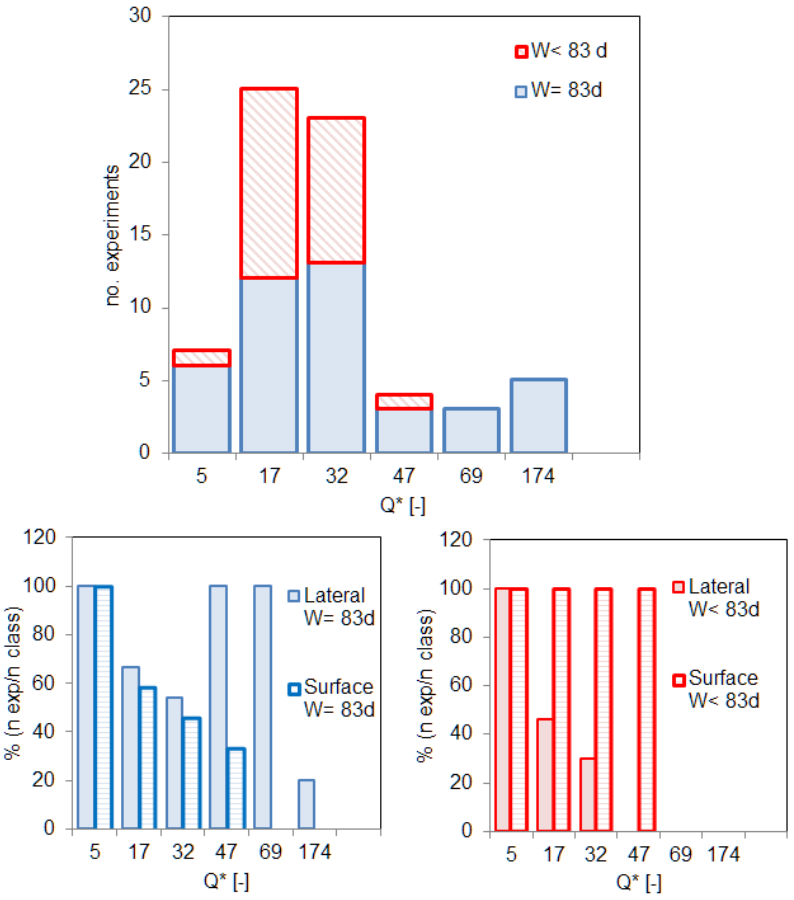


Figure 3.14: Overview of the data relative to the granular flows presented in the thesis. In the main plot the data are grouped according the width of the channel, while in the two sub-plots they are additionally divided in lateral and surface recordings

# Chapter 4

# Results

The experiments presented in the thesis refers to fully developed flows in a rectangular channel and over a loose bed.

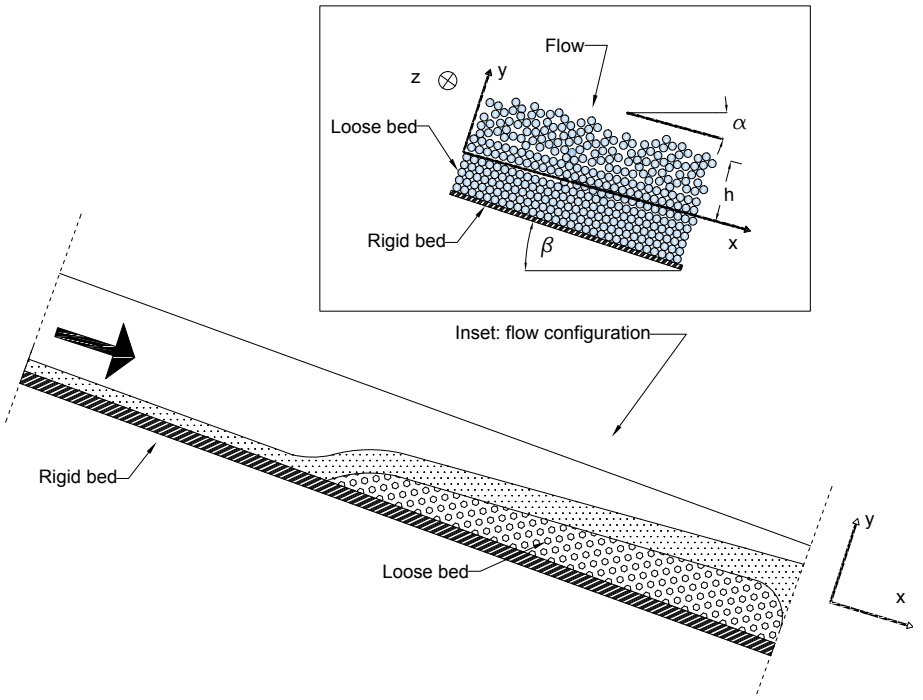


Figure 4.1: Sketch of the flow: the rigid bed corresponds to the channel base, while the loose bed corresponds to the static edge below the rolling grains. The $xyz$ system is based on the flow direction. $\beta$ is the tilting angle of the flume, while $\alpha$ is the slope of the free surface

The flow is three-dimensional, and the presence of a static deposit is induced by adopting two different configurations as explained later on.

In all the runs the flume was kept at an angle greater than the internal friction angle to obtain a part where the material flowed on a rigid rough base, and another part where it developed on a soft base.

The reference system considered in the analysis is represented in figure 4.1, where the $x$-axis is put along the direction of the motion, the $y$-axis along the flow depth, orthogonal to the surface, and the $z$-axis is considered along the spine-wise direction, normal to the side-walls. The flow depth $h$ is defined as the height of the flowing grains, and it is measured from the deposit to the free surface. In addition, the slope of the deposit is taken equal to the free surface slope, and it is measured with respect to the horizontal.

The measurements were made in correspondence of the sections where the flow conditions reach the uniformity, far from the outlet and inlet of the channel.

## 4.1 Definitions: averaged velocities and discharge

The flow characterization was done by detecting and following the particles passing through a fixed volume control, filmed by high speed cameras from the top-surface or lateral side walls as explained in the previous paragraph. In order to derive Eulerian quantities, averages should be performed, and some attention should be paid on the boundaries and extension of the control volume. It is due to the fact that, as in solid transport, granular flows are multiphase systems, in which particles occupy a sub-domain of the whole domain that is considered over finite periods of time.

From a theoretical point of view, considering Gray and Lee (1977), and as reported in a paper review by Nikora *et al.* (2013) there are different types of areal average. We will consider the superficial $\langle A\rangle_s$ and intrinsic spacial average $\langle A\rangle$ of a variable A, which are expressed as:

$$\langle A\rangle_s(x_i,t) = \frac{1}{V_0}\int_{V_0} A(x_i+\xi_i,t)\gamma(x_i+\xi_i,t), dV = \frac{1}{V_0}\int_{V_s} A(x_i+\xi_i,t), dV \qquad (4.1)$$

$$\langle A\rangle(x_i,t) = \frac{1}{V_s}\int_{V_0} A(x_i+\xi_i,t)\gamma(x_i+\xi_i,t), dV = \frac{1}{V_s}\int_{V_s} A(x_i+\xi_i,t), dV \qquad (4.2)$$

where $\gamma(x_i+\xi_i,t)$ is the"clipping function" that is equal to 1 in the solid phase and 0 otherwise. The volume $V_s$ occupied by the solid phase is given by the integral of the clipping function, computed over a generic control volume $V_0$:

$$V_s = \int_{V_0} \gamma(x_i+\xi_i,t), dV \qquad (4.3)$$

The angular brackets are a spacial average, and $x_i$ is the position at which the domain is centred ($\xi$ is the local coordinate system used for the integration). The main differences between the two averages is that the first one is obtained dividing

the value of A by the whole volume considered, while the second average is obtained by considering only the "net" volume occupied by the solids.

In the analysis of granular flows it is more convenient to define *areal* averages, in which the surfaces are the cross-sections of the control volumes. Ballio *et al.* (2014) defines the following quantities:

$$\{A\}_s(x_i,t) = \frac{1}{S_0}\int_{S_0} A(x_i+\xi_i,t)\gamma(x_i+\xi_i,t), dS = \frac{1}{S_0}\int_{S_s} A(x_i+\xi_i,t), dS \tag{4.4}$$

$$\{A\}(x_i,t) = \frac{1}{S_s}\int_{S_0} A(x_i+\xi_i,t)\gamma(x_i+\xi_i,t), dS = \frac{1}{S_s}\int_{S_s} A(x_i+\xi_i,t), dS \tag{4.5}$$

where the brackets $\{.\}$ denote areal average, $S_s$ is the portion occupied by the solid phase while $S_0$ is the total area as in the volumetric averages. Consequently, it is possible define an areal concentration as:

$$c_A = \frac{1}{S_0}\int_{S_0} \gamma(x_i,t) dS = \frac{S_s(t)}{S_0} \tag{4.6}$$

Therefore the sediment discharge over surface $S_0$ can be expressed:

$$Q = \int_{S_0} u\gamma = \int_{S_s} u = S_0\{u\}_s = S_0\{u\}c_A \tag{4.7}$$

Ballio *et al.* (2014) shows that the result is equivalent by performing the areal average only on the moving particles, since the immobile ones have zero-velocity.

The previous definition of the discharge corresponds to the definition of the volumetric transport rate per unit width defined as:

$$q_{bl} = u_{bl}\, c_{bl}\, \delta_{bl} \tag{4.8}$$

where $c_{bl}$ is the concentration and $\delta_{bl}$ is the thickness of the considered layer and $u_{bl}$ is the velocity. Ballio (2014) shows that the alternative definition of the solid discharge is based on volume-averaged quantities.

$$q_{bl} = N_{bl}\, u_{bl}\, w_{bl} \tag{4.9}$$

where $N$ is the number of particles, while $w$ the particle volume.

The previous concepts can be applied to the estimation of the velocity profiles and the solid discharge from the image acquisitions.

### 4.1.1 Mean velocity

Consider the images recorded from the flume side-walls, and the portion of the flow taken in the sequence of frames. The image window analysed in each frame represents the control volume, while the ensemble of particles detected corresponds to the volume of the solid phase. The cross sections defines the limits of the control volume.

The flow depth can be divided into not-overlapping horizontal layers of small thickness and a mean value of the velocity can be defined per each stripe.

The mean velocity in a bin is expressed as:

$$\langle u_k^{(n)} \rangle = \frac{\sum_i I_i^{(n)} u_i^n}{\sum_i I_i^{(n)}} \tag{4.10}$$

which corresponds to an intrinsic average: $\{u_k^{(n)}\}$ In this case $I_i^{(n)}$ is the indicator function equal to 1 if the particle (solid phase) falls in the $k$-th layer and equal to 0 otherwise, $u_i^n$ is the instantaneous particle velocity, and $\sum_i I_i^{(n)}$ is the total number of particles detected in a single frame in the $k$-th layer. Therefore, the indicator function selects only the particle that fall inside the computational area in which the averages are performed. Theoretically, in our case the superficial average can be expressed as a function of the intrinsic velocity through the concentration $c_s$, $\langle u_k^{(n)} \rangle_s = c_s \langle u_k^{(n)} \rangle$.

The same concepts can be applied also to evaluate the profile of the surface velocity.

In this section time-averaged quantities are considered for the vertical and transversal profiles. They are computed over a sequence of more than 1000 images corresponding to an effective duration of the flow of few seconds.

### 4.1.2 Depth-integrated quantities and bulk variables

Concerning the depth averaged velocity,we can give different definitions:

1. A first definition of the depth averaged velocity comes from the vertical profiles of the velocity (measured at the side walls) as:

$$\hat{U}_{lat} = \frac{\int_{\overline{h}} \langle u_k \rangle c dy}{\overline{h}\overline{c}} \tag{4.11}$$

   where the mean velocity is weighted with the concentration and is computed only over the portion occupied by the particles (without the voids). The mean

concentration is given by:

$$\overline{c} = \frac{\int_{\overline{h}} c dy}{\overline{h}} \tag{4.12}$$

where $\overline{h}$ is the mean thickness of the flow computed from the lateral recordings.

2. Another definition consider the whole depth of the flow, including the volume that is not occupied by the particles:

$$U_{lat} = \frac{\int_{\overline{h}} \langle u_k \rangle dy}{\overline{h}} \tag{4.13}$$

A bulk velocity can be also defined from the solid discharge, as

1.
$$\{\hat{U}_{lat}\} = \frac{Q_s}{W\overline{c}\overline{h}} = \frac{M_s}{\Delta t \rho_s W \overline{c}\overline{h}} \tag{4.14}$$

where $M_s$ is the solid mass measured at the outlet section of the channel ([kg])and $\rho_s$ is the solid density of the grains, $Q_s = M_s/\Delta t$ is the solid discharge ([kg/s]). In this case the ratio $M_s/\rho_s$ represents only the volume occupied by the particles, and the product $\overline{h}\overline{c}$ is the effective height occupied by the grains. Therefore the average correspond to an intrinsic average.

2. Another definition involves the total volume occupied by the granular flow:

$$\{U_{lat}\} = \frac{Q_s}{W\overline{h}} = \frac{M_s}{\Delta t \rho_s W \overline{h}} \tag{4.15}$$

**Scales**

In the following paragraphs we will use the mean velocity $\langle u_k^{(n)} \rangle$ (averaged also in time) to show the velocity profile for each run along the vertical and transversal direction.

In addition we will consider the average computed over the depth ($U_{lat}$) to compare the data adopting the Froude number scale.

Alternatively two other scales are taken into account in the presentation of the data:

- the diameter $d$, which is the mobility scale;
- the width $W$, which can be important for the lateral effect.

Using these scales we can define the non-dimensional discharge

$$Q^* = \frac{Q}{Wd\sqrt{dg}} \tag{4.16}$$

The non-dimensional velocity:

$$u^* = \frac{u}{\sqrt{dg}} \tag{4.17}$$

where $u$ is the mean value $\langle u_k^{(n)} \rangle$ and the non-dimensional flow-depth and width:

$$h^* = \frac{h}{d}; \qquad W^* = \frac{W}{d} \tag{4.18}$$

When the results are compared to the data from Jop *et al.* (2005), the dimensionless discharge is divided also by the mean concentration $\overline{c}$ considered equal to 0.6, using the same definition given by the authors in their work:

$$Q^* = \frac{M_s/\rho_s}{\Delta t \overline{c} W d \sqrt{gd}} \tag{4.19}$$

It is worth noting that the dimensionless discharge is equivalent to the Froude number multiplied by the submergence $h/d$:

$$Q^* = \frac{Q/\rho}{\nu W d \sqrt{gd}} = \frac{\overline{U} h W}{\phi W d \sqrt{gd}} \tag{4.20}$$

which is equal to

$$Q^* = \frac{F_r}{\phi} \left( \frac{h}{d} \right)^{3/2} \tag{4.21}$$

where $F_r = \overline{U}/\sqrt{gh}$

## 4.2 Uniformity and steadiness

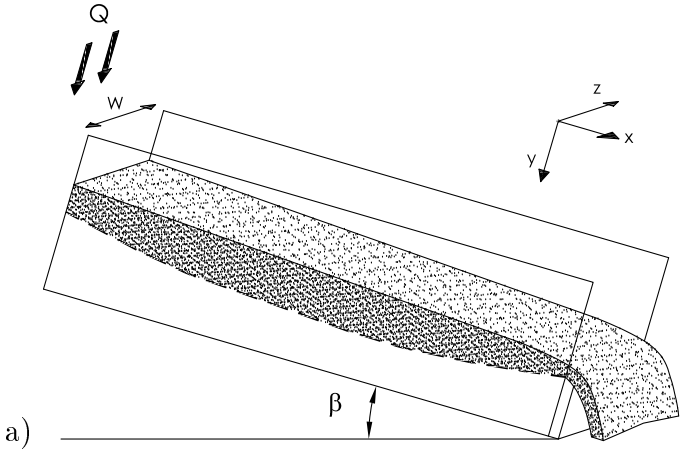


Figure 4.2: Rolling grains on a static edge in the case of a weir.

Two configurations were utilized and compared to obtain a steady flows over a soft bed. The first configuration was similar to that one commonly used in the

literature: it employed a simple weir placed at the end of the channel, which induces the formation of a static deposit inside the channel. This deposit is stabilized by the material flowing over it, and it extinguishes as the flow stops (see figure 4.2).

In the second configuration (see figure 4.3) the downstream conditions were changed and a gate with one or more slits was used to slow down the flow and make it to form a deposit.

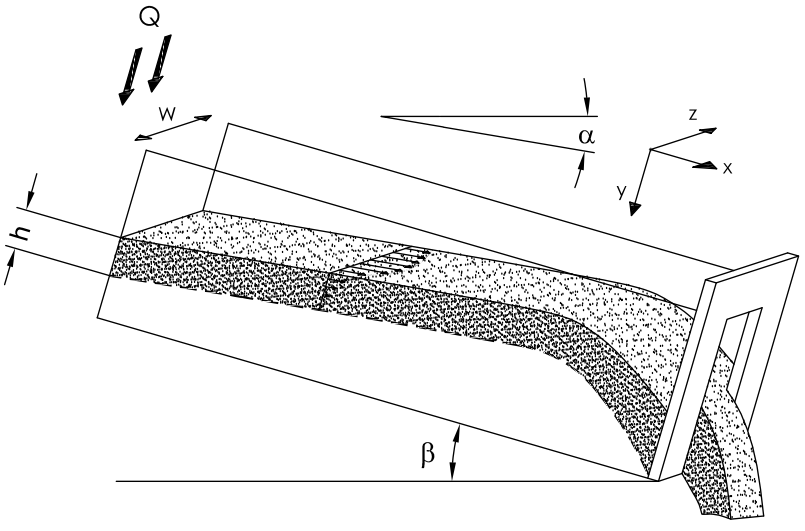


b)

Figure 4.3: Rolling grains on a static edge in the case of a slit gate and a tilting angle greater than the internal friction of the material.

The second option was studied to have a better control on the adaptation length of the flow, and to assure uniformity for a longer part of the channel.

For both of them, the section at which the material was released was at 2 m from the end section (long almost 3500 particle size). In the first case the height of the weir was kept constant and equal to 4 cm, while in the second case the apertures of the slit gate was changed according to the discharge.

The two settings were compared to understand the influence of the downstream conditions on the flow, starting from the observation that the uniformity can be achieved after a certain length (called adaptation length) as it happens for the sediments in a river, or for the back water effect in water (it is the distance at which this effect vanishes). After being poured into the channel, in fact, the particles need to travel a certain distance to adapt to the new conditions. Near the input section they own a certain velocity depending on the discharge and the height at which they have fallen down. Then they start to decelerate, until they reach a constant velocity that changes once again when they arrive near the outlet.

In the case of the weir, it is likely that the deposit develops along the flume as depicted in figure 4.2) and the material accelerates towards the weir. Putting a slit

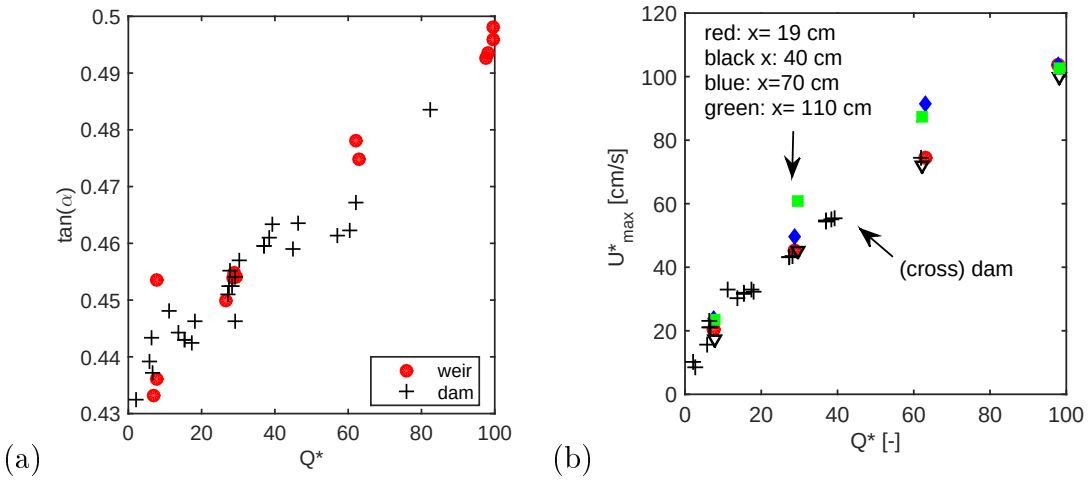


Figure 4.4: Comparison between the two configurations:(a) Variation of the free surface slope with the specific discharge, (b)and of the maximum values of the longitudinal surface velocity (b).

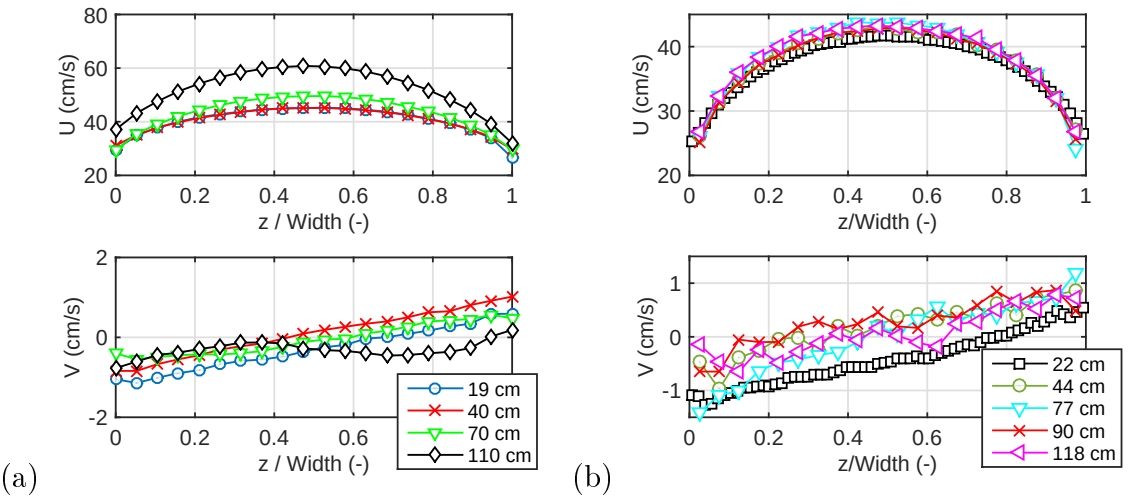


Figure 4.5: Velocity evolution along the channel in the case of the weir (a), and in the case of the slit gate (b). Symbols are relative to different sections at which the measurements were performed

gate at the end of the chute has been proven a better solution to obtain a longer region of uniformity.

Figure 4.4 shows a comparison between the two configurations. The free surface slope seems to be not affected by what happens at the outlet, while the velocity exhibits higher differences.

Figure 4.5 compares the surface velocity profiles obtained at increasing distance from the exit for the two configurations, and for the same discharge. In the case of the slit gate the longitudinal velocity does not change across the flume, except for the

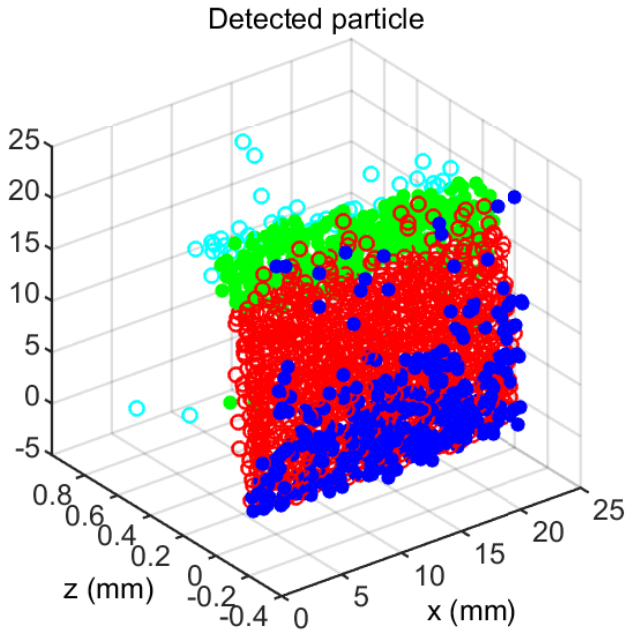


Figure 4.6: 3D coordinates of the detected particles in the volume control

part closer to the outlet, where the flow decelerates because of the contraction. For the weir, by contrast, the velocity tends to decrease towards the exit of the channel, reaching a steady condition only near the end. However here the flow is altered by the weir itself, and the disturbing effects on the velocity are not negligible.

It is worth noting that in the heap configuration studied by Taberlet *et al.* (2003), Taberlet *et al.* (2004), and Bi *et al.* (2005) particles are poured directly over the static hedge, and the flow-depth is often larger than the width of the channel itself. In our case, by contrast, the deposit starts forming for a deceleration of the flow, and the flowing height remains always lower than the width of the flume, being less influenced by the side-walls friction.

## 4.3 Flow field description

We start analysing a single experiment in which a stereoscopic recording has been carried out from the lateral side-walls.

The volume control is 22 mm x 15 mm x 1 mm, containing almost 2000 particles with a diameter of 0.6 mm. Figure 4.6 shows the centres of the detected particles in the experiment, subdivided in four different stripes of 0.13 mm along the transversal direction. The colours used to represent the particles change according the position, with darker colors used close to the side-walls, and brighter tones backward. In

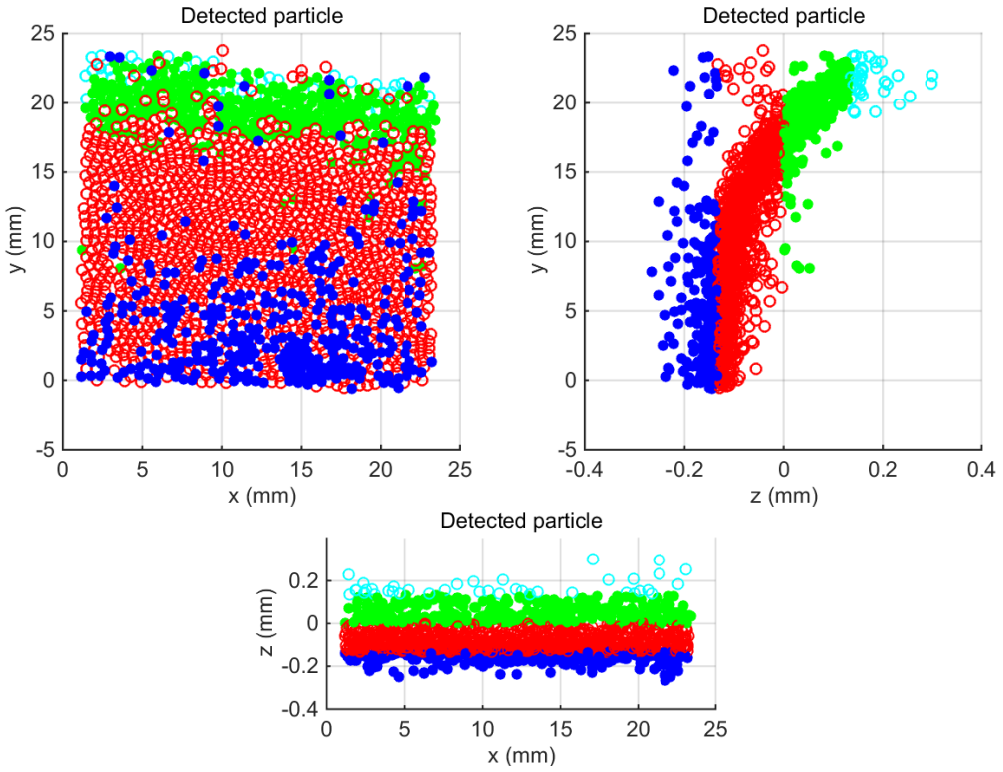


Figure 4.7: Orthographic projections of the detected particles in the control volume. Clockwise from the top: front view, side view and top view

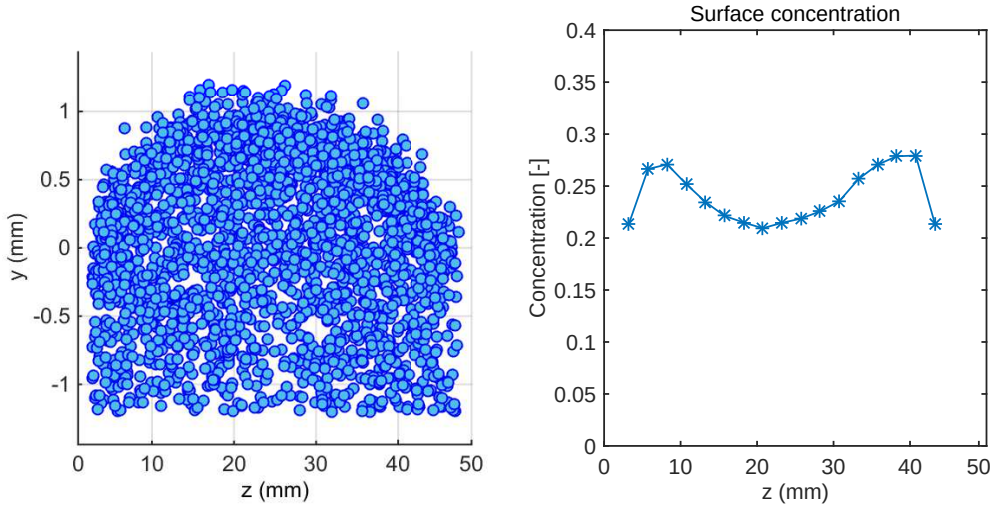


Figure 4.8: Particles detected recording the flow from the top surface. View of the plane $z - y$

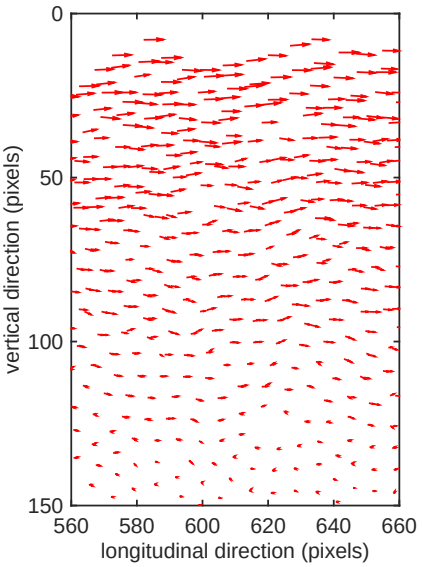


Figure 4.9: Trajectories for three successive instants. Coordinates are expressed in pixels

figure 4.7 the distribution of barycentre is represented more clearly in the three orthographic views, where the particles are projected on the front plane $x - y$, the lateral plane $y - z$ and the $x - z$ plane.

Since the flow is dense, over the most part of the depth observations are restricted to a region having a width comparable with the dimension of a single sphere. However, by approaching the free-surface, since the solid volume fraction at the wall decreases, the chance to get grains that are inside the flows increases.

Interesting aspects are highlighted by the recording obtained by the top-view. From picture 4.8 two important aspects are visible: (i) for dry granular flows lateral walls represent a very reflective boundaries that result in a reduction of the velocity near the side-wall, and in a slight curvature of the surface; (ii) the concentration changes in the transverse direction, reaching its lower value at the centreline where the flow is more rapid.

Analysing the trajectories in the $xz$ plane in figure 4.9, some considerations can be made on the particle motions. In the bulk particles are constrained to move in the available space, because they are confined below and above by the presence of the other grains. Momentum is constantly transmitted from a layer to another thanks to the repeating chattering of the particles, but only sometimes the velocity fluctuations are strong enough to push a particle to jump between strata. Once this occurs, a void is left and a new particle is free to move into the new available

space. Armanini *et al.* (2009) found out the same evidence for mixtures of solids and water, and Hill *et al.* (2003) observed the same behaviour in their rotating drums experiments. They pointed out that there is always a strong component of order, which results in a stratification parallel to the mean flow, superposed with a mild component of disorder (self-diffusion perpendicular to the mean flow).

For layers near the static deposit the motion tends to correspond to a slow rearrangement of particle position, and the vertical movement are strongly controlled by the formation of the voids, which become more rare.

The free surface is characterized by a higher agitation with respect to the below strata. However, compared to the experiments conducted in water or performed with heavier particles, our material shows a lower component of the motion in the direction perpendicular to the mean flow. Particles continuously jump one over each other, mixing together and travelling longer path with respect to the lower layers, but their ballistic trajectories are very flat.

Likely the motion at the surface is influenced by air intrusion, and in our case, since particles are light, this can affect their motion. It is worth noting that within the flow particles are too packed together to be influenced by the air.

## 4.4 Vertical profiles

The experiments analysed in the following paragraph are labelled as in table 3.6 and they are presented here divided in five groups according to their discharge: i) $Q^* = [0 - 10]$, ii) $Q^* = [10 - 25]$, iii) $Q^* = [25 - 40]$, iv) $Q^* = [40 - 70]$, v) $Q^* > 70]$. The profiles are measured from the lateral transparent side-walls, and therefore they could slightly changed in the $z$ direction, as we will illustrate in the next section.

The vertical coordinate is normalized with the flow-depth, which is defined as the height of the flow measured from the top free-surface to the point where the velocity profile is 0.1% of the mean value. The longitudinal velocity and the granular temperature are expressed respectively in cm/s and $cm^2/s^2$, while the other two parameters are dimension-less.

For experiments analysed through two-dimensional Voronoï method the concentration profiles are bounded by the random loose packing value close to the bottom, where they become too irregular. This is due to a limit of the two dimensional imaging technique, which overestimated the concentration where the grain configuration remains unchanged and the statistics are repeated over the same set of particles.

Vertical profiles are presented in figure 4.10, 4.11, 4.12, 4.13, 4.14, distinguished according their discharge. Velocity, concentration and granular temperature are all

continuously varying throughout the flow depth from the top free-surface down to the bottom.

The longitudinal velocity generally exhibits an initial downward concavity, while the last part has a different behaviour according to the flow-rate. In fact, it could be linear or have an inflection point, reaching the top layers with a different concavity. Some differences can been highlighted for increasing flow-rates: i) for very slow flows (Slow 14 and Slow 12 in figure 4.10) the linear part is a small fraction of the depth, and the velocity remains concave as it reaches the top layers; ii) at the opposite, for very rapid runs 4.14 there is an inflection point at half of the flow-height, with a reverse concavity, which seems to suggest a presence of "plug flow"; iii) in the intermediate cases the differences are not so sharp: the profiles could end with a linear part, or evolve towards the top with a downward concavity.

The concentration remains almost comparable to the random loose packing value for a large part of the flow-depth, and then it progressively decreases towards the surface, starting from almost half the depth. Slow and rapid runs (figure 4.10 and 4.14) are characterized also by a weak gradient throughout the height, involving more layers towards the bottom.

The granular temperature generally increases going to the top free-surface, and it follows the same curvature of the velocity. It gradually wanes near the bottom, where particles are trapped in their static configuration.

The Savage number ($I_s = \rho(\gamma d)^2/P$) is an indicator of the rheological stratification in the grain ensemble since it is defined as the ratio between a microscopic time scale $d/(P/\rho)$, which represents the time of rearrangements, and a macroscopic time scale linked to the mean deformation. Considering a threshold value at $I_s = 10^{-2}$, the vertical profiles show that the part of the flow-depth involved in a collisional-regime increases for increasing flow-rates.

## 4.5 Transversal profiles

Figure 4.15 and 4.16 display the variation of the longitudinal velocity and the granular temperature on the free surface in the direction normal to the side-walls. The experiments are grouped into different classes according to the flow-rates with the same division used for the lateral profiles: i) $Q^* = [0 - 10]$, ii) $Q^* = [10 - 25]$, iii) $Q^* = [25 - 40]$, iv) $Q^* = [40 - 70]$, v) $Q^* > 70]$. However here only four groups are presented.

The velocity exhibits a symmetric profile across the width (figure 4.15), reaching its maximum at the centreline, and its minimum at the side-walls. The trend is

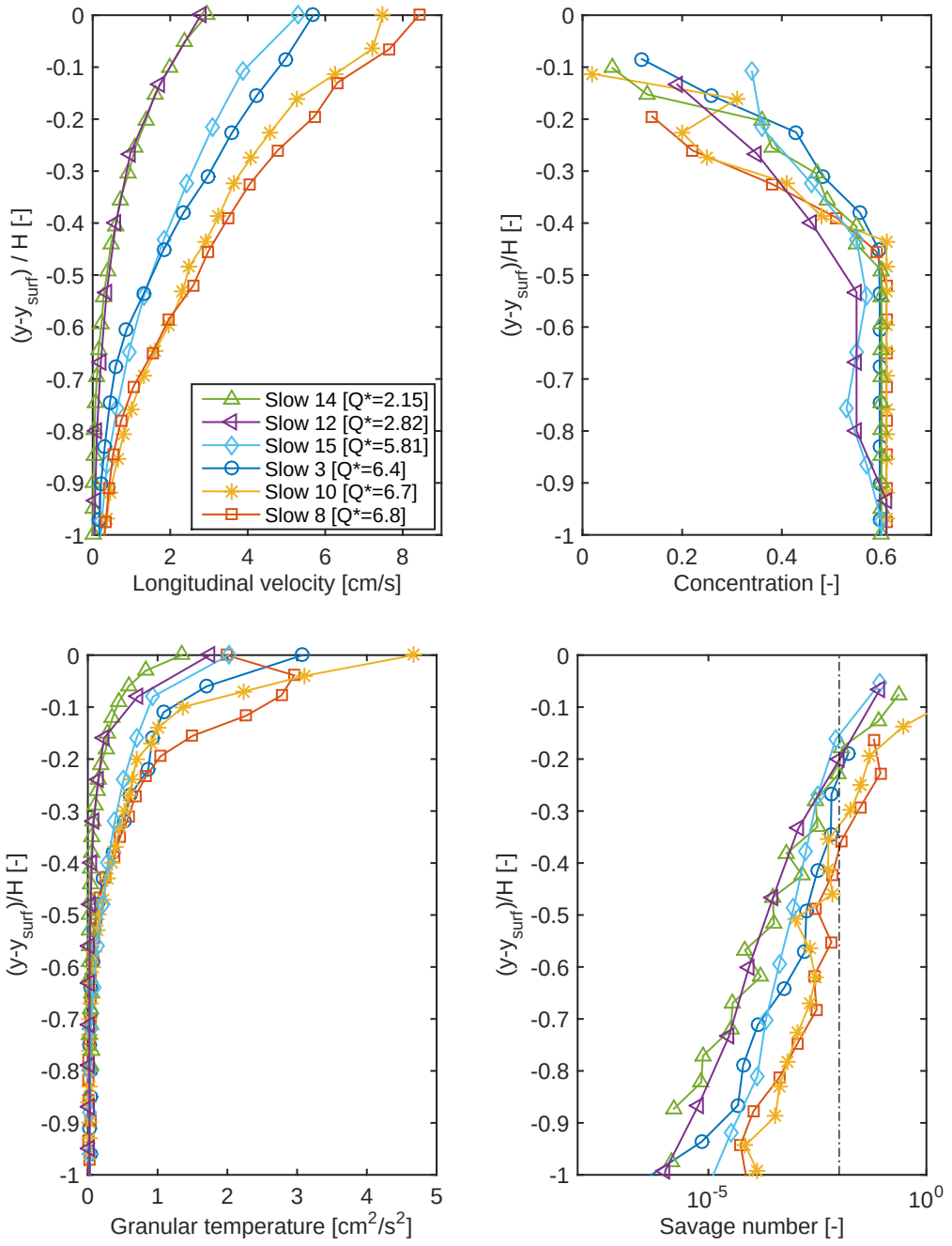


Figure 4.10: First group: $Q^* = [0 - 10]$

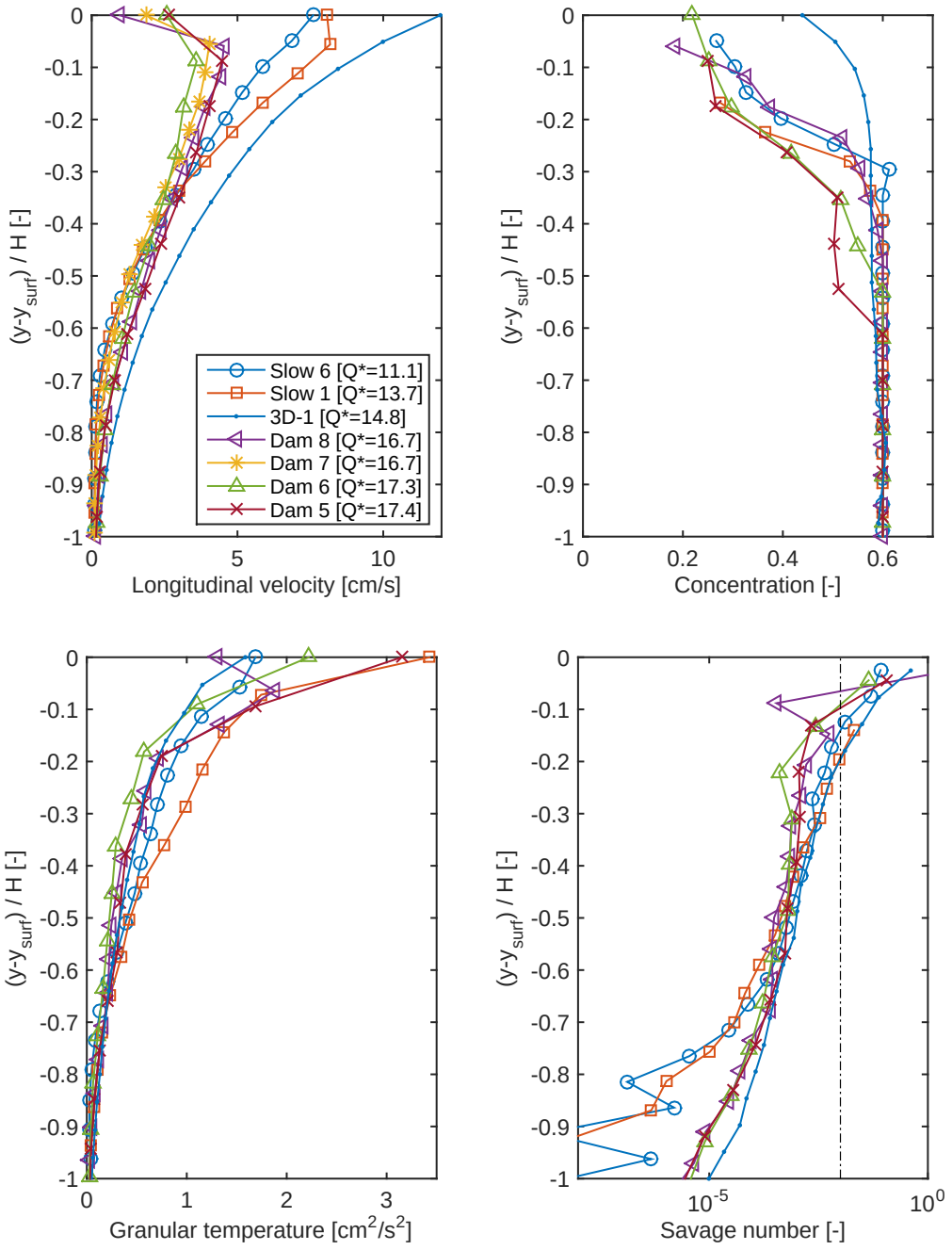


Figure 4.11: Second group: $Q^* = [10 - 25]$

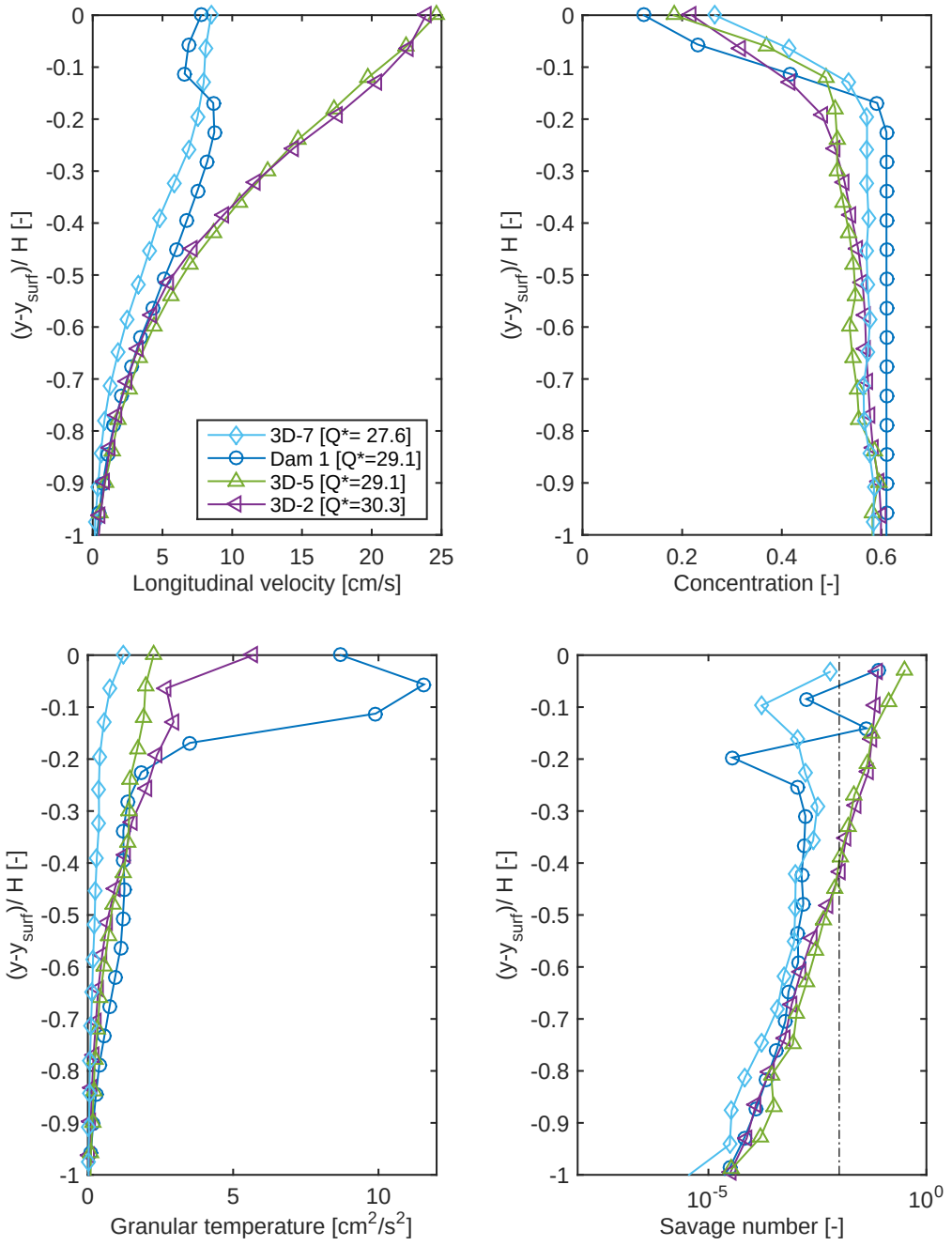


Figure 4.12: Third group: $Q^* = [25 - 40]$

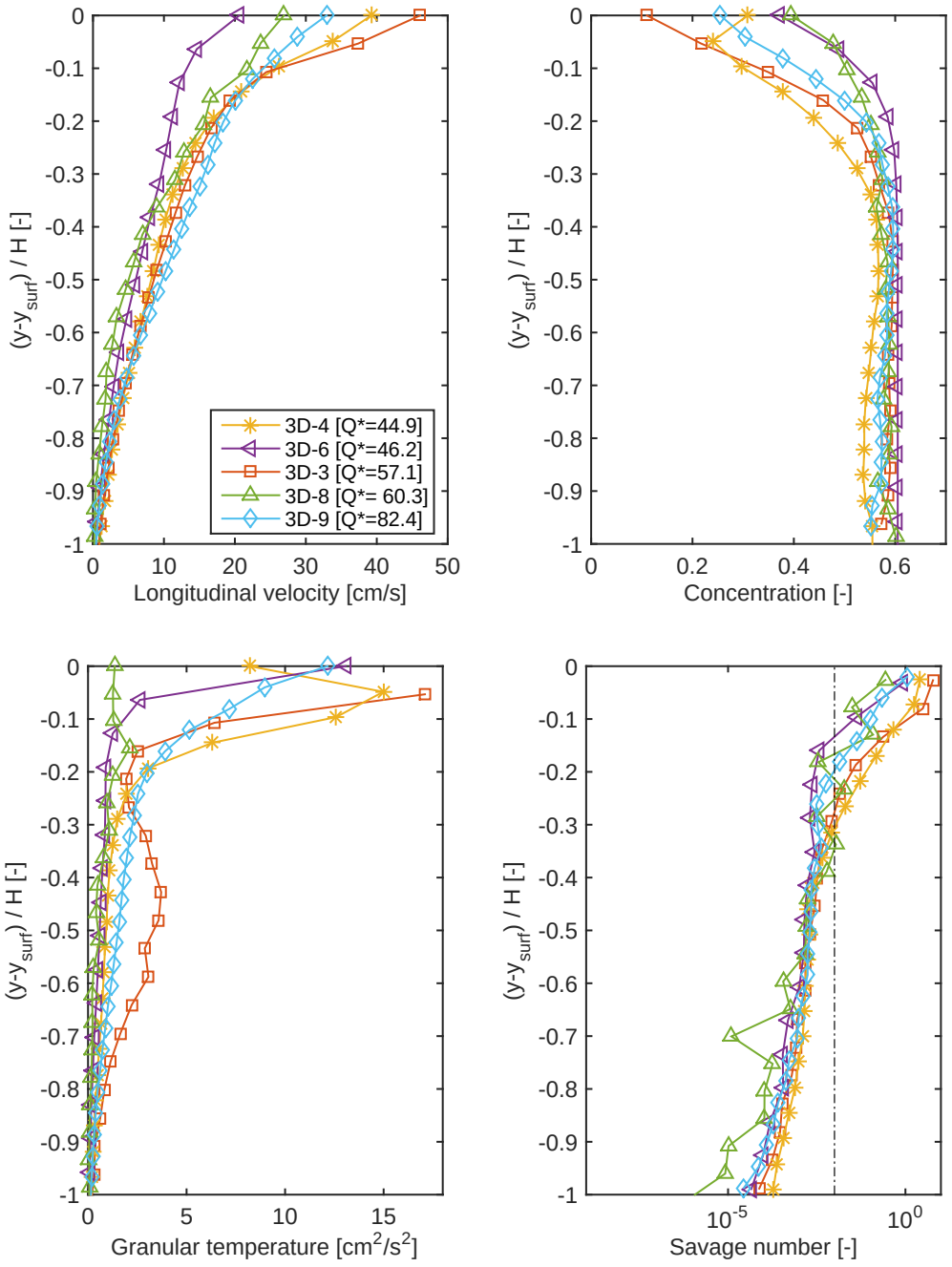


Figure 4.13: Fourth group: $Q^* = [40 - 70]$

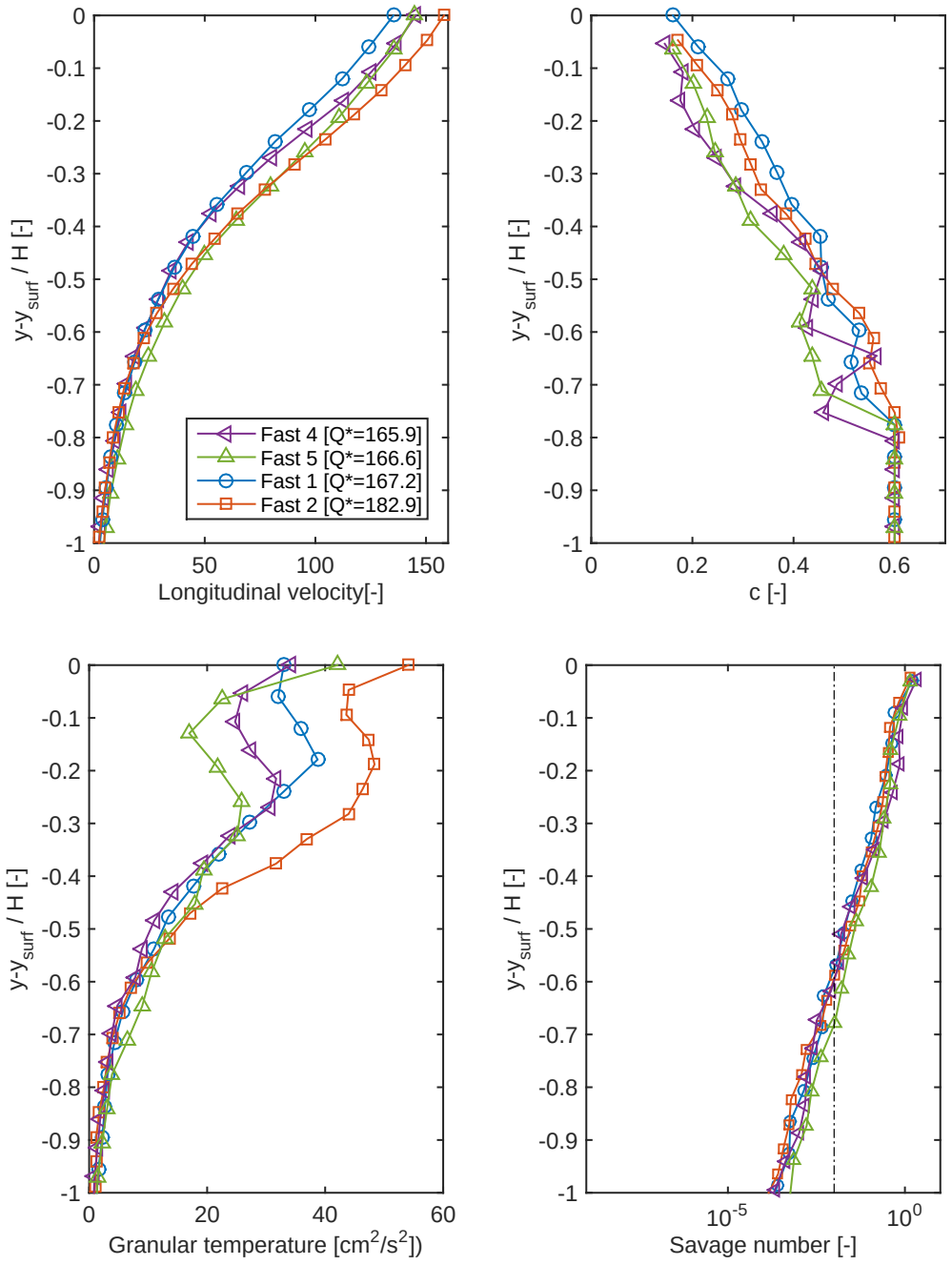


Figure 4.14: Fifth group: $Q^* > 70$]

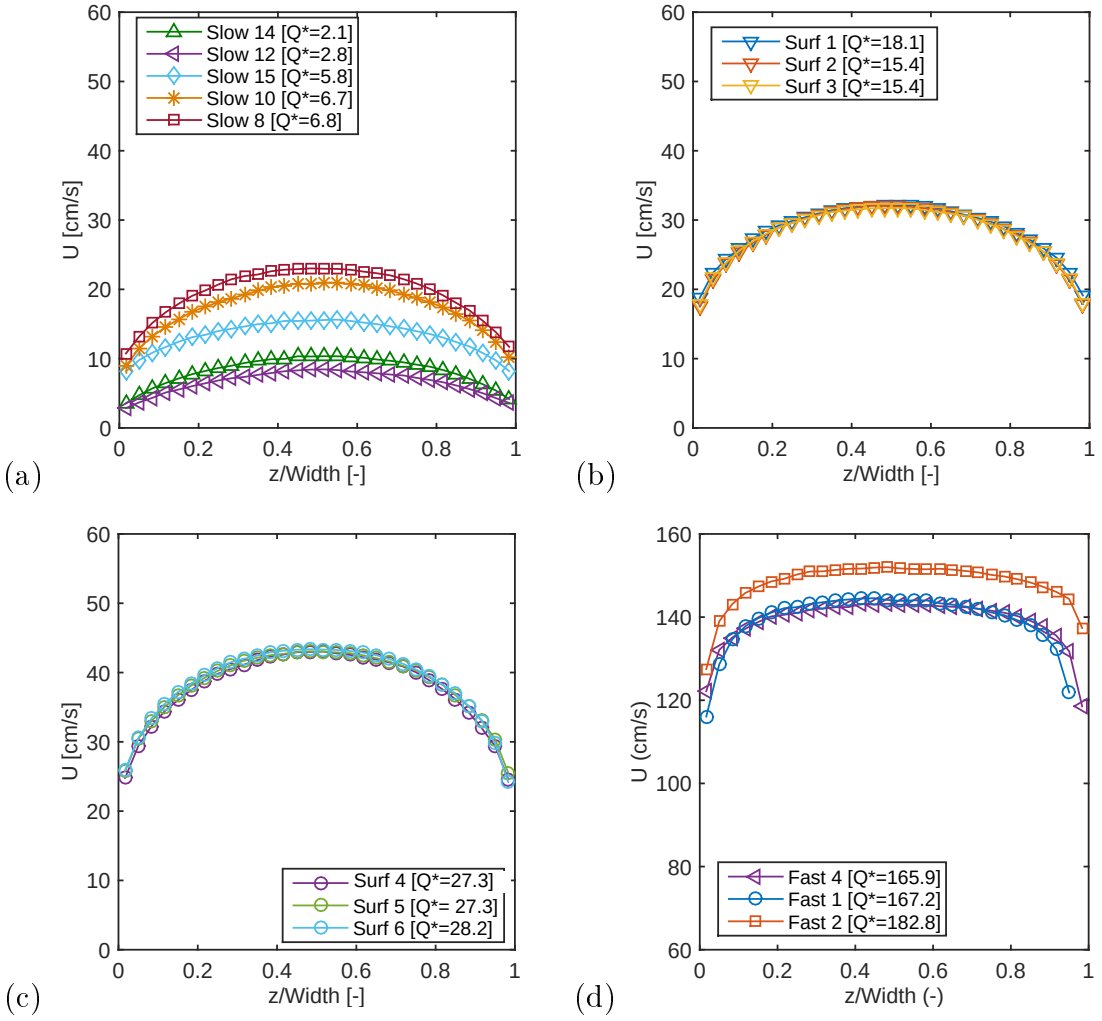


Figure 4.15: Transversal profiles of velocity for different discharges over the same width ($W = 83d$). From the top to the bottom, going clockwise the experiments are relative respectively to (a) $Q^* = [0 - 10]$, (b) $Q^* = [10 - 25]$, (c) $Q^* = [25 - 40]$ and (d) $Q^* > 70]$

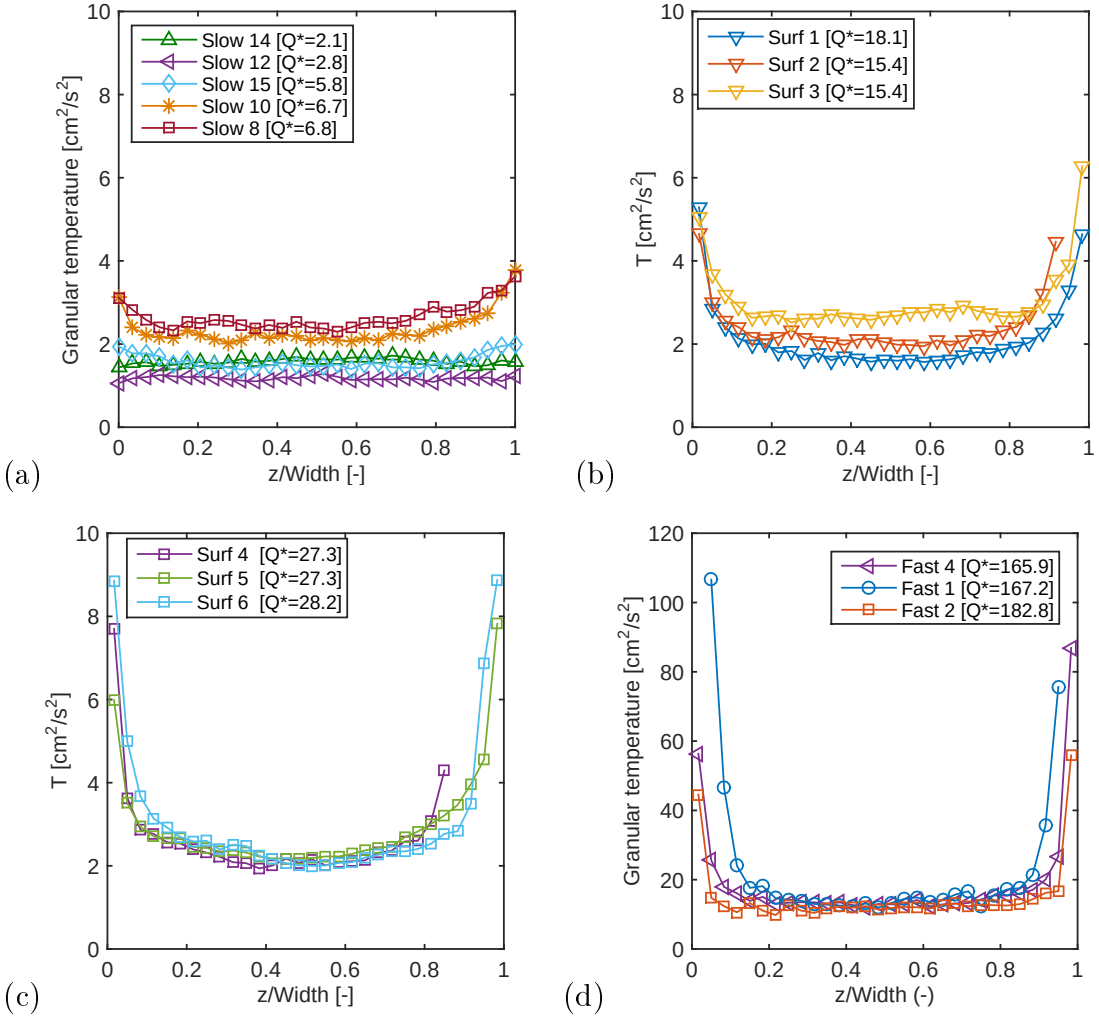


Figure 4.16: Transversal profiles of temperature for different discharges over the same width ($W = 83d$). From the top to the bottom, going clockwise the experiments are relative respectively to (a) $Q^* = [0 - 10]$, (b) $Q^* = [10 - 25]$, (c) $Q^* = [25 - 40]$ and (d) $Q^* > 70]$

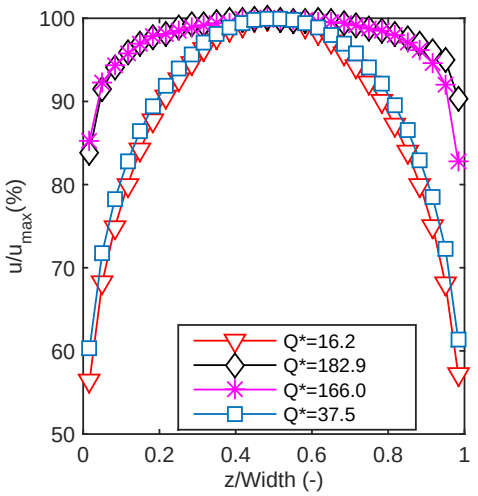


Figure 4.17: Transversal profiles of velocity at different discharge over the same width ($W = 83d$)

common for all the discharges analysed, and it remains unchanged also by varying the channel width as shown in the next paragraph.

Nevertheless, normalizing the velocity with its maximum value (figure 4.17) one can observe that for increasing flow-rates the profile becomes more uniform across the width as it happens for liquid flows in a turbulent regime. For example, while for a dimension-less discharge of $Q^* = 37$ [-] the lateral velocity is about the 40% of the maximum value, for a much higher flow-rate of $Q^* = 165$ [-] the difference among the two values reduces to a merely 20%.

The surface granular temperature is computed considering the fluctuating components parallel to the motion and orthogonal to the side-walls:

$$T = \frac{< u'^2 > + < w'^2 >}{2} \tag{4.22}$$

and it differs from the granular temperature estimated from the lateral walls, where the $w'$ component is not measured (for two-dimensional recording). As shown in figure 4.16 it is almost constant across the width, apart from the two bands near the lateral walls, where it increases. Here particles are continuously sheared between the walls, which have the effect of lowering particle velocity, and the "core" part of the flow, which, by contrast, tends to activate them. Therefore, grains are extremely agitated near the two lateral flat boundaries and they tend to fluctuate around the mean motion. It is interesting to note that for very slow flows the temperature remains almost constant also near the walls.

The concentration profile is not reported since its quantitative estimation is not

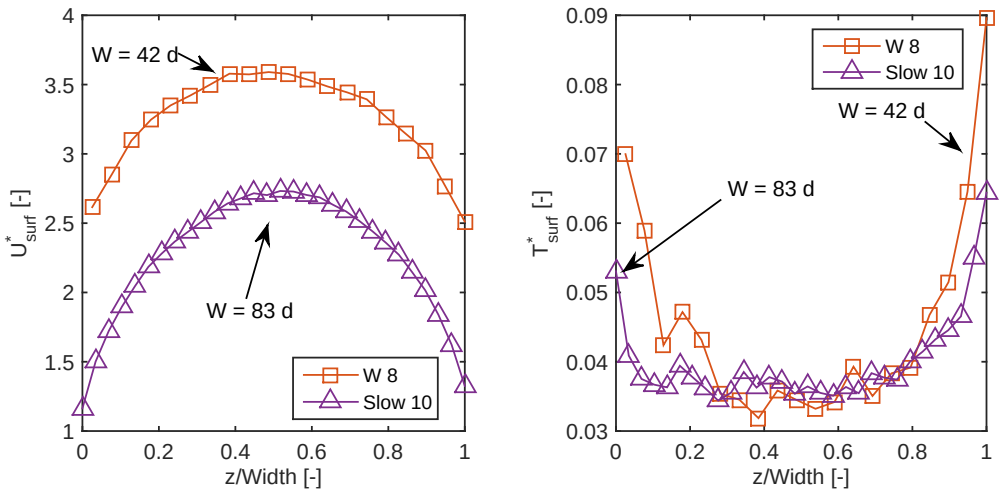


Figure 4.18: Experiments performed at a dimension-less discharge equal to $Q^* = 8.6$ with a mean deviation of 2. The profiles are relative to a width of 5 cm and 2.5 cm.

reliable on the free surface velocity for two-dimensional analyses. However as we can see from figure 4.8 the concentration reaches a minimum where the velocity has a maximum value, and it increases towards the side-walls. There it changes again, returning similar to the value assumed at the centreline. However, globally the concentration seems to remain constant.

## 4.6 Side-wall effect

Several experiments were performed by changing the width, in order to determine the influence of the lateral confinement on the flow dynamics. Five different widths were analysed and compared in addition to the width of 5 cm and they are summarised in table 4.6.

Due to some intrinsic limits of the set-up used in this analysis, the specific discharges investigated for the different widths are not strictly the same. Therefore to enhance the differences which arise by narrowing or enlarging the flume, we do not follow the same classification used in the previous paragraph. Here the comparison is made by considering experiments that were performed exactly at the same specific flow-rate (with a maximum deviation from the mean value of 2, referring to dimensionless values), to avoid other effects different from the lateral confinement.

Figure 4.18, 4.19 and 4.21 show the profiles of the longitudinal velocity and the granular temperature for three different discharges. The $z$ direction is normalized with respect to the channel width and spans from 0 to 1, while the granular temperature is normalize by the squared value of the reference velocity $\sqrt{gd}$. Considering the same specific discharge, the surface velocity usually increases by narrowing the

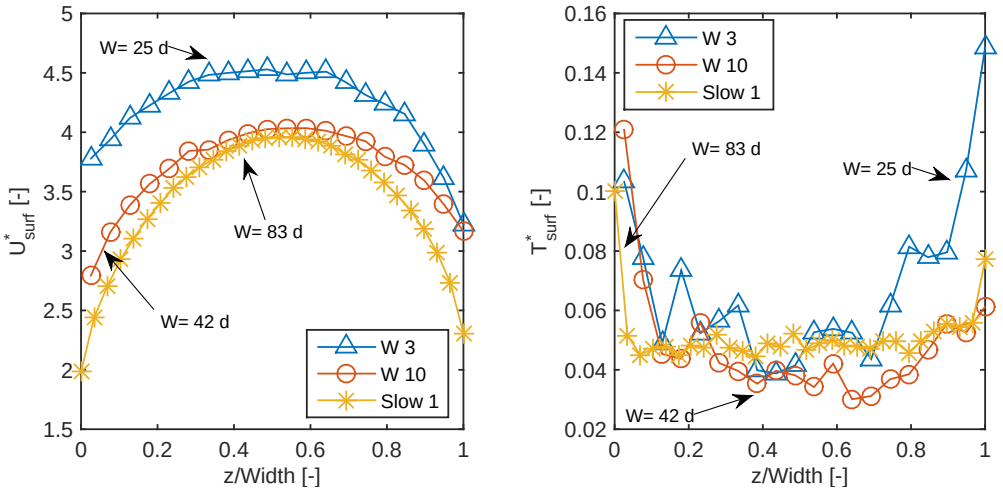


Figure 4.19: Experiments performed at a dimension-less discharge equal to $Q^* = 13.7$ with a mean deviation of 0.23. The profiles are relative to a width of 5 cm, 1.5 cm and 2.5 cm.

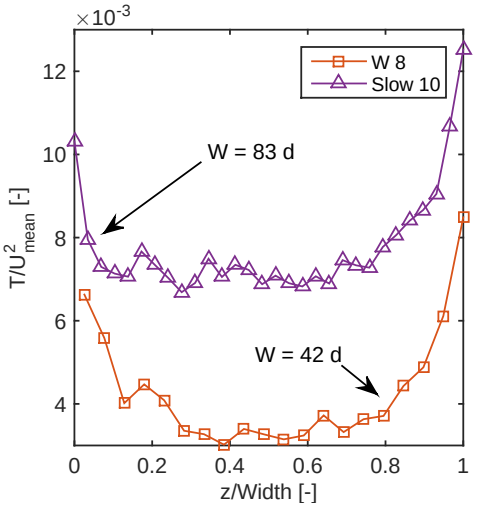


Figure 4.20: Experiments performed at a dimension-less discharge equal to $Q^* = 13.7$ with a mean deviation of 0.23. The profiles are relative to a width of 5 cm, 1.5 cm and 2.5 cm.

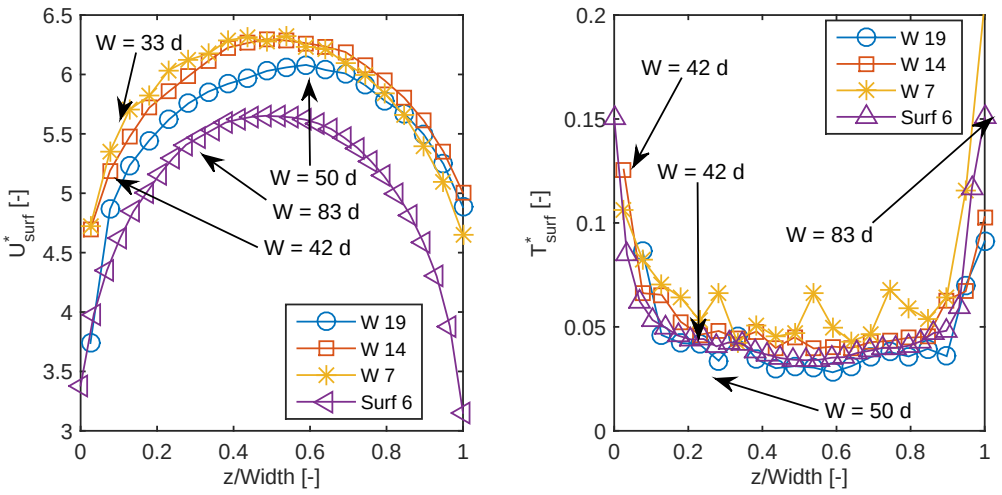


Figure 4.21: Experiments performed at a dimension-less discharge equal to $Q^* = 28.6$ with a mean deviation of 0.20. The profiles are relative to a width of 5 cm, 2.0 cm, 3.0 cm and 2.5 cm.

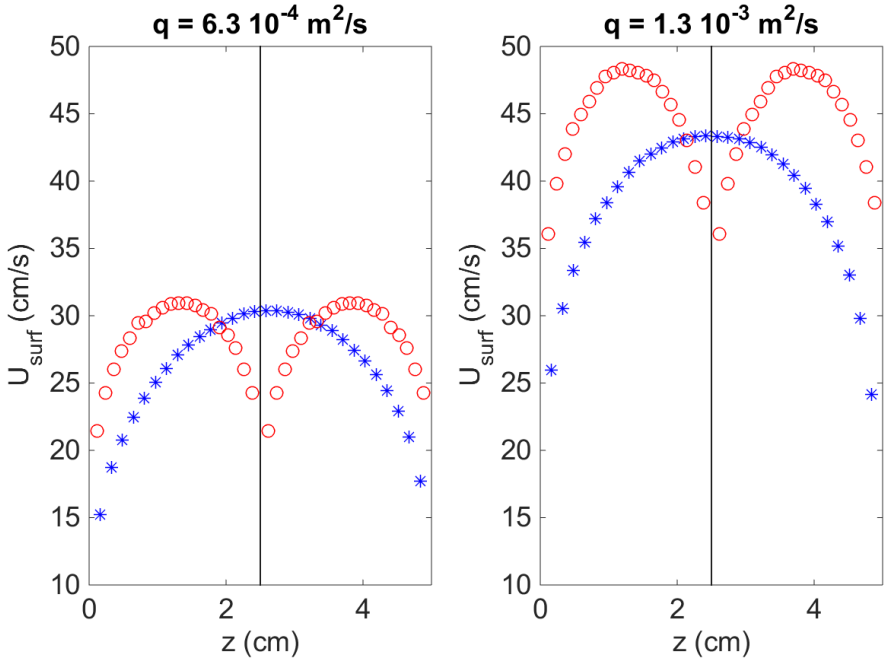


Figure 4.22: Experiments performed at the same discharge ($Q^* = 13.7$ and $Q^* = 28.2$), depicted together as they were performed simultaneously in the flume. The black line in the middle represents the symbolic separation of the channel in two equal parts large respectively 2.5 cm.

Table 4.1: Investigated widths.

| W [cm] | W [d] |
|---|---|
| 1.5 | 25 |
| 2.0 | 33 |
| 2.5 | 42 |
| 3.0 | 50 |
| 3.5 | 58 |

channel. This trend is always visible from very slow flows to rapid ones. and it is depicted more clearly in figure 4.22. If we consider a flume large 5 cm with a specific discharge of $Q^* = 13.7$, we get a velocity profile that in figure spans from left to right, with its maximum in the centre. If we divide the channel into two parts, large respectively 2.5 cm, but we consider the same specific flow-rate, we end up with two velocity profiles whose maximum are at the middle of the two partitions. The maximum value (and also the slip velocity at the side wall) for these narrow channels is higher than the maximum speed measured in the undivided flume.

As shown in figure 4.18, 4.19 and 4.21 the granular temperature tends to remain constant by varying the width of the channel, except for the part near the walls, where particles are very agitated. However, by normalizing the temperature with the squared value of the mean surface velocity (see figure 4.20) it seems that enlarging the channel the flow is characterized by higher values of the kinetic energy compared to the mean velocity of the flow.

The trend of the granular temperature could give some hints on the reasons why granular flows are faster for narrower channels. Higher values of the granular temperature result in stronger processes of dissipation and diffusion within the flow, which slow down as it loses its energy. Besides, the reduction of the velocity on the free surface causes an increase of the flow depth, due to the conservation of the mass. This process is combined with a larger diffusion of the kinetic energy downward, a and a consequent growth of the collisional part.

The trend is also visible from the lateral side-walls. Figure 4.23 shows the comparison between two experiments performed at the same specific discharge, but at different width (one the half of the other). As already mentioned, for wider channels the surface velocity is lower. However, the average flow-depth increases, as the temperature granular at the side-walls.

In this analysis two aspects have not yet been mentioned: the variation of the flow-depth along the width and the free-surface slope.

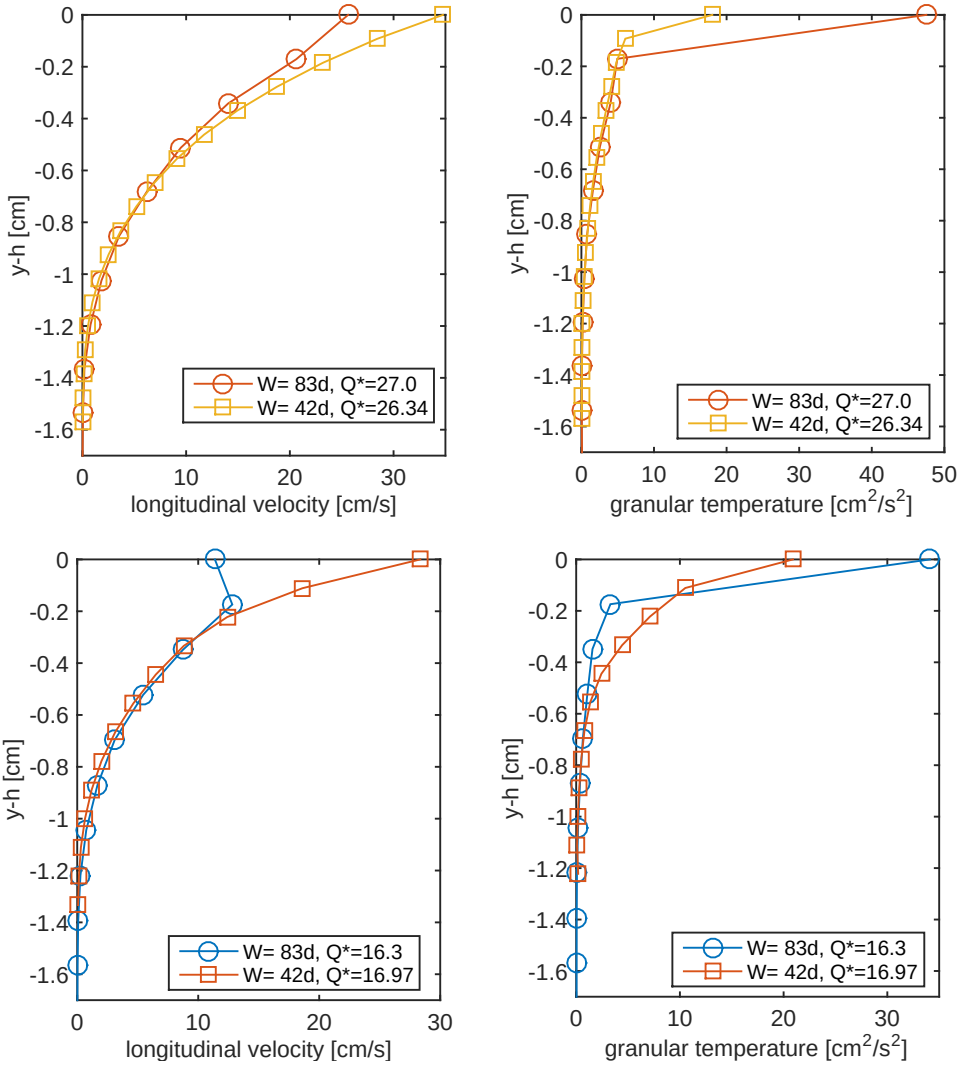


Figure 4.23: Experiments performed at the same discharge and filmed through the transparent side-walls. The top surface is placed at $y = 0\,\mathrm{cm}$. The differences between the flow-depths relative to the widths of $W = 83d$ and $W = 42d$ is always about $2 - 3$ particles.

### 4.6.1 Free surface slope

Figure 4.24 shows the variation of the free surface slope at increasing values of the dimensionless discharge, and for different channel widths.

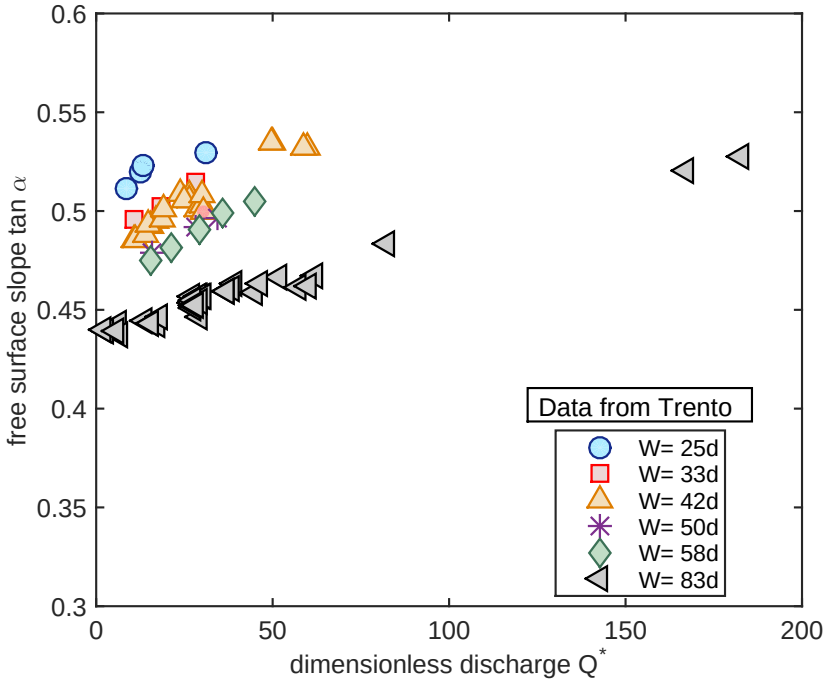


Figure 4.24: Tangent of the angle measured between the free surface slope and the horizontal as function of the dimensionless discharge $Q^* = Q/(W\, d\sqrt{dg})$. The different symbols refer to different widths, as indicated in the legend. All the data are collected in the flume developed in Trento.

As pointed out also by Jop *et al.* (2005), the free surface slope increases by narrowing the gap between the two lateral walls, reaching a steady value for higher discharge.

In our experiments the maximum flow-rate that could be obtained was limited by the volume of the hopper and by the extension of the channel, which was not enough long to allow for steady and uniform conditions in the case of very fast flows. However a general trend can be extrapolated looking at data relative to the largest width that was studied $W = 83d$.

The tendency of the free surface slope to increase with the flow-rate has been observed in previous studies (Rajchenbach (1990), Dury *et al.* (1998), Grasselli and Herrmann (1999), Lemieux and Durian (2000), Khakhar *et al.* (2001)), but its dependence on the width has been highlighted by the works of Taberlet *et al.* (2003),Jop *et al.* (2005).

In the hypothesis of a shear independent rheology, the free surface slope is an

indicator of the effective friction that acts in the studied system, and it is given by the ratio between the tangential and normal stresses $\mu = \tau/p$.

Therefore, as it can be observed in this plot, the friction depends on the flow-field and it is also affected by the lateral confinement. The latter factor becomes less and less important by enlarging the channel, as shown also by the data of Jop *et al.* (2005) who performed several measures on a wide range of widths. The effect of the side walls can be summarised in the following points:

1. Decreasing the width the flow becomes "*sliding*" (and frictional). In fact, narrower is the channel higher is the influence of the lateral walls. However, as shown in figure 4.20 the granular temperature increases locally near the side-walls due to the rebounds of the particles. This means that the dissipation is lower in this part of the flow, and the free surface slope increases.

2. Conversely, for wider channels the lateral boundaries play a minor role, while the loose bed has a relatively higher weight. As a consequence the free surface slope decreases.

3. Therefore, for increasing widths $W \to \infty$ the flow becomes more and more collisional as the walls have less importance (e.g. shear dependent). The flow depth increases, and, for continuity, the velocity reduces for an increasing process of diffusion downward.

In section 5 this elements are interpreted according an hydraulic approach, pointing out how they are deeply connected to each other.

## 4.7 Flow-depth measurements

For some experiments the flow-depth was determined through the erosion method described in section 3.3, varying the flow-rate and the width of the flume. These measures were compared with the thickness estimated from the vertical profiles recorded at the side-wall, evaluating the accuracy and the differences between the two methods.

The aim of the analysis was to quantify the variation of the flow thickness in the transverse direction, starting from the assumption that it evolves as the velocity profile does in the flow interior. As pointed out by different experimental works (Armanini *et al.* (2005), Jop *et al.* (2005)), the flow field has a strong three dimensional character, and the velocity profile can be fitted by an hypothetical paraboloid surface. So that one might expect that the depth tends to increase towards the

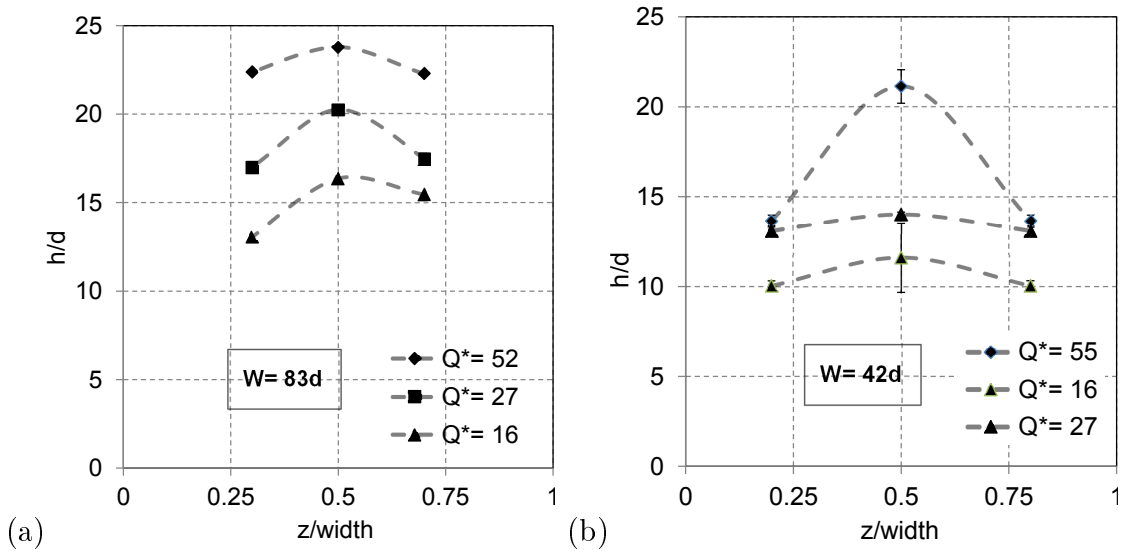


Figure 4.25: Flow variation in the transversal direction for two different widths. (a) $W = 83d$ and (b)$W = 42d$

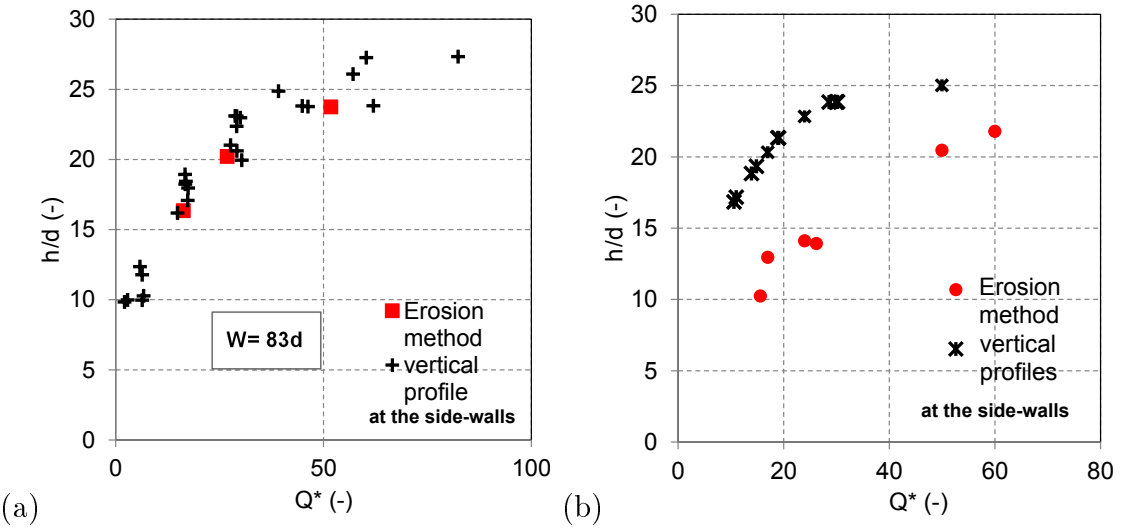


Figure 4.26: Comparison between the measurements performed with the erosion method (red spot) and the estimates done by the imaging techniques at the side-walls. (a) $W = 83d$, (b) $W = 42d$

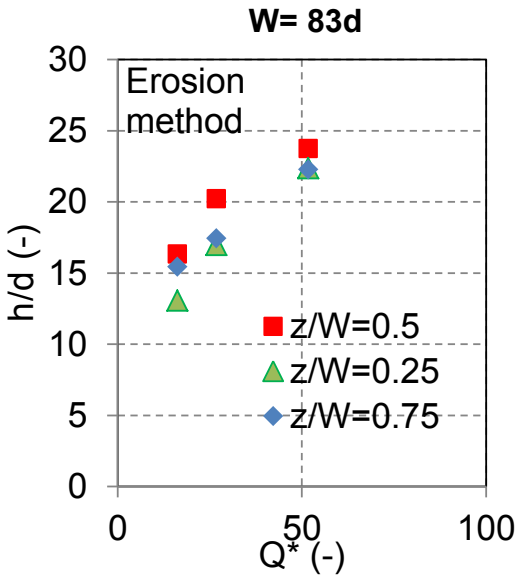


Figure 4.27: Erosion method: results for a width of $W = 83d$. Comparison between the measures carried out at the centreline and at the side walls for different specific discharge.

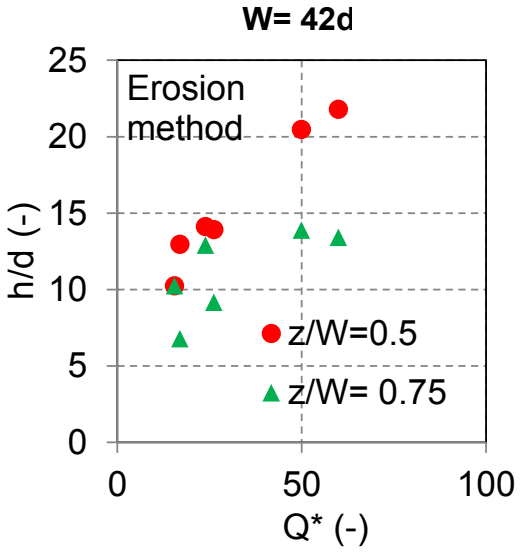


Figure 4.28: Erosion method: results for a width of $W = 42d$. Comparison between the measures carried out at the centreline and at the side walls for different specific discharge.

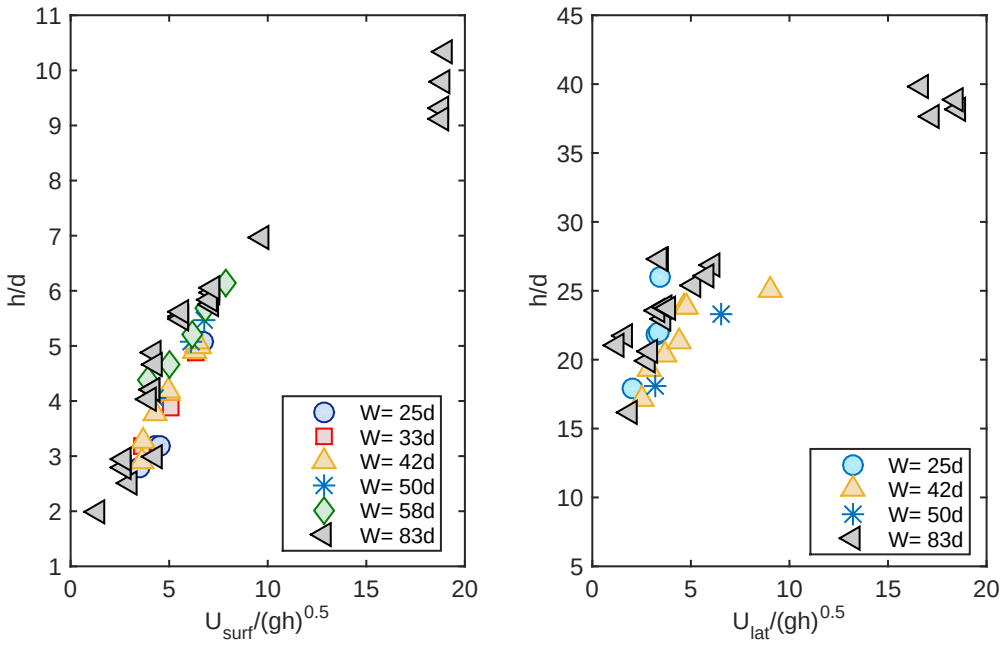


Figure 4.29: Flow-depth and velocity. (a) the flow-depth is computed by the ratio between the discharge and the surface velocity, (b) the flow-depth is estimated from the vertical profile of the velocity filmed at the side-walls.

centreline, remaining lower at the side-walls, following the same trend of the longitudinal velocity. Jop *et al.* (2005) found out that for a width of $W = 142\,d$ the difference between the height in the two points is of the order of about 30% considering a discharge of $Q^* = 16.5$, while Armanini *et al.* (2005) observed that a flow could have a thickness up to 6 cm at the lateral walls, still presenting moving grains at the centreline.

The erosion method was tested on two different widths of $W = 83d$ and $W = 42d$, and the measures were performed at three consecutive points of the same section of the flow, respectively one at the centreline, and two on 1/4 and 3/4 of the total width. Together with these measures, for each discharge, lateral recordings were performed to make a comparison between the two techniques.

Some considerations can be done by comparing the results:

1. The erosion method allows to measure the flow-depth even far from the side-walls, where imaging techniques cannot be applied, but it does not give a measure of the velocity. Figure 4.25 shows the crosswise variation of the height both for a width of $W = 83d$ and $W = 42d$, and for three different flow-rates. The difference between the values measured at the centreline and at the side-walls is always of the order of few particles (with a mean value of 3), which is much lower than the reduction measured by Jop *et al.* (2005). The main

discrepancy is registered by the highest flow-rate $Q^* = 55$ used for a channel large $W = 42d$.

2. On the other hand, pushing a blade inside the flow modifies locally the velocity field and consequently the depth that should be measured. This effect is more important for narrower channel. The presence of the blade represents a further reduction of the available width, and the flow accelerates locally lowering near the blade. Therefore, especially for thin channels, the technique could underestimate the depth.

3. The previous considerations are confirmed by figure 4.26, where the measures done through the erosion method at the centreline are compared to the depth estimated by the lateral side wall from the vertical profile of velocity. The latter values should be lower than the former ones, because they are taken at the lateral walls. However it does not happen, especially for the narrowest channel, and the flow-depth seems to be underestimated by the erosion method. It could be to the fact that: i) the blade disturbs the flow as it has been explained previously; ii) the blacking coating is removed only by the fastest particles, because the grains that are just above the static bed do not own enough energy to erode the sooth; iii) finally, the measured coming from the vertical profiles are done considering the portion of the flow that is between the top surface and the layers where the velocity is about 0.1% of the mean value. So that they also include slow particles.

Considering these aspects, we decided to relay on the flow-depth measured by the vertical profiles for our experiments, still keeping in mind that the flow-depth is deeper at the centreline.

## 4.8 Comparison with literature data

In this section the experimental results are compared with the literature, considering more precisely the work of Jop *et al.* (2005) and Taberlet *et al.* (2003), who studied the flow over an heap, and the effect of the side-walls on the flow-dynamics.

By comparing the data with the experiments of Jop *et al.* (2005), the scale of the mobility is adopted.

1. Figure 4.30(a) shows that the maximum values of the surface velocity computed in Trento are in agreement with the data of Jop for the lower flow-rates,

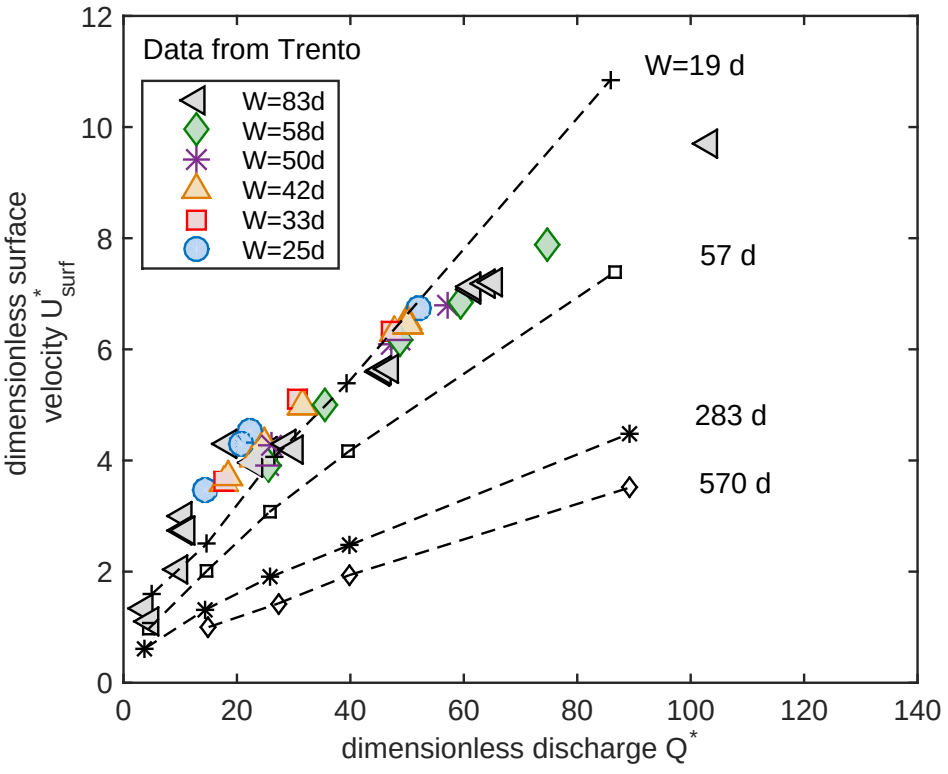


(a)

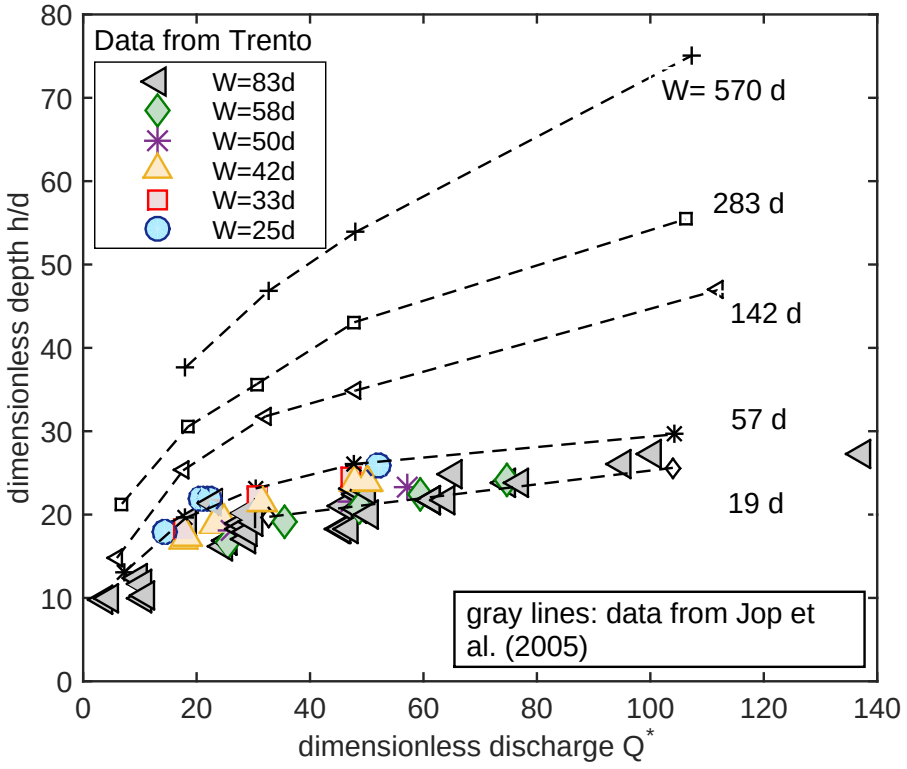


(b)

Figure 4.30: Comparison with the experiments performed by Jop (grey lines).

Table 4.2: Mechanical properties of the set-up used by Jop *et al.* (2005) and Taberlet *et al.* (2003), compared with the set-up developed in Trento. Properties characterizing binary collisions for the small plastic spheres used in Trento are derived from literature, while the parameters describing the impact between the wall and a sphere have been measured as described in the section 4.9.

| **Parameter** | **Description** | **Jop and Taberlet** | **Trento** |
|---|---|---|---|
| | Collision between two spheres | | |
| | | glass | polystirene |
| e [-] | normal rest. coeff. | 0.8-0.97 | 0.95 |
| $\mu$ [-] | Friction coeff. | 0.048-0.177 | 0.189 |
| $\beta$ [-] | Tangential rest. coeff. | 0.37-0.25 | 0.46 |
| $d$ [mm] | Particle diameter | 0.52 | 0.52 |
| $\rho$ [kg/m$^3$] | Solid density | 2500 | 980 |
| | Collision particle-side-walls | | |
| | | glass-glass | polystirene-plexigass |
| $\mu_w$ [-] | Friction coeff. | 0.4 | 0.24 |
| E [GPa] | Young modulus | 68.9 | 3.3 |
| $\nu$ [-] | Poisson coeff. | 0.23 | 0.37 |

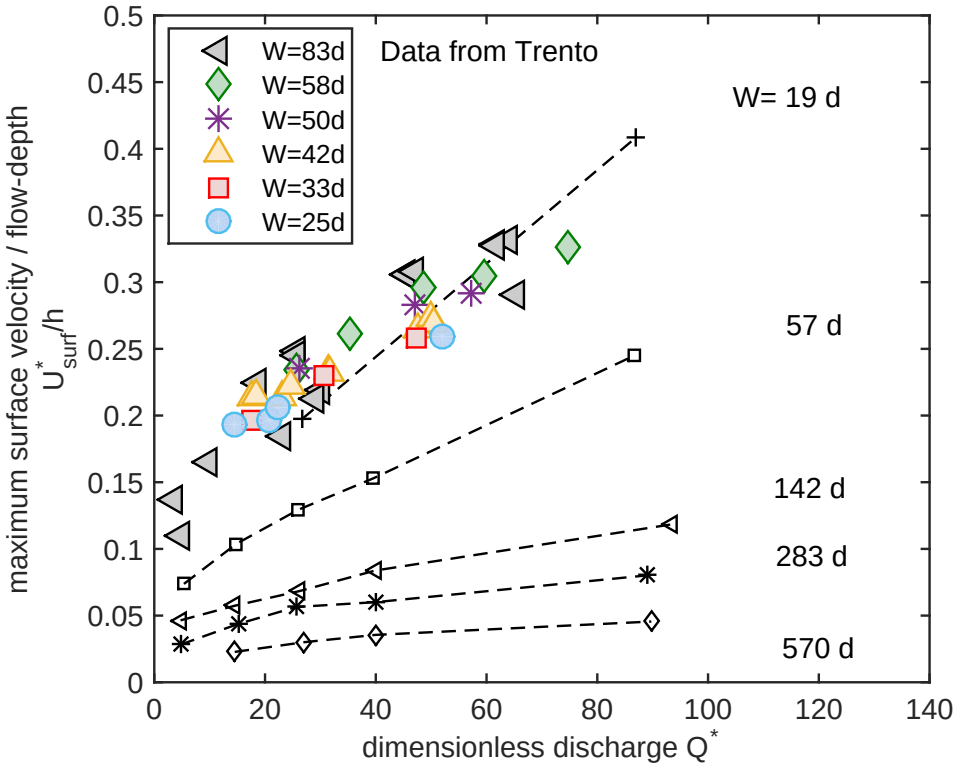


Figure 4.31: Comparison with the experiments performed by Jop (grey lines). Estimation of the non-dimensional global shear rate against the dimensionless discharge. The gray lines are data from Jop, while the coloured symbols are experiments performed in Trento.

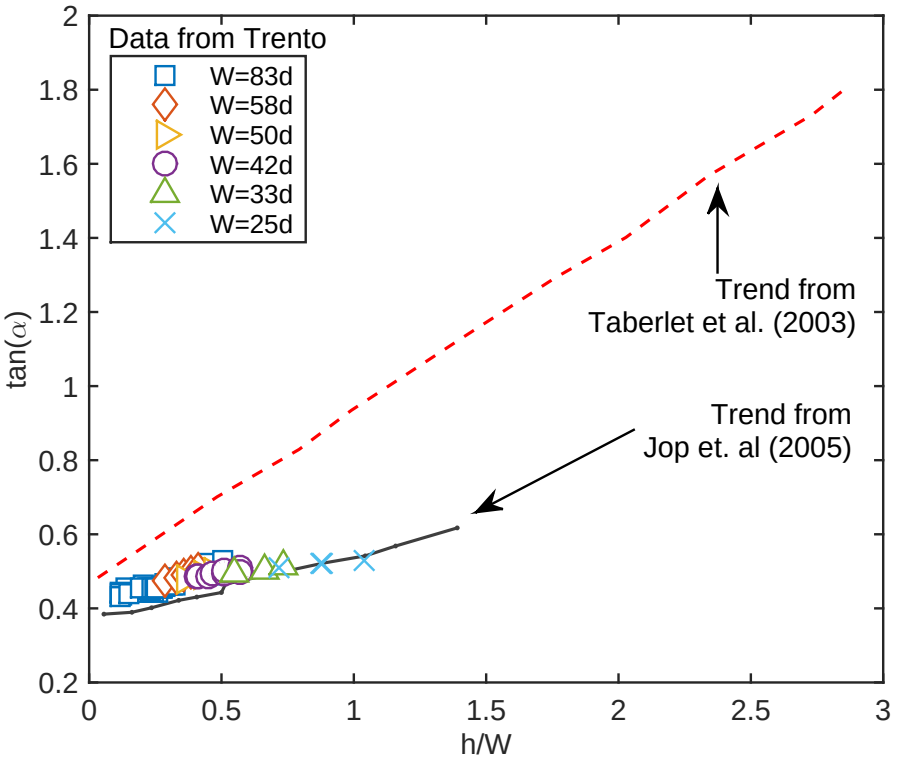


Figure 4.32: Comparison with the experiments performed by Jop (solid line) and Taberlet (dashed line). Free surface slope for the ratio between the flow-depth and the width.

while they diverge by increasing the discharge. Although there is a dependence of the surface velocity on the width, it seems to be less important in comparison to the experiments performed by Jop. In fact, the rate at which the velocity changes with the discharge is the same for all the widths, and it seems to be higher than what was found by Jop.

2. The flow obtained during the experiments is more superficial than the flow reproduced by Jop as shown in figure 4.30(b)

3. Figure 4.31(b) shows an estimate of the shear rate for different widths as function of the flow rate. As pointed out also by Jop (2004), the shear rate is not independent of the discharge, but it increases with it. However, the dependence on the width is less accentuate, and the points seem to collapse on the same curve. The difference might rely on two reasons: the different definition of the flow-depth and the different configuration used to perform the experiments.

4. Taberlet reaches higher values of the free surface slope in comparison with the experiments of Trento and Jop. It might be due to the fact that he worked with higher flow rates, at which he obtained larger ratio of the flow-depth over the width and a more collisional regime.

## 4.9 Measurements of the collisional properties

To have a fully characterization of the dynamics of the flow at the side-walls a series of experiments was performed measuring the angle of rebound of the particles against a flat plate of the same material and characteristics of the wall.

Given the typical particle diameters and velocities of the experiments, the the effects of air resistance on a falling particle are negligible.

Experiments have been carried out with 0.5 mm plastic spheres rebounding from a thick plexiglass plate for a range of impact angles from normal to near-glancing.

The drop height was initially changed in the case of the normal impact to study the dependence of the restitution coefficients on the impact velocity. After having seen that the height does not have a great influence on the coefficient values, it was set at a fix value of $h = 15\,\mathrm{cm}$, corresponding to an impact speed of $1.7\mathrm{m\,s^{-1}}$.

As described in section 2.4 the oblique collision of a sphere with a flat surface can be fully described by studying the classic rigid-body theory. The ratio of the rebound and impact speed is the overall coefficient of restitution $\widehat{e}$ that is equal to

$\widehat{e} = \mathbf{g}_r/\mathbf{g}_i$, where the symbols are the same indicated in figure 4.33. For the present case of zero initial spin (section 3.4.1) the following relations are valid:

$$e = -\frac{\mathbf{c}' \cdot \mathbf{n}}{\mathbf{c} \cdot \mathbf{n}}; \qquad \beta_0 = \frac{\mathbf{c}' \cdot \mathbf{t}}{\mathbf{c} \cdot \mathbf{t}}; \qquad \mu = \frac{|\mathbf{J} \cdot \mathbf{t}|}{\mathbf{J} \cdot \mathbf{n}} \tag{4.23}$$

Furthermore, the results are analysed defining:

$$v_y = \mathbf{c} \cdot \mathbf{c}; \qquad v_x = \mathbf{c} \cdot \mathbf{t} \tag{4.24}$$

Values of the normal and tangential coefficient of restitution are plotted in figure 4.34 for different angles of impact. The normal coefficient of restitution varies between 0.8 and 0.6, over the range of impact angles from 0° (normal) to 70° (near glancing) with an average of 0.753. The scatter of the points are dependent on the non-perfectly similarity of the particles used in the analysis, since they are characterized by a certain dispersion of the physical and mechanical properties, as the surface roughness and diameter. The tangential coefficient of restitution, plotted in figure 4.34 with circle symbols, has a clear variation with the impact angle reaching a minimum value of 0.6 close to $\theta = 20°$, and approaching 1 only for glancing incidence.

The trend is characteristic of nearly elastic collisions. However, as highlighted also by Kharaz *et al.* (2001), these values entail that the a significant part of initial kinetic energy is partly converted in rotational energy, and partly it is lost by friction and other dissipation processes.

The measurements of normal and tangential restitution coefficient refer to motion of the centre of gravity of the sphere. To get information about the behaviour of the contact patch, the non-dimensional angles are computed according the Maw-representation.

Considering figure 4.35,a plot of $\psi_2$ over a sufficient range of $\psi_1$ yields two linear regimes defining the domains of sticking and sliding contact. The two parameters $\beta_0$ and $\mu$ my be determined either from the slopes and intercepts produced by regression analyses of the two regimes, or from the values produced by the coefficient definition appropriate to each regime.

All the parameters are summarised in table 4.3

Table 4.3: Coefficients describing the collision between a plastic sphere used in the experiments and a flat plate of plexiglass, representing the side-wall

| parameters | values |
|---|---|
| $\mu_w$ | 0.24 |
| $\beta$ | 0.29 |
| $e_{nw}$ | 0.75 |
| $e_{eff}$ | 0.46 |

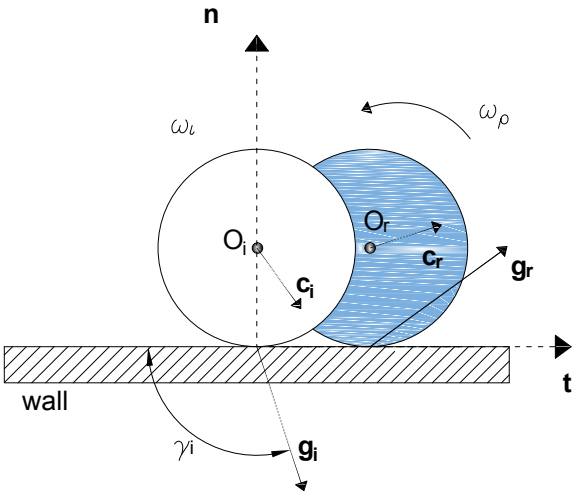


Figure 4.33: Scheme of a sphere colliding against a plate. The reference system is defined with respect to the plate, considering the normal and the tangential vectors to it. The dark particle is the rebounding sphere, whose properties are designates with the index $r$. The translational velocity is defined as $c$, while the angular velocity with the symbol $\omega$. The velocity at the point of contact is indicated with the symbol $g$. The incidence angle is $\gamma$, and it is defined with respect to the plate.

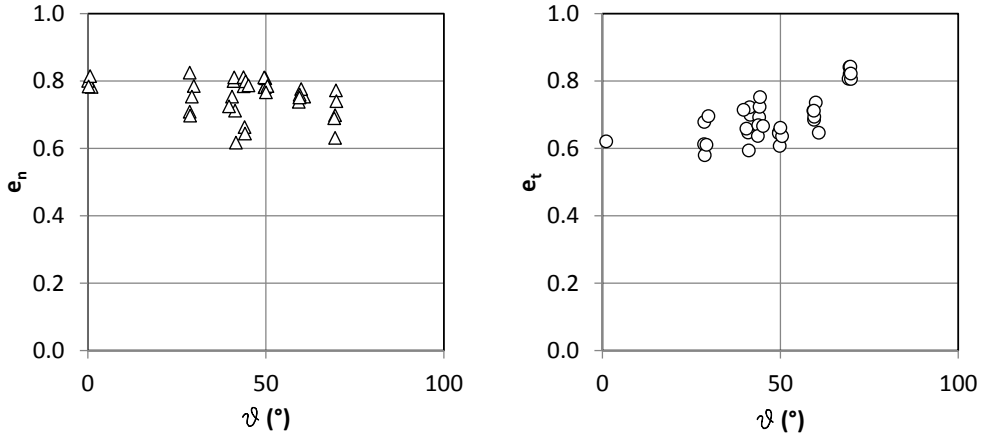


Figure 4.34: Variation of the normal and tangential coefficient of restitution with the vertical component of the velocity

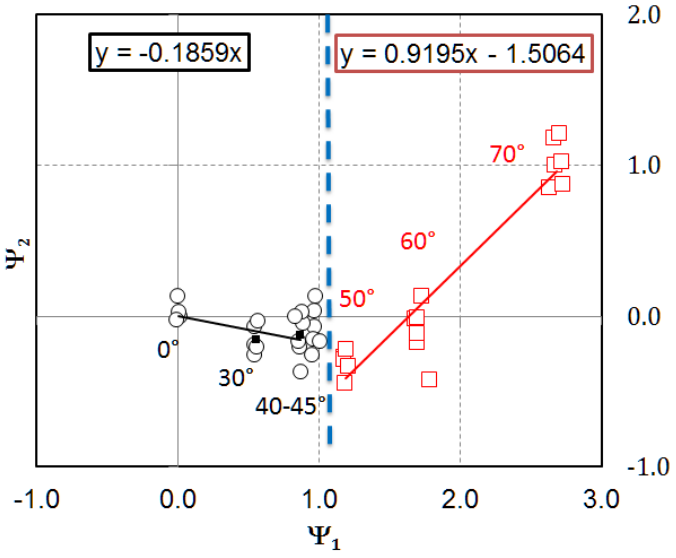


Figure 4.35: The non dimensional rebound angle is represented against the non-dimensional impact angle according to the Maw's analysis. Two distinct regimes can be identified. At the left the sticking region and at the right the sliding region. From the intercept and the slope of the two curves the two parameters $\mu$ and $\beta_0$ can be derived.

# Chapter 5

# Analysis and discussion

## 5.1 Global relationships

In this section global features of the experiments are analysed and discussed, considering the overall relations that link the physical quantities measured in the tests.

#### Considerations on the velocity

Unlike mixtures of solid and water that are mainly characterized by strong vertical variations of the physical quantities, dry granular flows also display transversal gradients. The surface velocity is a good example of this behaviour, since it is not constant along the z-direction but varies from the side-walls to the center-line where it reaches a maximum value. Therefore, when considering surface variables, it is useful to specify which value is taken into account.

The analysis of the whole dataset shows that the mean and the maximum values of the surface velocity are linearly correlated, and they keep the same proportion for all the widths (the mean velocity is always lower than the highest speed by 10%, figure 5.1 (a)). Consequently both values can be used indifferently during the global analysis.

For the lateral quantities, figure 5.1 (b) shows the difference between the depth-average velocity $U_{lat}$, computed averaging the velocity measured at the side-walls over the flow-depth, and the bulk velocity, as it has been defined in the previous chapter:

$$\{U_{lat}\} = \frac{Q}{W\overline{h}} \tag{5.1}$$

where the considered $\overline{h}$ is the flow-depth measured at the side-walls. The discrepancy between the two values, especially for the highest discharges, depends on two factors: i) the first aspect is correlated to the flow-depth, whose increase with the discharge

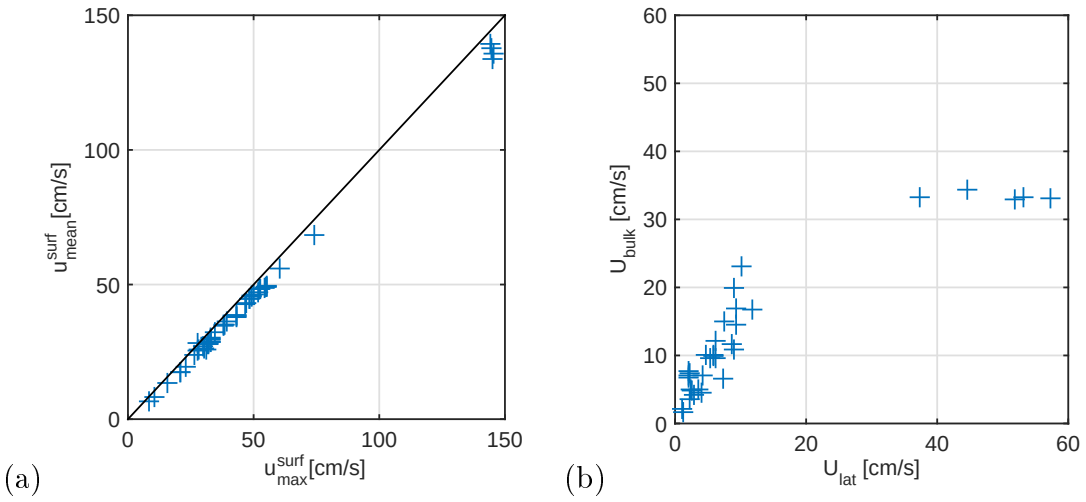


Figure 5.1: (a) Mean and maximum values of the surface velocity. The proportion between the two values remains constant for all the experiments analysed. (b)Comparison among different definitions of the lateral velocity. $U_{lat}$ is the depth averaged velocity computed at the side-walls from the lateral recordings, while $U_{bulk}$ is the bulk velocity computed from the discharge

is not linear, but it tends to a "saturation" value ii) the second aspect is due to the transversal gradients both of the velocity and of the flow-height. Therefore the values computed averaging the measurements at the side-walls will be different from the values derived from a bulk estimation made from the discharge.

### Froude number scale

Experimental data are interpreted considering the Froude scale. Two different definitions of the Froude number can be considered:

1. a lateral Froude number:

$$Fr_{lat} = \frac{U_{lat}}{\sqrt{g\overline{h}}} \tag{5.2}$$

   which is computed using the depth average velocity measured at the side-walls, $U_{lat}$, and the flow-depth, $\overline{h}$, defined from the vertical profiles.

2. a surface Froude number:

$$Fr_{surf} = \frac{U_{surf}}{\sqrt{g\overline{h}_{bulk}}} \tag{5.3}$$

   where $U_{surf}$ is the cross-wise average of the surface velocity, while $\overline{h}_{bulk}$ is a bulk estimate of the flow-depth, defined in this case as:

$$\overline{h}_{bulk} = \frac{Q}{W\,U_{surf}} \tag{5.4}$$

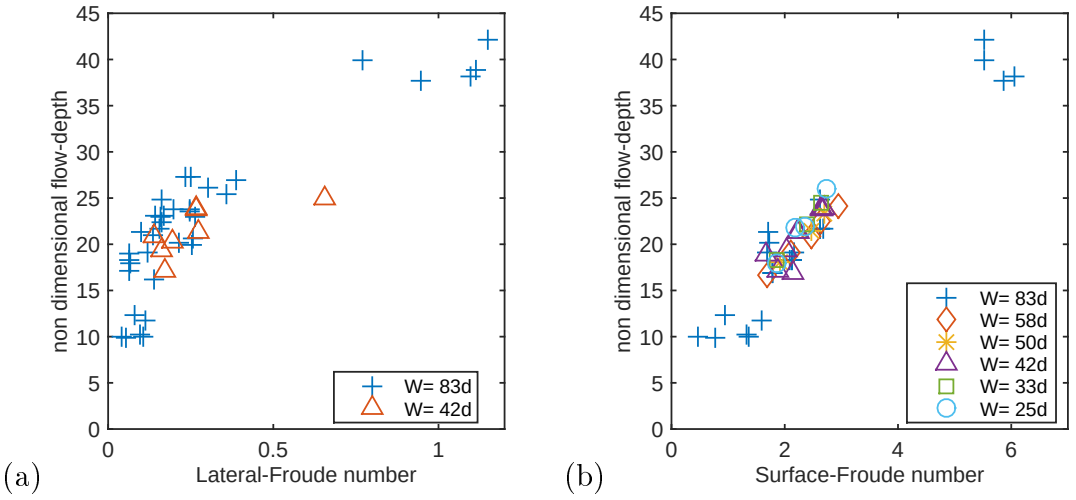


Figure 5.2: Variation of the flow-depth with the Froude number. In (a) lateral velocity is considered to compute the Froude number, while in (b) surface variables are used

The two definitions lead to very different values, since the depth average velocity is always lower than the cross-wise one, since it is evaluated considering the fastest part of the flow. A bulk flow-depth is employed for the surface Froude number, because lateral measurements are not available for all the runs, especially for those carried out at different widths.

Figure 5.2 shows the variation of the non dimensional flow depth $\overline{h}/d$ with increasing values of the Froude number. The trend follows a power law, $h/d = a\,(Fr_{lat})^b$, if the lateral Froude is considered, with $b$ equal to 5/2 (figure 5.2 (a)).

By contrast, in the case of the surface Froude number, the correlation seems to be strongly linear and independent of the width (figure 5.2(b)).

## 5.2 Hydraulic approach

Considering the experimental observations made in the previous chapter, it seems that by enlarging the channel, for the same specific discharge, there is a transition of regime, from a frictional regime to a collisional one, from shear-independent to shear dependent, at least at the layers near the free surface. The definition of the flow-depth adds complexity to the problem, since its position is not an independent parameter of the system, but it is inherently coupled with the flow dynamics.

Therefore it is not clear whether the overall behaviour is a consequence of a "local rheology", as derived by Taberlet *et al.* (2003), who considered also the width as a specific parameter to describe the rheology of confined channel flows, or it depends on a variation of the regime, where the width plays a role only as a boundary condition.

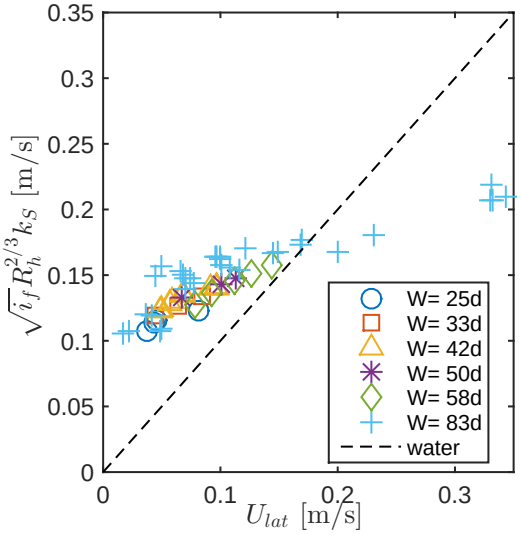


Figure 5.3: Interpretation of the data using the Gauckler formula, $U = k_S i_f^{0.5} R_h^{2/3}$

In the latter case granular flows would behave like Newtonian fluids, which can be either laminar or turbulent.

From these considerations, we try to verify whether an hydraulic approach is feasible, treating granular flows as homogeneous fluids and adopting models that are indicative of the granular regime and the type of contacts among particles.

In this section the data are interpreted according the classical laws of hydraulics, but considering the global variables relative to granular flows. Like the fluids, also in this case a hydraulic radius is defined as:

$$R_h = \frac{\overline{h} W}{2\overline{h} + W} \tag{5.5}$$

where the flow depth is measured at the side-walls. First the Gauckler-Manning relation is employed, then a more general resistance law is used to fit the experimental data.

1. The Gauckler-Manning relation correlates the average velocity of the flow with the channel bed slope $i_f$, considered equal to the free surface slope for uniform conditions, the hydraulic radius $R_h$, and the friction coefficient $k_S$.

$$U = k_S R_h^{2/3} i_f^{1/2} \tag{5.6}$$

The friction coefficient is defined as $k_S = 26/d_{50}^{1/6}$ (with $[k_S] = \mathrm{m}^{1/3}\mathrm{s}^{-1}$ and $[d_{50}] = \mathrm{mm}$ ) and $i_f = \sin\alpha$. Figure 5.3 shows that the lateral velocity is not predicted very well by the Manning law, being underestimated at higher dis-

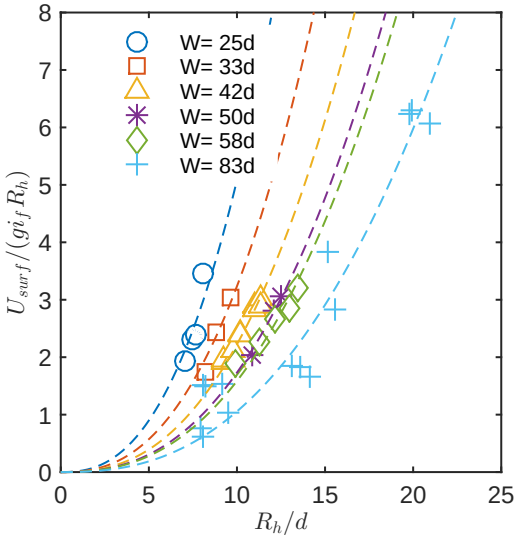


Figure 5.4: Resistance law $U_{surf}/u* = a(R_h/d)^b$, with $b = 2/5$, and the exponent $a$ varying as in figure 5.5. Application to the granular flows.

charges and overestimated for lower values of the flow rates. Indeed, for grain flows the dependence of the velocity on the flow-depth might be different from water, as highlighted also in Figure 5.2, where the flow-thickness is correlated with the Froude number by a power of 5/2

2. A more general resistance law can be written as:

$$\frac{U}{u^*} = a\left(\frac{R_h}{d}\right)^b \tag{5.7}$$

where the friction velocity is defined as $u^* = (g \cdot R_h \cdot i_f)^{0.5}$. The two parameters $a$ and $b$ can be inferred by the experimental data (figure 5.4). By reporting $U/u^*$ as function of the hydraulic radius, the exponent $b$ results to be equal to 2/5, as obtained also by considering the relation between the discharge and the flow-depth. However, although the exponent remains constant, the factor $a$ seems to vary with the widths, decreasing by enlarging the canal as shown in figure 5.5.

The above relationship (5.7) works well when the "roughness" at the walls is equal to the resistance at the bed. That does not occur for the considered flows, for which another approach is necessary. In the next section we will split the contributions given by the walls and the bed.

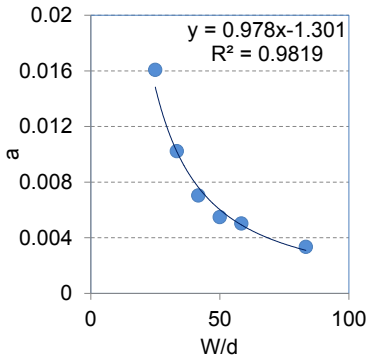


Figure 5.5: Variation of the coefficient $a$ with the width

### 5.2.1 Resistance law with a different roughness definition

Let's consider the balance of the forces in the direction of the motion for a control volume that is delimited laterally by the side-walls and below by the deposit, under the assumptions of steady and uniform conditions:

$$\tau_f \, W + 2\tau_l \, \overline{h} = \rho_s \, g \, \phi \, W \, \overline{h} \sin \alpha \tag{5.8}$$

Equation (5.8) stands that the weight of the solid particles in the control volume is balanced by the friction at the bed $\tau_f$, over the deposit, and by the friction at the side-walls $\tau_l$, along the flow-depth $\overline{h}$. In the expression, $\rho_s$ is the density of the particles, $W$ the width, $\phi$ the solid concentration, $\sin \alpha$ the free surface slope, which is taken equal to the slope of the deposit for uniform conditions.

Let's define the shear stress in terms of the mean velocity of the flow-depth as it is commonly done for water under uniform conditions. The generic friction stress can be written as:

$$\tau_{(i)} \propto \rho_s \, f_{(i)} \, U^2 \tag{5.9}$$

where $f$ is the friction factor that depends on the type of regime that characterizes the flow. In this case we can observe that particles move slowly near the deposit, where their motion can be captured by Couolombian relations, while they are more agitated near the side-walls. Therefore, the following assumptions can be done on the coefficient $f_{(i)}$:

1. near the deposit the regime can be similar to a laminar flow, so that the coefficient $f_f$ may be defined in terms of the local Reynolds number:

$$f_f \propto \frac{1}{R_e} = \frac{\nu}{U \, d} \tag{5.10}$$

where $\nu$ is the viscosity, which can be considered similar to that of water.

2. near the side-walls the regime can be seen as turbulent, and $f_l$ may be considered independent of the velocity and it assumes a constant value, which can be range from $0.001 - 1$ as for water.

The relations for the friction stresses become:

$$\begin{aligned} \tau_f &\propto \rho_s \nu/(U\, d) \\ \tau_l &\propto \rho_s\, f_l\, U^2 \end{aligned} \tag{5.11}$$

Substituting eq.(5.11) in eq.(5.8), multiplying all the terms for $(gdd)$, and considering the following dimensionless variables:

$$U^* = \frac{U}{\sqrt{gd}} \tag{5.12}$$

$$Q^* = \frac{Q}{W\, d\sqrt{gd}} = U^* \frac{h}{d} \tag{5.13}$$

$$W^* = W/d \tag{5.14}$$

The force balance can be written as:

$$U^* W^* \frac{1}{\frac{d\sqrt{gd}}{\nu}} + 2\, f_l Q^* U^* = \phi \frac{W^* Q^*}{U^*} \sin\alpha \tag{5.15}$$

The free-surface slope can be expressed in terms of the ratio $h/W$, through a power relation whose coefficients can be fitted by the experimental data:

$$\sin\alpha = a \left(\frac{h}{W}\right)^b = a \left(\frac{Q^*}{W^* U^*}\right)^b \tag{5.16}$$

with $b < 1$. Substituting in eq.5.15 and grouping the constant terms in the following coefficients:

$$\begin{aligned} A &= \frac{\nu}{d\sqrt{gd}} \\ B &= 2\, f_l \\ C &= a\, \phi \end{aligned} \tag{5.17}$$

the force balance becomes an expression of the dimension-less velocity in terms of the dimension-less width, through the parameter $Q^*$:

| symbol | units | value |
|---|---|---|
| $d$ | m | 0.0006 |
| $\nu$ | $m^2s^{-1}$ | $10^{-2} - 10^{-5}$ |
| $f_l$ | – | 0.01 |
| $a$ | – | 0.74 |
| $b$ | – | 0.169 |
| $\phi$ | – | 0.6 |

Table 5.1: Parameters used in the equation 5.19. The constants $a$ and $b$ have been fitted by the experimental data

$$AU^*W^* + B\,Q^*U^* = C\frac{W^{*(1-b)}Q^{*(b+1)}}{U^{*(b+1)}} \tag{5.18}$$

$$U^* = \left[C\frac{W^{*(1-b)}Q^{*(1+b)}}{AW^* + B\,Q^*}\right]^{1/(b+2)} \tag{5.19}$$

where it is always $0 < b < 1$

The above equation has been plotted in figure 5.6 and 5.2.1, using the constants listed in table 5.1

Figure 5.6 displays the variation of the dimensionless velocity with the width, for different values of the dimensionless discharge. The simple model shows that the velocity $U^*$ has always a maximum in the transition between the two regimes, from a "viscous" regime to a "turbulent" one. Additionally it predicts the velocity reduction with the width and the tendency towards an asymptotic value for each discharge, independent of the width. The initial peak tends to be less sharp but higher as the viscosity decreases.

The influence of the coefficient $f_l$ is less strong. If it increases from 0.01 to 0.1, the peaks of the curves in figure 5.2.1 become smoother and a little lower.

In figure 5.9 the experimental points have been superimposed on the theoretical curves computed by choosing a proper value for the viscosity. Although the expression (5.19) does not represent a model to predict the velocity, since it was derived without a proper rheology, the comparison between the theoretical curves and the data is quite good. The maximum of the velocity exhibited by the experimental points at lower values of the width is reproduced adequately by the expression.

The main differences arise at larger widths, where the experimental data seem to decay faster than what is suggested by the expression. It might be due to the function chosen to define the free surface slope, which is not good to predict low ratios of the flow-depth over the width. Looking at the experimental data, $\sin\alpha$ varies with $\overline{h}/W$ with a sigmoid function,

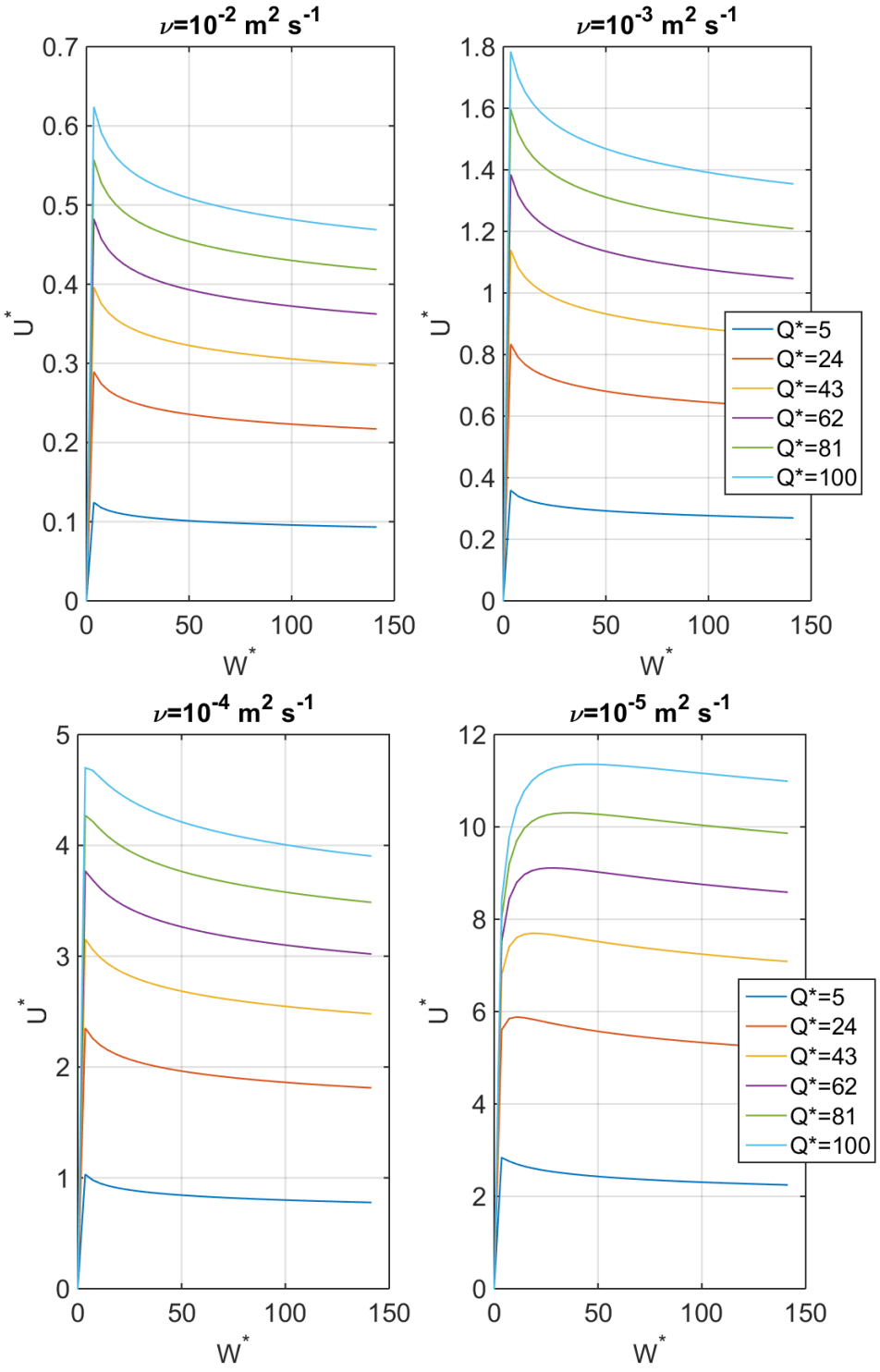


Figure 5.6: Variation of the dimension-less velocity with the width for different values of the viscosity

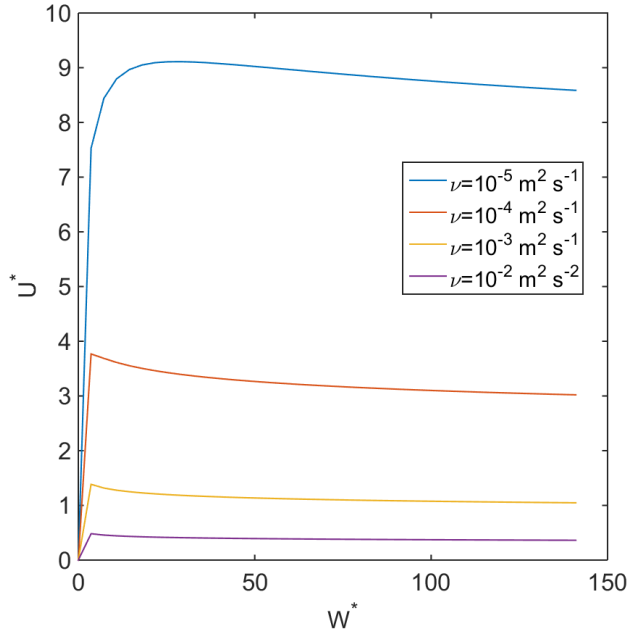


Figure 5.7: Variation of the velocity for different values of the viscosity but for the same discharge and turbulent coefficient $f_l$

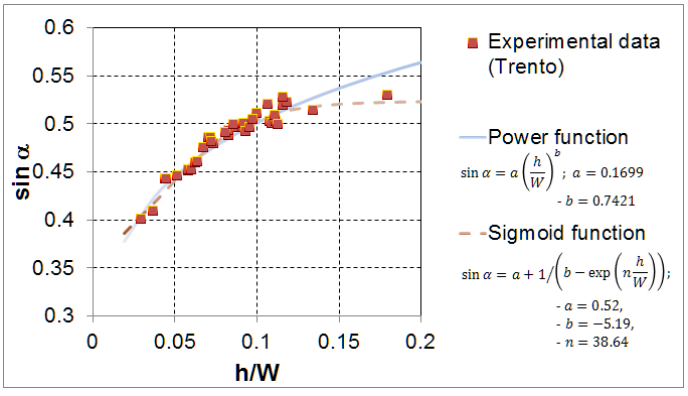


Figure 5.8: Different relations to define the free surface slope as a function of the ratio $h/W$

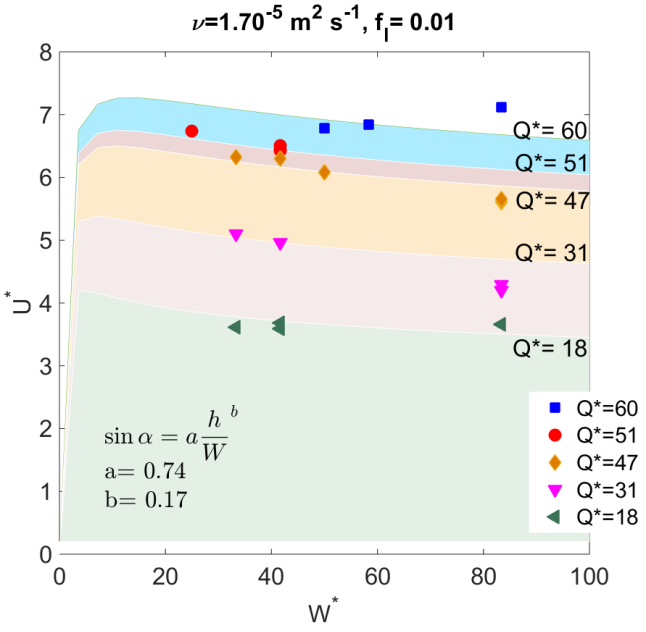


Figure 5.9: Experimental points on the theoretical curves. All the parameters are reported on the plot

### 5.2.2 Coulombian relation near the deposit

Let's consider the force balance written in equation (5.8). The friction stress at the deposit can be expressed through a Herschel-Bulkley relation:

$$\tau_f = \phi\, g\, \rho_s\, \overline{h} \tan\phi_f + \nu_0 \left(\frac{\partial U}{\partial y}\right)^k \tag{5.20}$$

where $\tan\phi$ is the tangent of the internal friction angle of the material, $\nu_0$ is the viscosity and $k$ is a coefficient that ranges from 0 to 1. In a first instance we can assume $k = 0$ and the previous expression reduces to the following one:

$$\tau_f = \phi\, g\, \rho_s\, \overline{h} \tan\alpha_f + \nu_0 \tag{5.21}$$

So that, by making some algebraic simplifications, the balance can be written again as:

$$A_1\, W^*\, Q^*\, U^{*b} + B_1\, W^*\, U^{*(1+b)} + C_1\, Q^*\, U^{*(2+b)} - D_1\, Q^{*(1+b)}\, W^{*(1-b)} \tag{5.22}$$

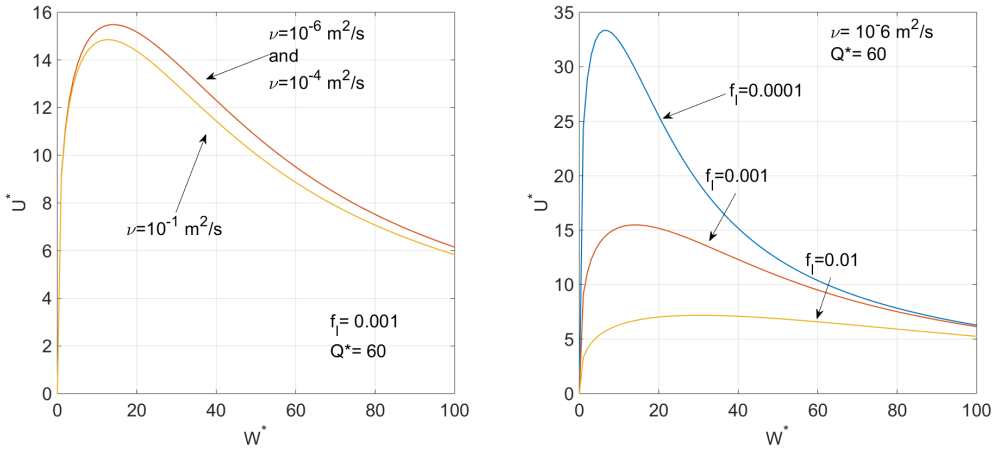


Figure 5.10: Variation of the velocity for different values of the viscosity and of the friction factor for the lateral contribution of the shear stress

where the variable $U^*$, $W^*$ and $Q^*$ are those defined in equation 5.18, while the constants $A_1$, $B_1$, $C_1$, $D_1$ are:

$$\begin{aligned} A_1 &= \phi \, \tan \phi_f; \\ B_1 &= \tfrac{\nu_0}{\rho \, g \, d}; \\ C_1 &= 2 \, f_l; \\ D &= a \, \phi. \end{aligned} \tag{5.23}$$

The above equation is implicit in $W^*$ and can be solved by using a Newton-Raphson procedure, once all the constants are fixed.

### More precise definition of the bottom friction

The bottom friction can be defined through a Coulombian relation by considering the weight of the material that slides over the deposit, and more precisely the perpendicular component of the weight to the inclined surface. Under the conditions of uniformity, the slope of the deposit corresponds to the one of the free surface. So that a more correct definition of $\tau_f$ is:

$$\tau_f = \phi \, g \, \rho_s \, \overline{h} \cos \alpha \tan \phi_f + \nu_0 \left( \frac{\partial U}{\partial y} \right)^k \tag{5.24}$$

In order to simplify the relation, and to obtain an equation where the width and the velocity are the only unknowns, we express $\cos \alpha$ as a linear function of $\sin \alpha$,

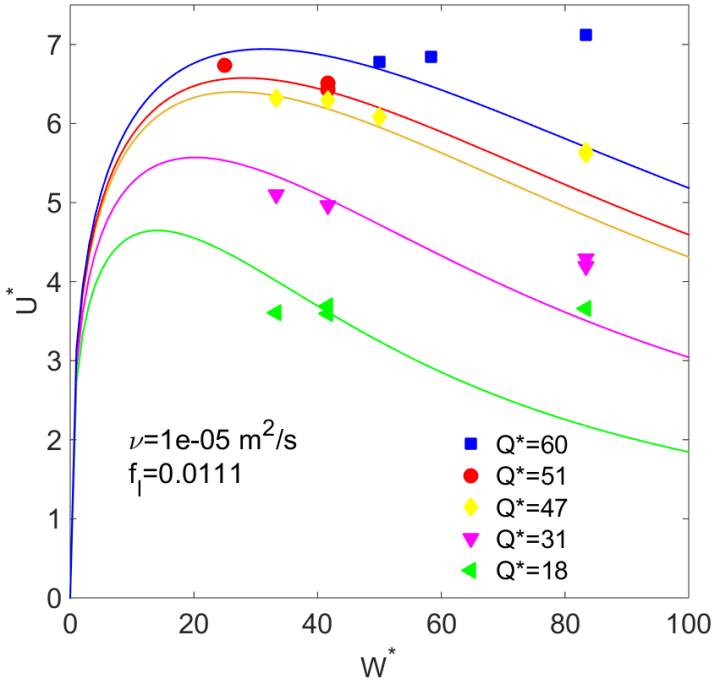


Figure 5.11: Experimental data on the theoretical curves. Parameters for the friction terms are reported at the bottom of the plot

since the the angle $\alpha$ has a very narrow range of variation, corresponding to a short chord of the trigonometric circle. So that, after substituting the terms in the balance equation, the final expression reads as:

$$A_2\, W^{*(1-b)}\, Q^{*(1+b)} + B_2\, Q^*\, W^*\, U^{*b} + C_2\, W^*\, U^{*(1+b)} + D_2\, Q^*\, U^{*(2+b)} = 0 \qquad (5.25)$$

where:

$$\begin{aligned} A_2 &= a\rho\,\phi\,(m\tan\phi_f - 1)\,; \\ B_2 &= \phi\rho q; \\ C_2 &= \tfrac{\nu_0}{g\,d}; \\ D_2 &= 2\,\rho f_l \end{aligned} \qquad (5.26)$$

## 5.3 Rheological interpretation

In this section experiments are interpreted according the kinetic theory for dense gases as formulated by Jenkins and Savage (1983), Jenkins and Richman (1985), and Jenkins and Hanes (1998) and its extension proposed by Jenkins (2007). In addition a comparison is made by using the novel approach developed by Armanini *et al.* (2014) for submerged mixtures of solids and water.

The collisional stresses are defined in chapter 2, but we briefly recall them here, referring to the previous chapter for the definition of the constants.

1. Standard kinetic theories:

$$p^{coll} = (1 + 4Cg_0\eta_p)C\rho T; \qquad \tau^{coll} = \mu^{coll}\dot{\gamma} \tag{5.27}$$

2. Extended kinetic theories:

$$p^{coll} = (4\rho g_0 T); \qquad \tau^{coll} = \mu^{coll}\dot{\gamma} \tag{5.28}$$

   where $g_0 = 0.85C/(0.64 - C)$; $\mu^{coll} = (8J/5\pi^{1/2})\rho d g_0 T^2$ and $J = 1 + \pi/12$

3. For the heuristic model proposed by Armanini *et al.* (2014), the frictional stresses are derived according the following relations:

$$p^{fric} = p^g \frac{I_{s0}}{I_{s0} + I_s} \tag{5.29}$$

   and

$$\tau^{fric} = p^g \tan\alpha \frac{I_{s0}}{I_{s0} + I_s} \tag{5.30}$$

The distribution of the internal stresses is derived using the experimental values of particles concentration, granular temperature and velocity measured for different experiments. The shear rate is approximated as:

$$\dot{\gamma} \simeq \frac{\Delta u}{\Delta y} \tag{5.31}$$

where the variation of the vertical component along the $-x$ direction is considered negligible.

Figure 5.12, 5.13 and 5.14 represent the distribution of the normal and tangential stresses. Some considerations can be done:

1. Collisional stresses balance the stresses due to the weight near the free surface, while by approaching the bed they tend to zero.

2. By considering the heuristic approach proposed by Armanini *et al.* (2014) the parameter $I_{s0}$ was varied for each experiment to have the best fit between the collisional stresses predicted by the kinetic theory and those derived by the model. As depicted in figure 5.15, its value seems to be independent of the discharge, but it oscillates around a mean value, which can be considered as the "best fitting" parameter for the experiments in dry conditions. This mean value is equal to 0.017, lower than the value proposed by the Armanini *et al.* (2014). This might be due to the fact that in the computation of the strain tensor the term $\partial u/\partial z$ has much more importance in dry conditions with respect to the mixtures of solid and water. However, assuming that it is only a fraction of the vertical variation of the longitudinal velocity, we can write:

$$\dot{\gamma}_{dry} = \frac{\partial u}{\partial y} + \frac{\partial u}{\partial z} \simeq \frac{\partial u}{\partial x}(1+n) = \widehat{n}\dot{\gamma}_{water} \tag{5.32}$$

Therefore, in dry conditions the Savage number, defined as $I_s = (d\dot{\gamma})^2\rho/p$, is $\widehat{n}$ times larger than the Savage number defined for systems with water. With some algebraic operations, one can prove that this results into a smaller value of the parameter $I_{s0}$.

### Energy balance and comparison with the extended kinetic theories

For the collisional part of the flow we try to apply the new formulation of the kinetic theory given by Jenkins, pointing out the main differences that arise in the balance of the granular temperature. The analysis is presented here for three different discharges. As shown in chapter 2, for uniform and steady conditions the energy balance is composed of three terms, which represent the production, the dissipation and the diffusion terms.

For the standard kinetic theory these components are:

$$PROD = \mu\left(\frac{\partial u_i}{\partial x_j} + \frac{\partial u_j}{\partial x_i}\right)^2 \tag{5.33}$$

$$DIFF = \frac{\partial}{\partial x_j}\left(k_T\frac{\partial T}{\partial x_j}\right) \tag{5.34}$$

$$DISS = -f_5\rho_s\frac{T^{1.5}}{d} \tag{5.35}$$

For the extended kinetic theory there is a slight change in the dissipation term, where the diameter is substituted by the length of the correlations among the particles (see chapter 2 for more details). The value of the chain length is derived by

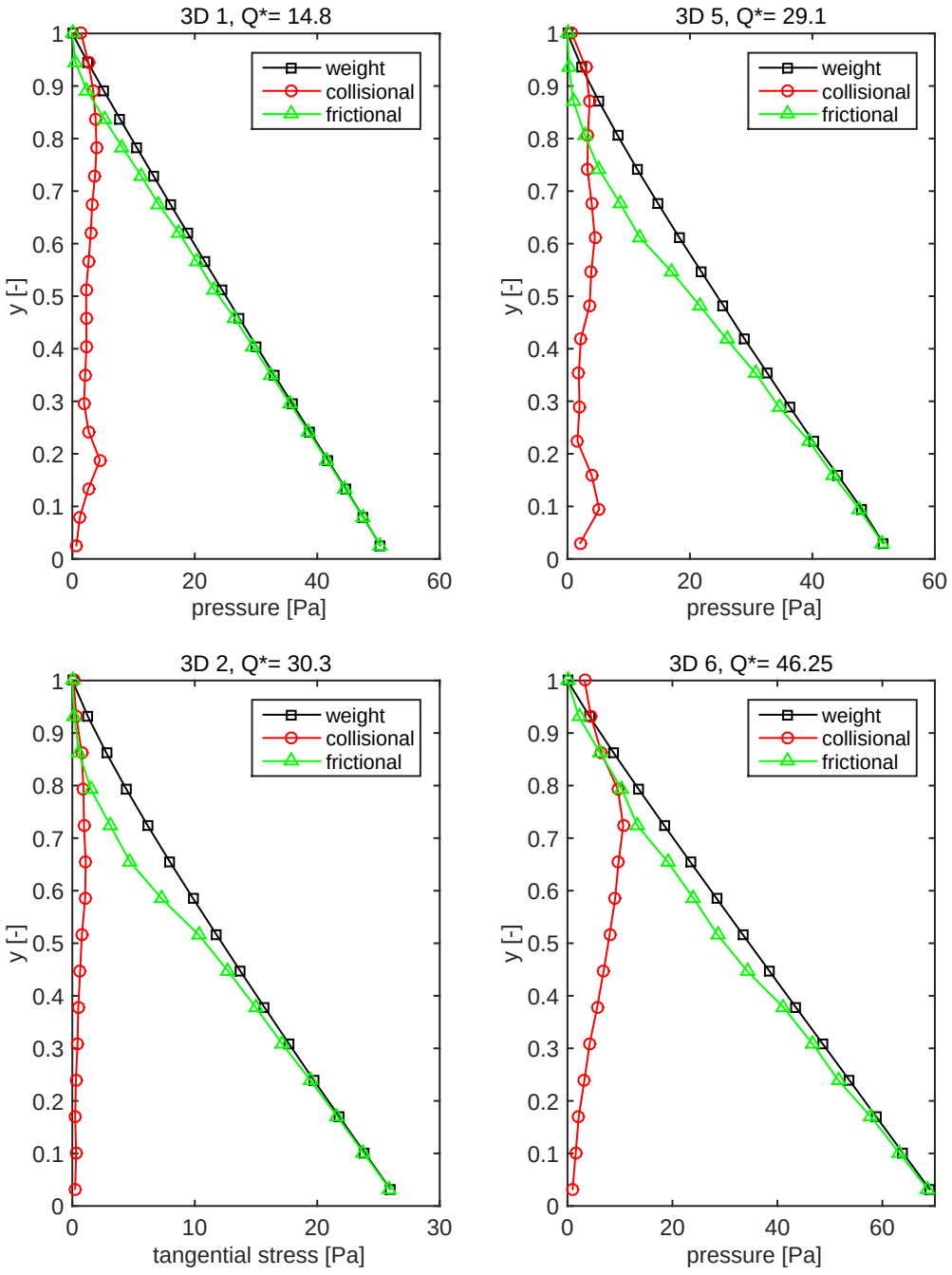


Figure 5.12: Distribution of the normal componenents for the internal stresses. The experiments are relative to increasing flow-rates.

the following expression:

$$\frac{L}{d} = \frac{1}{2}\left[\frac{30}{J}(1+e)c^2 g_0\right]^{1/3} \tag{5.36}$$

where the all the variables are defined in chapter 2.

To compute these terms, the experimental data are used, approximating the

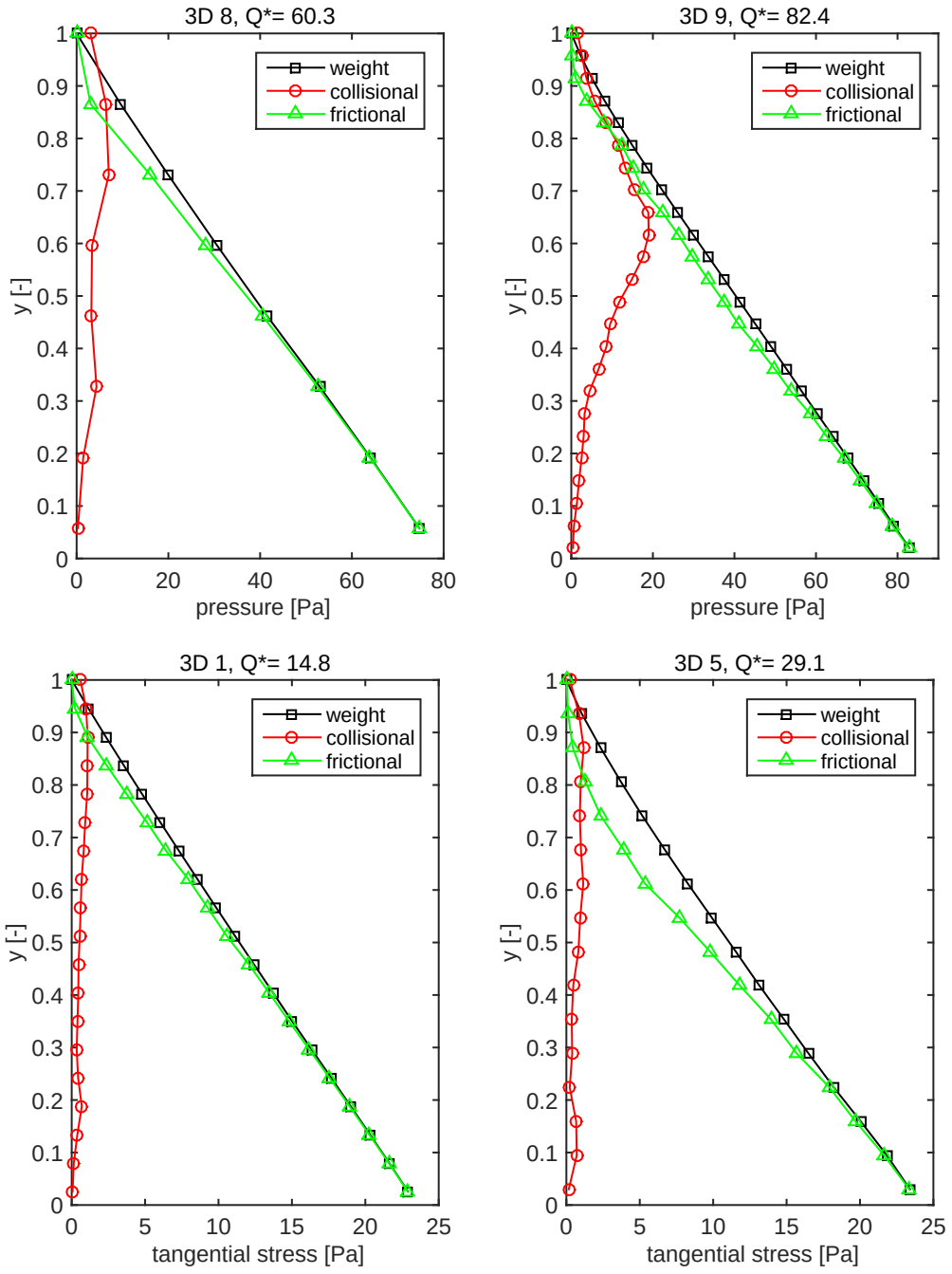


Figure 5.13: Distribution of the normal and tangential componenents for the internal stresses. The experiments are relative to increasing flow-rates.

derivatives in the following way:

$$\frac{\partial}{\partial y}\left(\frac{\partial T}{\partial y}\right) = \frac{\frac{T(y+\Delta y)-T(y)}{\Delta y} - \frac{T(y)-T(y-\Delta y)}{\Delta y}}{\Delta y} \tag{5.37}$$

In figure 5.16, 5.17 and 5.18 the terms are normalized with $\rho f\sqrt{gH}$

- The comparison among the two theories suggests that the extended kinetic

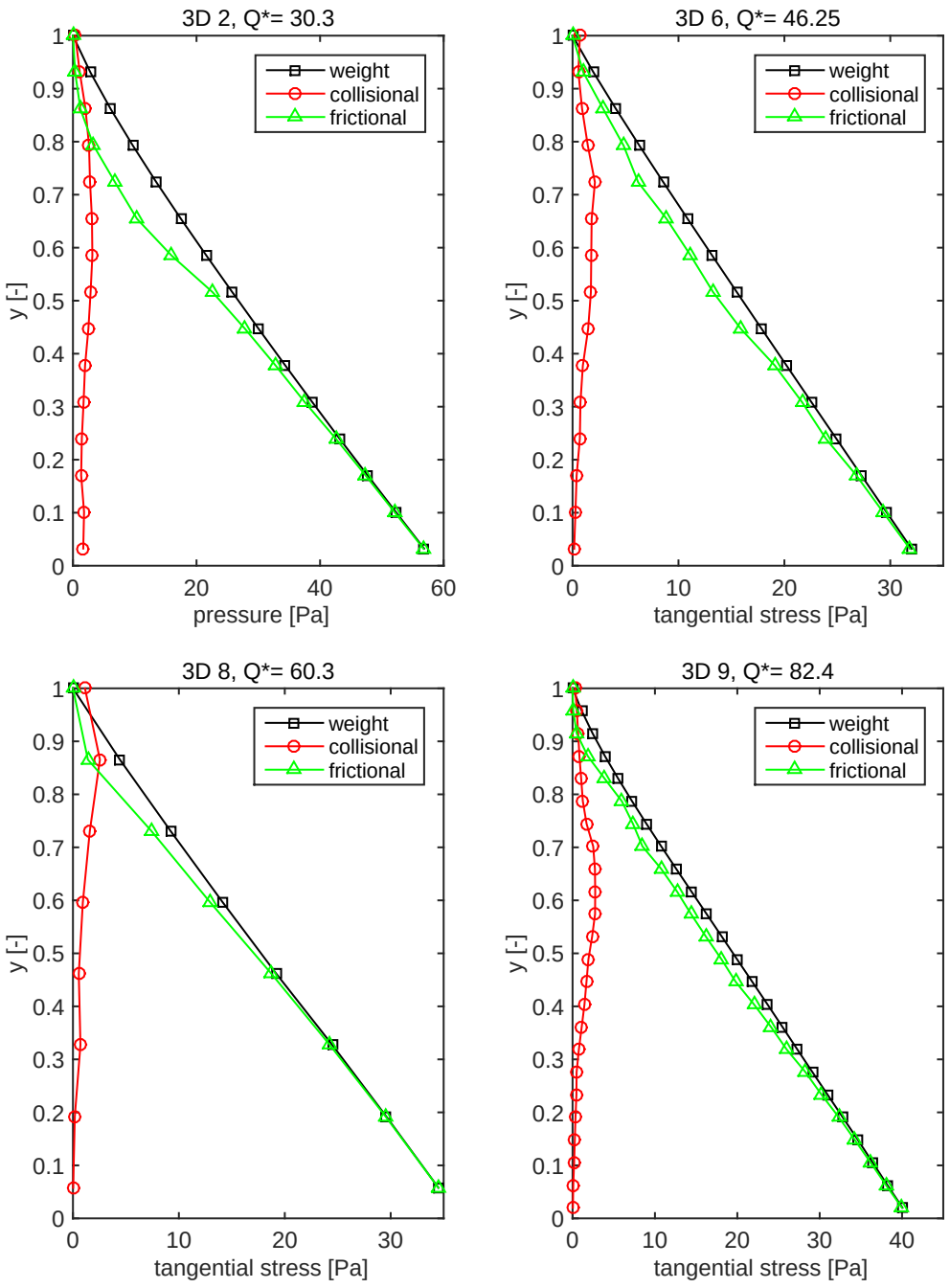


Figure 5.14: Distribution of the tangential componenents for the internal stresses. The experiments are relative to increasing flow-rates.

theory works better than the standard one to predict the tangential stresses, while they are equivalent for the pressure component of the particle stresses.

- As expected, the dissipation predicted by the extended theory is lower than the value derived by the traditional one, since the rate is computed by referring at the chain length of the particles that are in contact, instead of the single diameter.

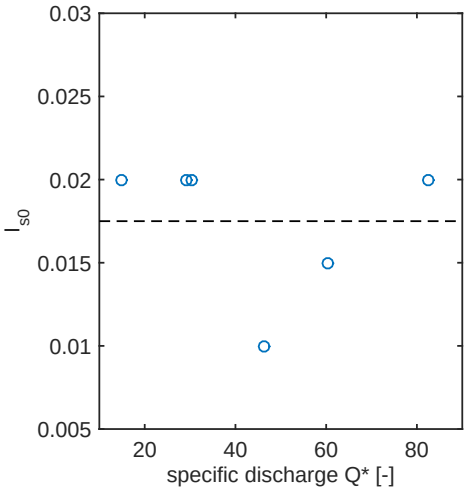


Figure 5.15: Variation of the parameter $I_{s0}$ with the specific discharge

- As a consequence of the different definition of the tangential stresses, the production term quantified by the extended theory is higher than the same term evaluated by the standard theory.
- For the diffusion term the two formulations are equivalent, predicting a nearly constant value through the flow-depth.

From the analysis it emerges that the balance can be considered qualitatively satisfied for all the experiments considered. However, the extended kinetic theory works better in comparison with the standard one, since it considers a correlation term that accounts for the frictional contacts among particles. This contribution is more important for lower discharges, where the frictional mechanism dominates throughout the flow-depth.

## 5.4 Comparison with mixtures of water and solids

Experiments carried out in dry conditions were compared with the results obtained for mixtures of solids and water by Armanini *et al.* (2005) and Larcher *et al.* (2007), who performed a series of experimental tests on uniform flow on the laboratory of Trento. Some interesting aspects can be highlighted. The first element that results from this comparison is that in presence of water steady flows on a loose bed are possible over a wider range of values of the flow-depth and concentration. As shown in figure 5.19, the height of the flow is 10 to 30 times the diameter of the solids when water is present as interstitial fluid, while in dry conditions the minimum depth to have steady conditions over a loose bed is much higher. This is due to the presence

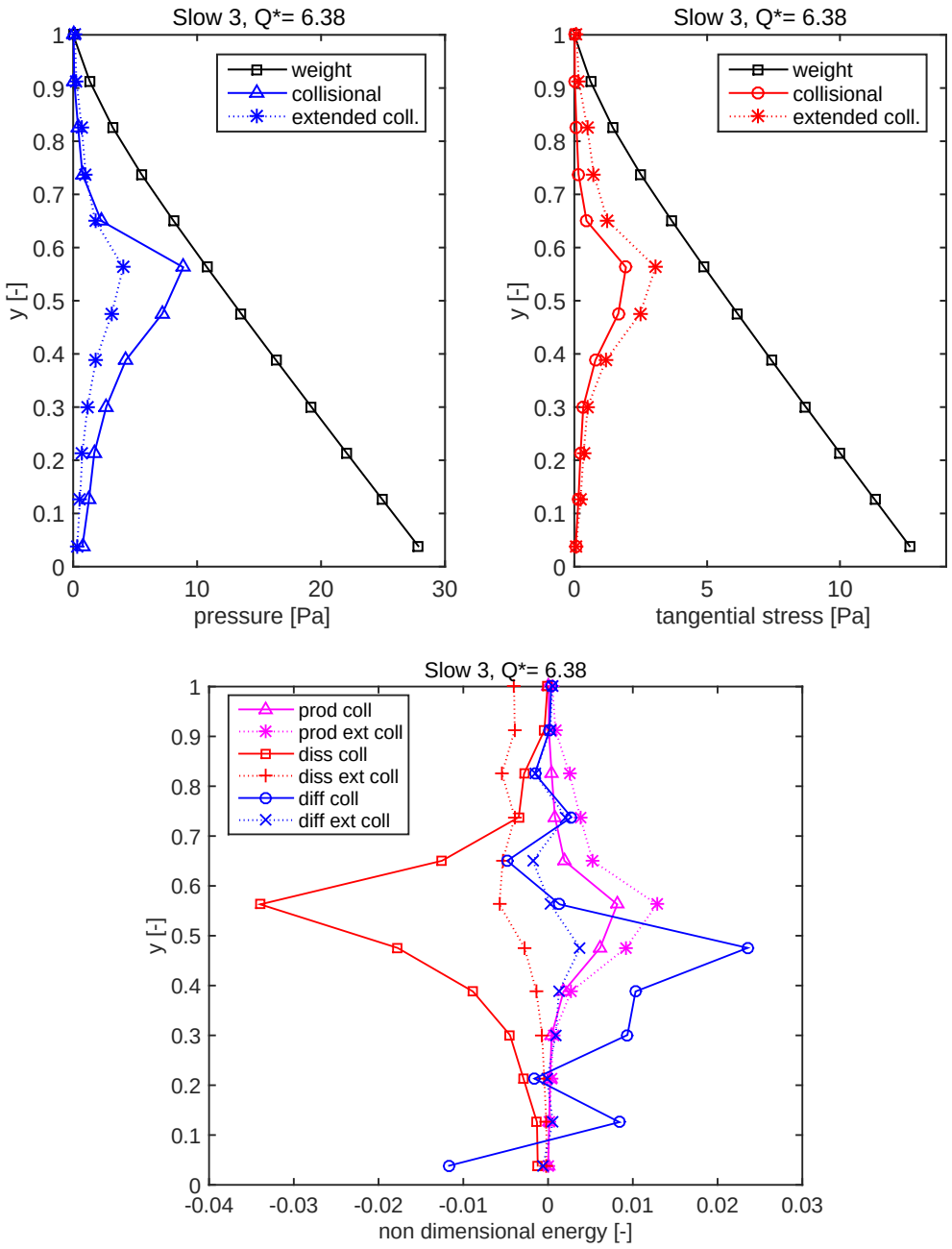


Figure 5.16: Comparison between the collisional stresses computed through the kinetic theory and the extended kinetic theory. Energy balance using the two different formulations

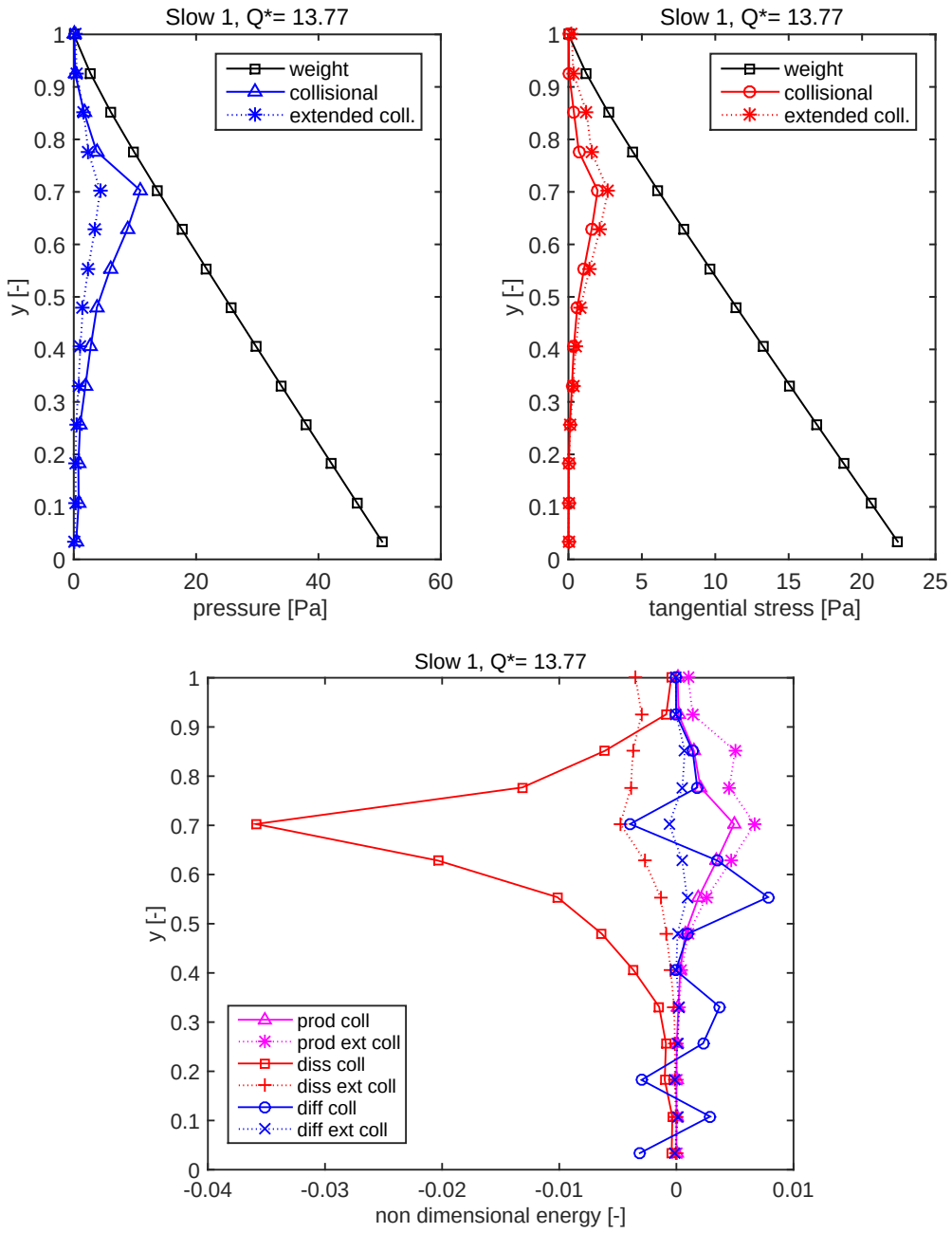


Figure 5.17: Comparison between the collisional stresses computed through the kinetic theory and the extended kinetic theory. Energy balance using the two different formulations

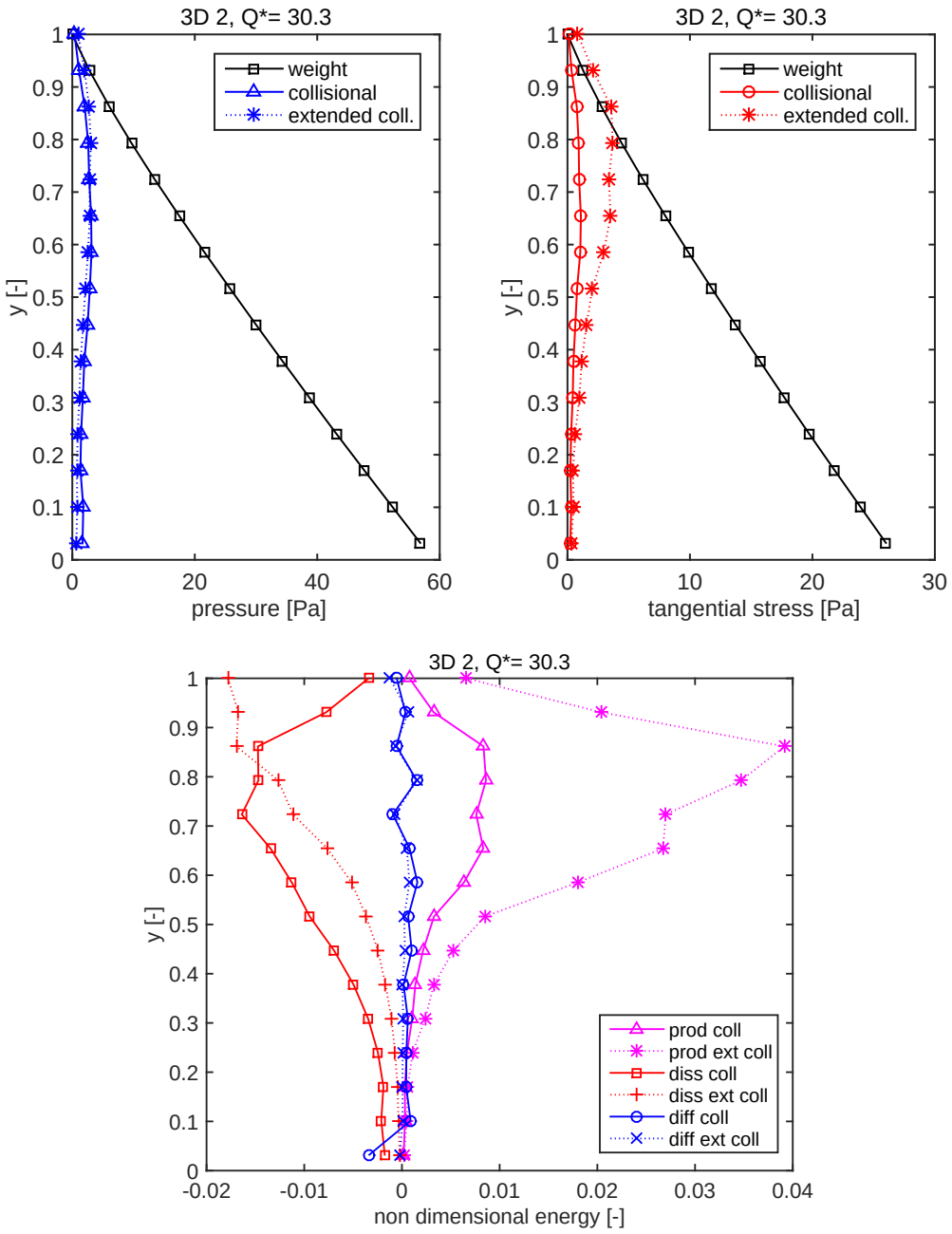


Figure 5.18: Comparison between the collisional stresses computed through the kinetic theory and the extended kinetic theory. Energy balance using the two different formulations

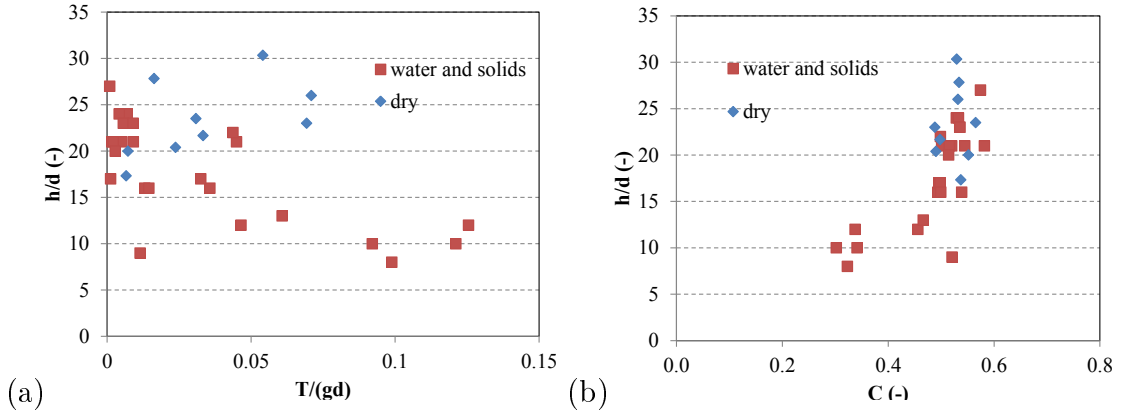


Figure 5.19: (a) Variation of the granular temperature with the flow-depth (average values) in submerged and dry conditions. (b) Range of values of the concentration for different flow-depths in the two systems

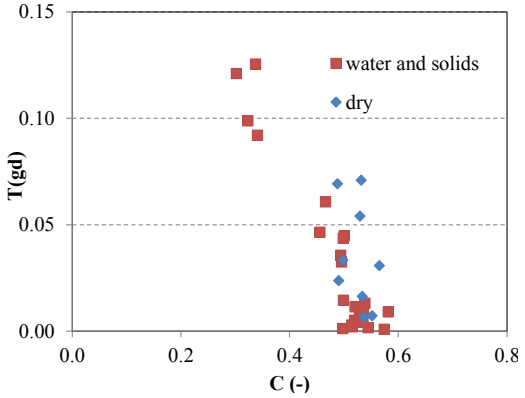


Figure 5.20: Average granular temperature and concentration for a submerged granular flow and for a flow in dry conditions

of a minimum discharge below which the static bed disappears, and the flow starts running over a rigid bed.

Figure 5.19 (b) shows that the depth average concentration $C$ is usually higher than 0.5 for dry material, while for submerged flows it tends to decrease by reducing the flow-depth. However, considering the same values of the non dimensional height, the estimated concentration of dry granular flows are in agreement with the results obtained for mixtures of solids and water.

Figure 5.20 confirms the aforesaid observations, representing the average values of the granular temperature computed for the two different systems. The granular temperature, normalized with respect to $(gd)$, covers the same range of values for similar concentrations.

# Chapter 6

# Conclusion

In this chapter we review the main results presented in the thesis, drawing the general conclusions from the experimental investigations conducted in the laboratory at the university of Trento. Suggestions for future developments are briefly discussed, considering the issues that the present work have raised.

## 6.1 Concluding remarks

The work has regarded the experimental investigation of dry granular flows over an erodible bed in a rectangular channel. The research has been motivated by the need to deepen the knowledge of this type of flows, which are widely present both in nature and industrial applications as largely explained in chapter 1. Certain processes, in fact, can be idealised as solid-fluid mixtures (where the fluid can be also air) composed of cohesionless grains of uniform sizes and density, whose mutual interactions are responsible for the global behaviour of the ensemble. In particular, the thesis deals with flows in confined geometry and over the erodible bed. These are key elements of natural movement of masses, such as snow-avalanches and debris flows, which develop over loose deposits that are dynamically coupled with the flowing materials. By reviewing the experimental works carried out on this topic, we found out some confusing results, and a lack of an accurate characterization of this flow in dry conditions. Therefore we decided to focus the attention on this topic.

A large number of experiments were carried out by using a rectangular flume, having transparent side-walls and an upper hopper to feed continuously the channel with the granular material. Imaging techniques were used to reconstruct the flow-field and to have a precise description of the process (chapter 3). The first aspect that was considered regarded the i) relevance of the boundary conditions to get uniform and steady conditions in the channel (section 4.2), pointing out the importance of

the section where the data are acquired. In this part, we have shown that the disturbing effects on the flow can be minimized by using a multiple slit gate instead of a simple weir at the end of the channel, in order to control the deposit formation and the adaptation length of the fluid.

The second object of the thesis was to fully characterized the flow by obtaining profiles of velocity, concentration and granular temperature. It was achieved by using the Voronoï techniques developed by the University of Trento (section 3.2), which are able to detect and track each particle composing the mixture. This aspect is very important to obtain reliable profiles of granular temperature of the flow, which cannot be derived by the traditional imaging technique. The thesis contributes with an accurate data set to the literature on this topic, giving detailed profiles for very slow to very fast flows. Thanks to this analysis, vertical structures were outlined together with transversal ones.

The third aspects considered was the effect of the lateral confinement on the flow dynamics. Summarizing the findings, we can affirm that for the same specific discharge Q/W i) by enlarging the width of the channel there is a kind of transition of regime, from a laminar to a collisional one as regard the surface layers of the flow; ii) as a consequence of this transition, the surface velocity is lower for larger widths, while the collisional agitation of the particles increases and occupy a larger region near the side-walls; iii) the flow-depth increases by increasing the width. These three aspects together have been interpreted according a simple model based on an hydraulic approach (section 5.2), which reveals that, by considering a different roughness between the walls and the bed, for the same specific discharge, the velocity has a maximum where this transition occurs. The peak is localized at very narrow channels (of the order of some particle diameters), while a steady condition is predicted for larger channels. However, the model does not offer a rheological approach, but only a simple explanation of the process.

A rheological interpretation of the data is given in section 5.3, by employing the kinetic theory for dense gases and the heuristic model proposed by Armanini *et al.* (2014). While the kinetic theory predicts quite well the collisional contribution in the upper layers of the flow-depth, the heuristic model is able to give an estimation of the frictional contribution of the stresses. Finally, some energetic considerations have been derived, by considering the comparison between the classical kinetic theories and the extended version proposed by Jenkins (2007), revealing how the latter one is better to predict the dissipation and production terms of the balance.

Two other experimental aspects have been investigated: (iv) the micro-mechanical characterization of the particle collisions with a plate and the direct measure of the

stresses at the side-walls (v). We were able to derive the three parameters that describe the interaction of the grains with the lateral boundaries, using an experimental apparatus that was built for this goal. As concern the design of the experimental device to measure the shear stresses, we obtained only a prototype version that is still under test. The mechanical parts were designed and built by using two different materials, while the electric components were planned to enhance the small variation of tension due to the excitement of the devise. However, some problems slew down the application of the tool to the experimental apparatus, and only preliminary results are available.

## 6.2 Future recommendations

Starting from what has been done during the thesis work, one of the future task is to solve and develop a well-functioning version of the device designed to measure the shear stresses at the side-walls. Some steps have been obtained by changing the construction characteristics of the tool, but some improvements can be achieved also by modifying the operational settings during the experiments.

Another aspect that is worth analysing in the future, is the role of the roughness of the wall in the lateral confinement, and what happens if this is equal to the roughness of the loose bed. It could be an interesting aspect and more similar to what occurs in nature, where the lateral levees are made up of the same material composing the flow.

Finally, it would be intriguing performing the same experiments by varying the shape and the density of the particles. In this way the dependence on the parameters could be highlighted more clearly.

# References


Aguirre, M. , Nerone, N. , Ippolito, I. , Calvo, A. , and Bideau, D. (2001). Granular packing: influence of different parameters on its stability. *Granular Matter*, 3 (1-2):75–77.

Ancey, C. (2001). Dry granular flows down an inclined channel: Experimental investigations on the frictional-collisional regime. *Physical Review E*, 65(1):011304.

Ancey, C. and Evesque, P. (2000). Frictional-collisional regime for granular suspension flows down an inclined channel. *Physical Review E*, 62(6):8349.

Ancey, C. , Coussot, P. , and Evesque, P. (1999). A theoretical framework for granular suspensions in a steady simple shear flow. *Journal of Rheology (1978-present)*, 43(6):1673–1699.

Aranson, I. S. and Tsimring, L. S. (2002). Continuum theory of partially fluidized granular flows. *Physical Review E*, 65(6):061303.

Aranson, I. S. and Tsimring, L. S. (2006). Patterns and collective behavior in granular media: Theoretical concepts. *Reviews of modern physics*, 78(2):641.

Armanini, A. , Capart, H. , Fraccarollo, L. , and Larcher, M. (2005). Rheological stratification in experimental free-surface flows of granular–liquid mixtures. *Journal of Fluid Mechanics*, 532:269–319.

Armanini, A. , Fraccarollo, L. , and Larcher, M. (2008). Liquid–granular channel flow dynamics. *Powder Technology*, 182(2):218–227.

Armanini, A. , Larcher, M. , and Fraccarollo, L. (2009). Intermittency of rheological regimes in uniform liquid-granular flows. *Physical Review E*, 79(5):051306.

Armanini, A. , Larcher, M. , Nucci, E. , and Dumbser, M. (2014). Submerged granular channel flows driven by gravity. *Advances in Water Resources*, 63:1–10.

Azanza, E. , Chevoir, F. , and Moucheront, P. (1999). Experimental study of collisional granular flows down an inclined plane. *Journal of Fluid Mechanics*, 400: 199–227.

Bagnold, R. A. (1954). Experiments on a gravity-free dispersion of large solid spheres in a newtonian fluid under shear. In *Proceedings of the Royal Society of London A: Mathematical, Physical and Engineering Sciences*, volume 225, pages 49–63. The Royal Society.

Ballio, F. , Nikora, V. , and Coleman, S. E. (2014). On the definition of solid discharge in hydro-environment research and applications. *Journal of Hydraulic Research*, 52(2):173–184.

Bi, W. , Delannay, R. , Richard, P. , Taberlet, N. , and Valance, A. (2005). Two- and three-dimensional confined granular chute flows: experimental and numerical results. *Journal of Physics: Condensed Matter*, 17(24):S2457.

Bouchaud, J.-P. , Cates, M. , Prakash, J. R. , and Edwards, S. (1994). A model for the dynamics of sandpile surfaces. *Journal de Physique I*, 4(10):1383–1410.

Brodu, N. , Richard, P. , and Delannay, R. (2013). Shallow granular flows down flat frictional channels: Steady flows and longitudinal vortices. *Physical Review E*, 87 (2):022202.

Campbell, C. S. (1990). Rapid granular flows. *Annual Review of Fluid Mechanics*, 22(1):57–90.

Capart, H. , Young, D. , and Zech, Y. (2002). Voronoï imaging methods for the measurement of granular flows. *Experiments in Fluids*, 32(1):121–135.

Cruz, F. , da, Emam, S. , Prochnow, M. , Roux, J.-N. , and Chevoir, F. (2005). Rheophysics of dense granular materials: Discrete simulation of plane shear flows. *Physical Review E*, 72(2):021309.

Daerr, A. and Douady, S. (1999). Sensitivity of granular surface flows to preparation. *EPL (Europhysics Letters)*, 47(3):324.

Gennes, P.-G. , de (1999). Granular matter: a tentative view. *Reviews of modern physics*, 71(2):S374.

Delannay, R. , Louge, M. , Richard, P. , Taberlet, N. , and Valance, A. (2007). Towards a theoretical picture of dense granular flows down inclines. *Nature Materials*, 6(2):99–108.

Drake, T. G. (1990). Structural features in granular flows. *Journal of Geophysical Research: Solid Earth (1978–2012)*, 95(B6):8681–8696.

Dury, C. M. , Ristow, G. H. , Moss, J. L. , and Nakagawa, M. (1998). Boundary effects on the angle of repose in rotating cylinders. *Physical Review E*, 57(4):4491.

Ertaş, D. , Grest, G. S. , Halsey, T. C. , Levine, D. , and Silbert, L. E. (2001). Gravity-driven dense granular flows. *EPL (Europhysics Letters)*, 56(2):214.

Foerster, S. F. , Louge, M. Y. , Chang, H. , and Allia, K. (1994). Measurements of the collision properties of small spheres. *Physics of Fluids (1994-present)*, 6(3): 1108–1115.

Forterre, Y. and Pouliquen, O. (2008). Flows of dense granular media. *Annu. Rev. Fluid Mech.*, 40:1–24.

GDR-MiDi (2004). On dense granular flows. *Eur. Phys. J. E*, 14:341–365.

Goldhirsch, I. (1999). Scales and kinetics of granular flows. *Chaos: An Interdisciplinary Journal of Nonlinear Science*, 9(3):659–672.

Goldshtein, A. and Shapiro, M. (1995). Mechanics of collisional motion of granular materials. part 1. general hydrodynamic equations. *Journal of Fluid Mechanics*, 282:75–114.

Grasselli, Y. and Herrmann, H. (1997). On the angles of dry granular heaps. *Physica A: Statistical Mechanics and its Applications*, 246(3):301–312.

Grasselli, Y. and Herrmann, H. (1999). Shapes of heaps and in silos. *The European Physical Journal B-Condensed Matter and Complex Systems*, 10(4):673–679.

Gray, W. and Lee, P. (1977). On the theorems for local volume averaging of multiphase systems. *International Journal of Multiphase Flow*, 3(4):333–340.

Hill, K. M. , Gioia, G. , and Tota, V. V. (2003). Structure and kinematics in dense free-surface granular flow. *Physical Review Letters*, 91(6):064302.

Holyoake, A. J. and McElwaine, J. N. (2012). High-speed granular chute flows. *Journal of Fluid Mechanics*, 710:35–71.

Jackson, R. (1986). Some features of the flow of granular materials and aerated granular materials. *Journal of Rheology (1978-present)*, 30(5):907–930.

Jaeger, H. M. , Nagel, S. R. , and Behringer, R. P. (1996). Granular solids, liquids, and gases. *Reviews of Modern Physics*, 68(4):1259.

Janssen, H. (1895). Versuche über getreidedruck in silozellen. *Zeitschr. d. Vereines deutscher Ingenieure*, 39(35):1045–1049.

Jenkins, J. (1992). Boundary conditions for rapid granular flow: flat, frictional walls. *Transactions of the ASME*, 59:120–127.

Jenkins, J. and Richman, M. (1985). Kinetic theory for plane flows of a dense gas of identical, rough, inelastic, circular disks. *Physics of Fluids (1958-1988)*, 28(12): 3485–3494.

Jenkins, J. and Savage, S. (1983). A theory for the rapid flow of identical, smooth, nearly elastic, spherical particles. *Journal of Fluid Mechanics*, 130:187–202.

Jenkins, J. T. (2006). Dense shearing flows of inelastic disks. *Physics of Fluids (1994-present)*, 18(10):103307.

Jenkins, J. T. (2007). Dense inclined flows of inelastic spheres. *Granular matter*, 10 (1):47–52.

Jenkins, J. T. and Hanes, D. M. (1998). Collisional sheet flows of sediment driven by a turbulent fluid. *Journal of Fluid Mechanics*, 370:29–52.

Jenkins, J. T. and Louge, M. Y. (1997). On the flux of fluctuation energy in a collisional grain flow at a flat, frictional wall. *Physics of Fluids (1994-present)*, 9 (10):2835–2840.

Johnson, P. C. and Jackson, R. (1987). Frictional–collisional constitutive relations for granular materials, with application to plane shearing. *Journal of fluid Mechanics*, 176:67–93.

Johnson, P. C. , Nott, P. , and Jackson, R. (1990). Frictional–collisional equations of motion for participate flows and their application to chutes. *Journal of Fluid Mechanics*, 210:501–535.

Jop, P. (2008). Hydrodynamic modeling of granular flows in a modified couette cell. *Physical Review E*, 77(3):032301.

Jop, P. , Forterre, Y. , Pouliquen, O. , *et al.* (2005). Crucial role of sidewalls in granular surface flows: consequences for the rheology. *Journal of Fluid Mechanics*, 541(1):167.

Jop, P. , Forterre, Y. , and Pouliquen, O. (2006). A constitutive law for dense granular flows. *Nature*, 441(7094):727–730.

Khakhar, D. , Orpe, A. V. , Andresén, P. , and Ottino, J. (2001). Surface flow of granular materials: model and experiments in heap formation. *Journal of Fluid Mechanics*, 441:255–264.

Kharaz, A. , Gorham, D. , and Salman, A. (2001). An experimental study of the elastic rebound of spheres. *Powder Technology*, 120(3):281–291.

Komatsu, T. S. , Inagaki, S. , Nakagawa, N. , and Nasuno, S. (2001). Creep motion in a granular pile exhibiting steady surface flow. *Physical review letters*, 86(9): 1757.

Kumaran, V. (2009). Dynamics of dense sheared granular flows. part 1. structure and diffusion. *Journal of Fluid Mechanics*, 632:109–144.

Kumaran, V. and Bharathraj, S. (2013). The effect of base roughness on the development of a dense granular flow down an inclined plane. *Physics of Fluids (1994-present)*, 25(7):070604.

Larcher, M. (2002). Vertical structure of highconcentration liquid-granular flows. *Monographs of the School of Doctoral Studies in Environmental Engineering, Trento*, 2.

Larcher, M. , Fraccarollo, L. , Armanini, A. , and Capart, H. (2007). Set of measurement data from flume experiments on steady uniform debris flows. *Journal of Hydraulic Research*, 45(sup1):59–71.

Lemieux, P.-A. and Durian, D. (2000). From avalanches to fluid flow: A continuous picture of grain dynamics down a heap. *Physical Review Letters*, 85(20):4273.

Lois, G. , Lemaitre, A. , and Carlson, J. (2006). Emergence of multi-contact interactions in contact dynamics simulations of granular shear flows. *EPL (Europhysics Letters)*, 76(2):318.

Louge, M. Y. (2003). Model for dense granular flows down bumpy inclines. *Physical Review E*, 67(6):061303.

Louge, M. Y. and Keast, S. C. (2001). On dense granular flows down flat frictional inclines. *Physics of fluids*, 13:1213.

Lun, C. and Savage, S. (1986). The effects of an impact velocity dependent coefficient of restitution on stresses developed by sheared granular materials. *Acta Mechanica*, 63(1-4):15–44.

Lun, C. and Savage, S. (1987). A simple kinetic theory for granular flow of rough, inelastic, spherical particles. *Journal of applied mechanics*, 54(1):47–53.

Maw, N. , Barber, J. , and Fawcett, J. (1976). The oblique impact of elastic spheres. *Wear*, 38(1):101–114.

Mitarai, N. and Nakanishi, H. (2005). Bagnold scaling, density plateau, and kinetic theory analysis of dense granular flow. *Physical review letters*, 94(12):128001.

Nikora, V. , Ballio, F. , Coleman, S. , and Pokrajac, D. (2013). Spatially averaged flows over mobile rough beds: Definitions, averaging theorems, and conservation equations. *Journal of Hydraulic Engineering*, 139(8):803–811.

Pouliquen, O. (1999). Scaling laws in granular flows down rough inclined planes. *Physics of Fluids (1994-present)*, 11(3):542–548.

Rajchenbach, J. (1990). Flow in powders: From discrete avalanches to continuous regime. *Physical review letters*, 65(18):2221.

Roscoe, K. H. , Schofield, A. , and Wroth, C. (1958). On the yielding of soils. *Geotechnique*, 8(1):22–53.

Roux, J.-N. and Combe, G. (2002). Quasistatic rheology and the origins of strain. *Comptes Rendus Physique*, 3(2):131–140.

Roux, S. and Radjai, F. (1998). Texture-dependent rigid-plastic behavior. In *Physics of dry granular media*, pages 229–236. Springer.

Savage, S. (1998). Analyses of slow high-concentration flows of granular materials. *Journal of Fluid Mechanics*, 377:1–26.

Savage, S. B. (1984). The mechanics of rapid granular flows. *Advances in applied mechanics*, 24:289–366.

Schofield, A. and Wroth, P. (1968). Critical state soil mechanics.

Silbert, L. E. , Ertaş, D. , Grest, G. S. , Halsey, T. C. , Levine, D. , and Plimpton, S. J. (2001). Granular flow down an inclined plane: Bagnold scaling and rheology. *Physical Review E*, 64(5):051302.

Silbert, L. E. , Landry, J. W. , and Grest, G. S. (2003). Granular flow down a rough inclined plane: transition between thin and thick piles. *Physics of Fluids (1994-present)*, 15(1):1–10.

Spinewine, B. , Capart, H. , Larcher, M. , and Zech, Y. (2003). Three-dimensional voronoï imaging methods for the measurement of near-wall particulate flows. *Experiments in Fluids*, 34(2):227–241.

Taberlet, N. , Richard, P. , Valance, A. , Losert, W. , Pasini, J. M. , Jenkins, J. T. , and Delannay, R. (2003). Superstable granular heap in a thin channel. *Physical review letters*, 91(26):264301.

Taberlet, N. , Richard, P. , Henry, E. , and Delannay, R. (2004). The growth of a super stable heap: An experimental and numerical study. *EPL (Europhysics Letters)*, 68(4):515.

Tubino, M. and Lanzoni, S. (1993). Rheology of debris flows: experimental observations and modelling problems. *Excerpta of the Italian Contributions to the Field of Hydraulic Engineering*, 7:201–236.

Vanel, L. , Howell, D. , Clark, D. , Behringer, R. , and Clément, E. (1999). Memories in sand: Experimental tests of construction history on stress distributions under sandpiles. *Physical Review E*, 60(5):R5040.

Walton, O. R. and Braun, R. L. (1986). Viscosity, granular-temperature, and stress calculations for shearing assemblies of inelastic, frictional disks. *Journal of Rheology (1978-present)*, 30(5):949–980.